UNIVERSITY OF OKLAHOMA

GRADUATE COLLEGE

BLAST WAVE TRANSMISSION THROUGH THE EAR WITH COMPUTATIONAL AND 3D PRINTED MODELS AND ASSESSMENT OF COCHLEA DAMAGE WITH SEM IMAGING

A DISSERTATION

SUBMITTED TO THE GRADUATE FACULTY

in partial fulfillment of the requirements for the

Degree of

DOCTOR OF PHILOSOPHY

By

MARCUS BROWN
Norman, Oklahoma
2021

BLAST WAVE TRANSMISSION THROUGH THE EAR WITH COMPUTATIONAL AND 3D PRINTED MODELS AND ASSESSMENT OF COCHLEA DAMAGE WITH SEM IMAGING

A DISSERTATION APPROVED FOR THE
STEPHENSON SCHOOL OF BIOMEDICAL ENGINEERING

BY THE COMMITTEE CONSISTING OF

Dr. Rong Z. Gan, Chair

Dr. Vassilios I. Sikavitsas

Dr. Lei Ding

Dr. Chenkai Dai

Dr. Zahed Siddique

I dedicate this dissertation to my family, for whom I would not have the strength to accomplish so much.

Acknowledgments

I would like to acknowledge my advisor, Dr. Rong Z. Gan, for her support and mentorship throughout my Ph.D. program at the Stephenson School of Biomedical Engineering. Her persistence and passion for research helped develop the start of my research career and accomplish goals I would have considered unattainable before. The skills I have learned while under Dr. Gan's mentorship will prove invaluable for the rest of my research career.

I would like to thank my committee members, Dr. Vassilios I. Sikavitsas, Dr. Chenkai Dai, Dr. Lei Ding, and Dr. Zahed Siddique, who have all set time aside to help and give advice during my time at the University of Oklahoma. I would also like to thank Dr. Detamore for taking time out of his busy schedule to advise and support my research efforts.

I would like to express my eternal gratitude to the members of the Biomedical Engineering Laboratory for the immeasurable amount of help during my studies there. Dr. Shangyuan Jiang was helpful in all aspects of my research in the lab and a needed friend. Past members, Dr. Zach Yokell, Kyle Smith, Brooke Hitt, and Warren Engles, have all made this research journey much more fun. I would like to thank past member Kegan Leckness for helping me get my start with the lab's ear model, and Paige Welch and John J. Bradshaw for their help in developing our current models. I would like to also thank a past undergraduate researcher, Emily May, for work on the 3D printed temporal bone project.

I appreciate Dr. Preston Larson of the Samuel Roberts Noble Microscopy Laboratory for his help with my scanning election microscopy project and for allowing

me to work long nights on the electron microscopes. I would also like to personally thank David Akin from OU Supercomputing Center for Education & Research for aiding us in utilizing OU's supercomputers for finite element models. This work was supported by DoD grants W81XWH-14-1-0228 and W81XWH-19-1-0469.

Most of all, I would like to show my unending gratitude to my wife, Dr. Ashley Brown, and daughter, Olivia L. Brown, for their unwavering support and love through a transformative time in my life.

Table of Contents

List of Tables

List of Figures

Abstract

Blast-induced injuries affect the health of service members, veterans, and other victims, in which the auditory system is often damaged rupturing the tympanic membrane (TM) and reducing the number of viable cochlear hair cells. Blast-induced auditory damage to the outer and middle ear can usually be non-invasively observed but examining the damage to the inner ear is difficult to quantify. Finite element (FE) modeling and scanning electron microscopy (SEM) provide tools that allow for the prediction of the inner ear functional changes and assessment of the inner ear damage, respectively, when the ear is exposed to blast. Hearing protection devices (HPDs) have become the critical personal protection equipment to avoid this auditory damage for service members. Acoustic test fixtures and human temporal bones (TBs) have been used to test and develop HPDs; however, the lack of a cost-effective, standardized model impedes the improvement of HPDs.

In this study, we utilized a FE model of the human ear with a spiraled, two-chambered cochlea to simulate the response of the anatomically structured cochlea to blast overpressure (BOP) exposure. The FE model included an ear canal, a middle ear, and two and a half turns of a two-chambered cochlea and simulated a BOP transmission from the ear canal entrance to the spiral cochlea. The model was validated with experimental pressure measurements from the outer and middle ear of human cadaveric TBs. The results showed high stapes footplate displacements resulting in high intracochlear pressures and basilar membrane (BM) displacements at a BOP input of 30.7 kPa. The cochlea's spiral shape caused asymmetric pressure distributions across the width of the cochlea and significant BM transverse motion.

To create a standardized model for testing HPDs, a 3D printed human TB model was developed that reproduces the responses observed in blast testing of human TBs with and without HPDs. The 3D printed model consisted of the ear canal, TM, ossicular chain, middle ear suspensory ligaments/muscle tendons, and middle ear cavity. Pressures were measured at the ear canal entrance (P0) and near the TM in the ear canal (P1) during blasts then compared to similar tests in human TBs. Laser Doppler vibrometry was used to further validate TM movement under acoustic stimulation. Results indicated that in the 3D printed TB, the attenuated peak pressures at P1 induced by HPDs ranged from 0.92 – 1.06 psi (170 – 171 dB) with blast peak pressures of 5.62 – 6.54 psi (186 – 187 dB) at P0 which were well within the mean and standard deviation of published data from tests in human TBs.

SEM imaging was used to investigate the viability of outer hair cells (OHCs) of chinchillas that were exposed to six consecutive blast exposures ranging from 21-35 kPa (3-5 psi) and the effect of liraglutide, a glucagon-like peptide-1 receptor agonist, on OHC survival after blast exposure. Results showed that OHC loss did not differ among animal groups; however, the auditory brainstem response results showed hearing function loss in BOP exposed groups, and drug-treated chinchillas did regain more hearing function after blast.

The spiral cochlea model reported in this dissertation provides a necessary advancement for progress towards a model able to predict the potential hearing loss sustained during BOP exposure. The developed 3D printed TB provides an accurate and cost-effective evaluation tool for HPDs' protective function against BOP exposure with the potential to perform as a human temporal bone model for research in ear

biomechanics for acoustic transmission and the development of middle ear implants. Furthermore, the SEM study increases our understanding of the link between TBI and hearing loss while also supporting the use of liraglutide as a therapeutic for blast victims. In conclusion, the work reported in this dissertation increases our understanding of cochlear mechanics and sustained damage from blast exposure, and as such, creates opportunities for future research that will progress towards the goals of understanding the damage mechanisms of blast in the inner ear, creating a model that can accurately predict the damage to the ear from a given stimulus, and improving HPDs' effectiveness for protection against BOP exposure.

Chapter 1 Introduction

1.1 Structure and Function of the Outer and Middle Ear

Hearing and balancing are the primary functions of the human ear. Figure 1-1 shows the anatomy of the entire human ear organ, and the ear is comprised of three main regions: outer, middle, and inner ear. These three regions are also known as the peripheral auditory system (PAS). The ear is responsible for capturing acoustic sound pressure waves in the air and transducing them into action potential bound for the central auditory system (CAS) region of the brain via the auditory nerve. Humans are capable of hearing sound in the frequency range of 20 Hz to 20 kHz.

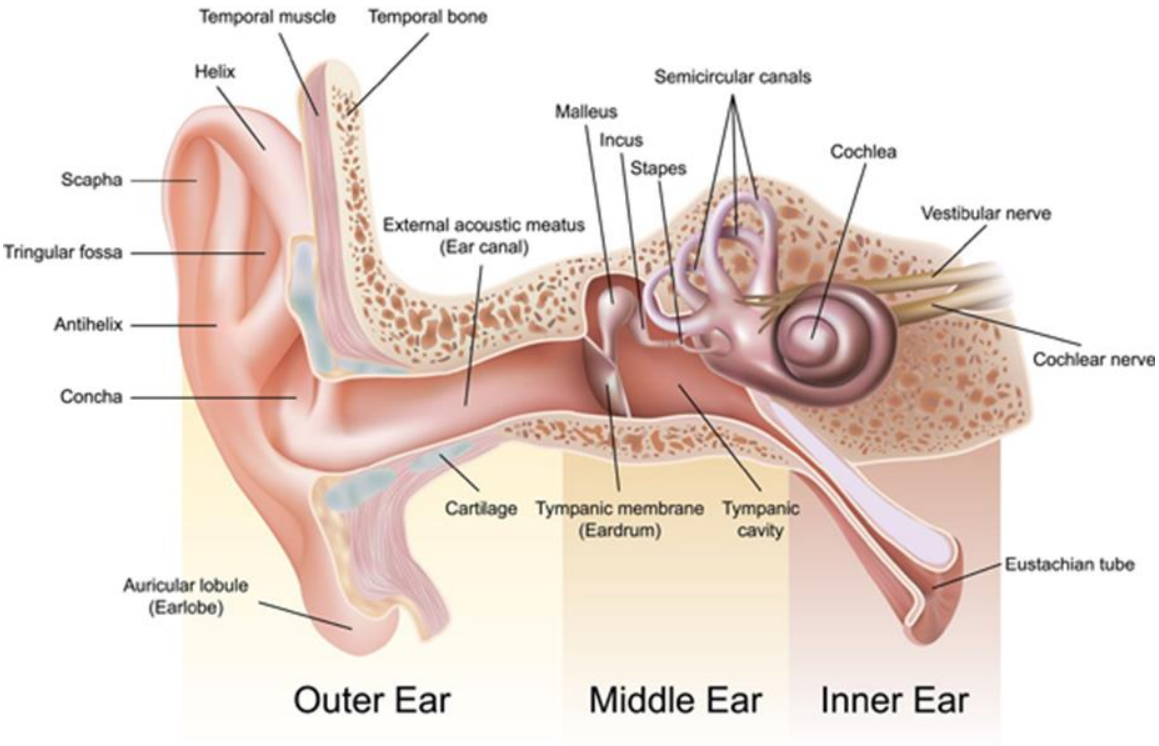

Figure 1-1. Illustration of the anatomy of the human ear. (https://earaudities.wordpress.com/basic-anatomy)

The outer ear is comprised of the pinna (from the helix to the earlobe in Figure 1-1) and the ear canal. The external portion of the ear, known as the pinna, consists of auricular cartilage, and sound localization is the primary function of the pinna which is aided by its complex shape.[1] Starting at the pinna, the ear canal (or acoustic meatus) is 2.3 cm (approximately) long and amplifies and carries sound to the tympanic membrane (TM) which closes the medial end of the ear canal.[29,109]

The TM is a soft tissue membrane in the ear and is essential for sensing sound pressure. The membrane sits at the end of the ear canal and serves as a barrier between the outer and middle ear (Figure 1-1). This membrane is sensitive enough to sense the small fluctuations in air pressure (sound) which cause it to vibrate. Given its importance in the hearing organ, the TM's ability to perform as intended will influence a person's capability to hear correctly. A few properties of the TM have the most influence on its function. The TM's specific cone shape increases its ability to detect sound waves with a typical area between 55.8 to 85.0 mm^2,[24,91] and despite averaging from 70 to 100 μm in thickness, this membrane has an intricate collagen network, with collagen fibers in both the radial and circumferential directions, that gives the TM its flexible yet tough viscoelastic properties.[94,98,111]

The TM connects to the ossicular chain which consists of three bones: malleus, incus, and stapes (Figure 1-2). These bones are responsible for passively transmitting vibrations from the TM to the inner ear. The malleus connects to the TM along the arm of the malleus (or manubrium) and attaches to the head of the incus at its head through the incudomalleolar joint (IMJ). The long process of the incus is connected to the head of the stapes by the incudostapedial joint (ISJ). The ossicular chain terminates at the stapes

footplate (SFP) where the stapes motion transmits the vibrations from the TM to the cochlea at the oval window. The ossicles are suspended by ligaments and muscle tendons within the middle ear cavity: superior mallear ligament, lateral mallear ligament, anterior mallear ligament, posterior incudal ligament, posterior stapedial tendon, tensor tympani tendon. These ligaments and tendons suspend the ossicles so they can freely rotate to effectively transmit acoustic pressure from the TM to the cochlea, usually referred to as the middle ear transfer function.[31] In addition, the stapedial and tensor tympani tendons' muscle contractions perform important functions within the middle ear, such as protection from intense sound.[5,10]

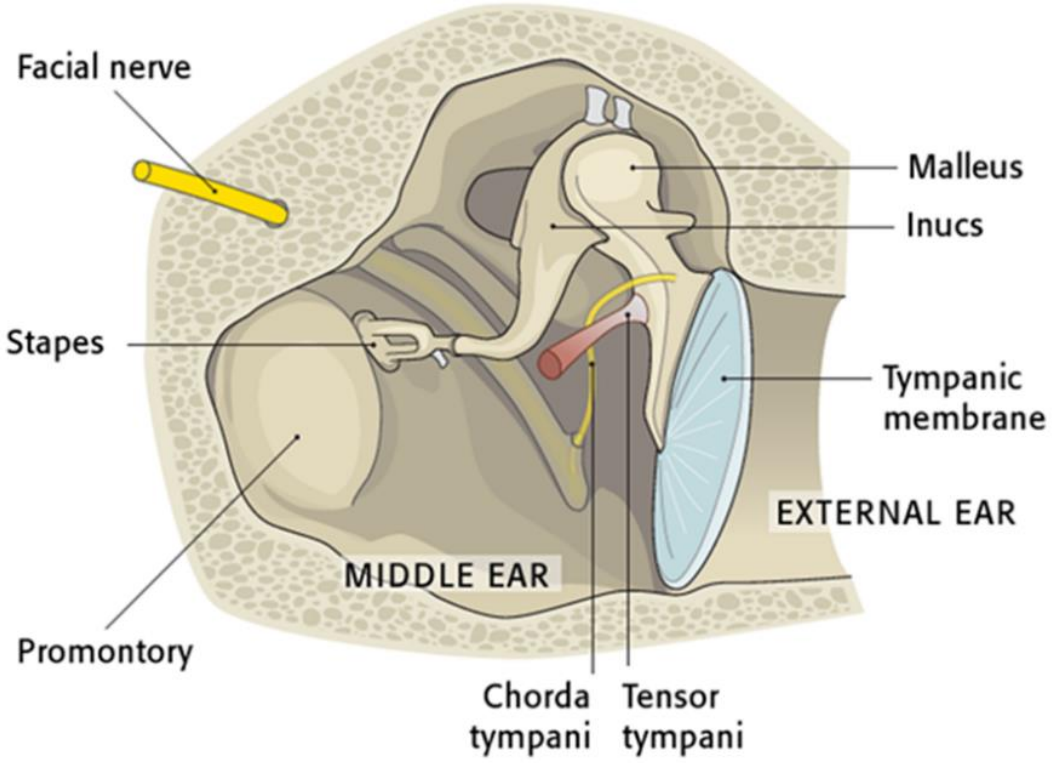

Figure 1-2. Human middle ear highlighting the ossicular chain (https://resources.aofoundation.org/-/jssmedia/surgery/93/93_ls20_treatment_i400.ashx?w=400)

1.2 Structure and Function of the Inner Ear

The inner ear, or cochlea, is where the mechanical energy from acoustic sound is transduced into action potentials for the brain to decode. The cochlea has three fluid-filled chambers, and this fluid is pressurized by the SFP movement to create pressure fluctuations within the cochlea's chambers (Figure 1-3). The three chambers are: scala vestibuli (SV), scala media (SM), and scala tympani (ST). The barrier between the SV and SM is the vestibular membrane, or Reissner's membrane (RM), and the barrier between the SM and ST is the basilar membrane (BM) (Figure 1-3). The membranes isolate the potassium-rich fluid, endolymph, within the SM from the perilymph (sodium-rich fluid similar to cerebrospinal fluid) in the ST and SV.[88] The RM's function is to transport fluid and electrolytes while the BM contains the organ of Corti where the sensory receptors are in the ear.

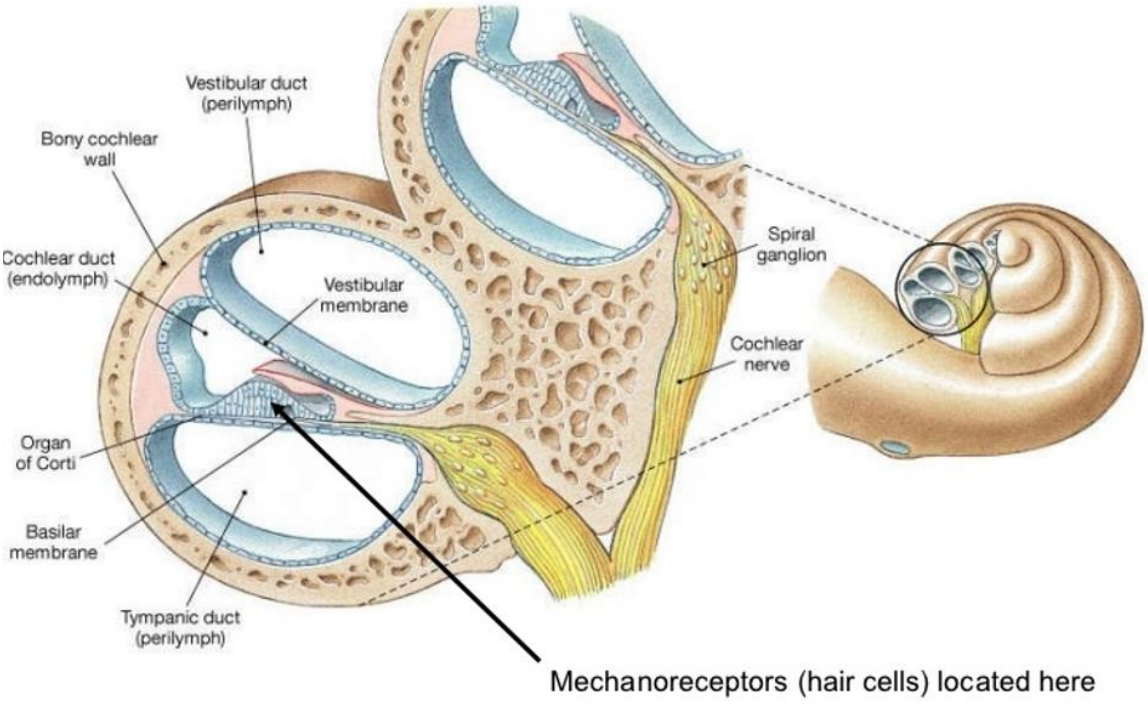

Figure 1-3. Cochlear chambers
(http://droualb.faculty.mjc.edu/Lecture%20Notes/)

The BM vibrates from the pressure fluctuations caused by the stapes and moves the organ of Corti (Figure 1-4).[88] Some of the cells within the organ of Corti are sensory cells called hair cells which detect mechanical movement and turns it into action potentials.[79,88] This is accomplished through the hair cell's sensory organelle known as the stereocilia. Directly above the organ of Corti is the tectorial membrane which is in contact with the stereocilia of the hair cells below. The mechanical motion of the stereocilia moves the extra-cellular protein chains that connect the stereocilia rows, known as tip links.[79,88] This strains the tip links which open potassium ion channels in the stereocilia leading to depolarization of the hair cell (Figure 1-4). This is commonly referred to as mechanoelectrical transduction.[21] The depolarization opens voltage-gated calcium ion channels which increase the release of neurotransmitter-filled vesicles at the bottom end of the hair cell.[79,88]

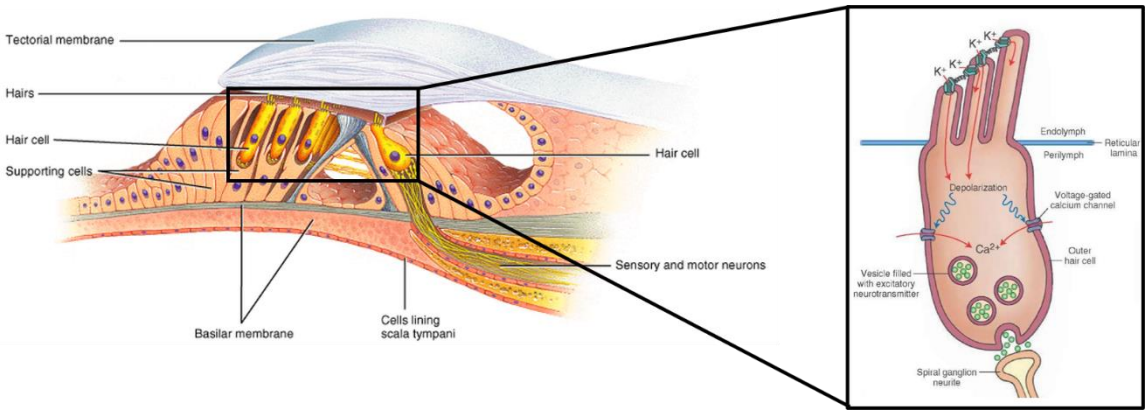

Figure 1-4. Organ of Corti (left) and hair cell structure and function (right)
(Left: John Wiley & Sons, Inc.; Right: http://what-when-how.com/neuroscience/auditory-and-vestibular-systems-sensory-system-part-1/)

The detection of sound is not merely a passive detection of acoustic waves, however. The hair cells play an important role in amplifying, dampening, and focusing the movement of the BM.[12,36,79,88] The two types of hair cells that exist in the organ of Corti are the inner hair cells (IHC) and outer hair cells (OHC), and they interact with

each other through a free-to-vibrate tectorial membrane.[79,88] IHCs are the main cells used for transducing the mechanical vibrations into action potentials, whereas the OHCs play an important role in controlling the movement of the BM.[88] Myelinated efferent neuron terminate directly at the OHC which gives the brain direct feedback to the cochlea.[79] This synaptic connection can cause the OHC to quickly activate electromotive proteins (prestin) that either contract or lengthen the cell's body which leads to a change in frequency detected by the IHCs.[12,36,79,88]

Another important mechanic of the cochlea is the slow displacement waves that propagate from the base to the apex, known as traveling waves.[2,88] In work that awarded Georg von Békésy[2] the 1961 Nobel Prize for Physiology or Medicine, the traveling wave was found to travel along the BM from base to the apex during normal sound stimuli, and as the wave propagated, its magnitude grew until it reached its respective frequency location at the BM in which it then quickly decays in magnitude.[88] The traveling wave of the cochlea comes from the mechanical properties of the cochlea, such as mass, stiffness, and damping, which passively processes auditory signals with frequency filtering and spatial analysis.[88]

1.3 Modeling the Ear

Many researchers have created models of the ear in an attempt to simulate the ear's function,[24,28,63,86] analyze difficult to measure parameters,[6,85,115] and make predictions of the ear's response or sustained hearing loss from different stimuli.[32,73,78,89] These models range from purely mathematical models to 3D finite element (FE) models (Figure 1-5).[24,76] Models similar to the FE model shown in Figure 1-5 have been used to

analyze the ear's transfer function and simulate the complex motion of the middle ear.[24,28,107]

Early models started as mathematical models that attempted to simulate parts of the auditory system from experimental observations, and models were created (and still being developed) to mimic the auditory system's response to speech.[17,63] Inner ear and auditory nerve (AN) models have progressed to attempt to simulate the AN's activity when the ear canal was stimulated by tones, noise, vowel sounds, and even speech.[4,14,17,63,65,96,115,116] One model in particular by researchers Zilany and Bruce[115] modeled the entire PAS and attempted to predict the active role the cochlea has in sound processing. This model was expanded by the researchers to model impaired auditory nerve fibers, and other studies used this model as part of or inspiration for later models of the PAS.[8,38,41,63,89,116] Many of these models were successful in simulating the PAS's response to various stimuli under normal and impaired conditions, and the models' outputs agreed with comparable experimental results.

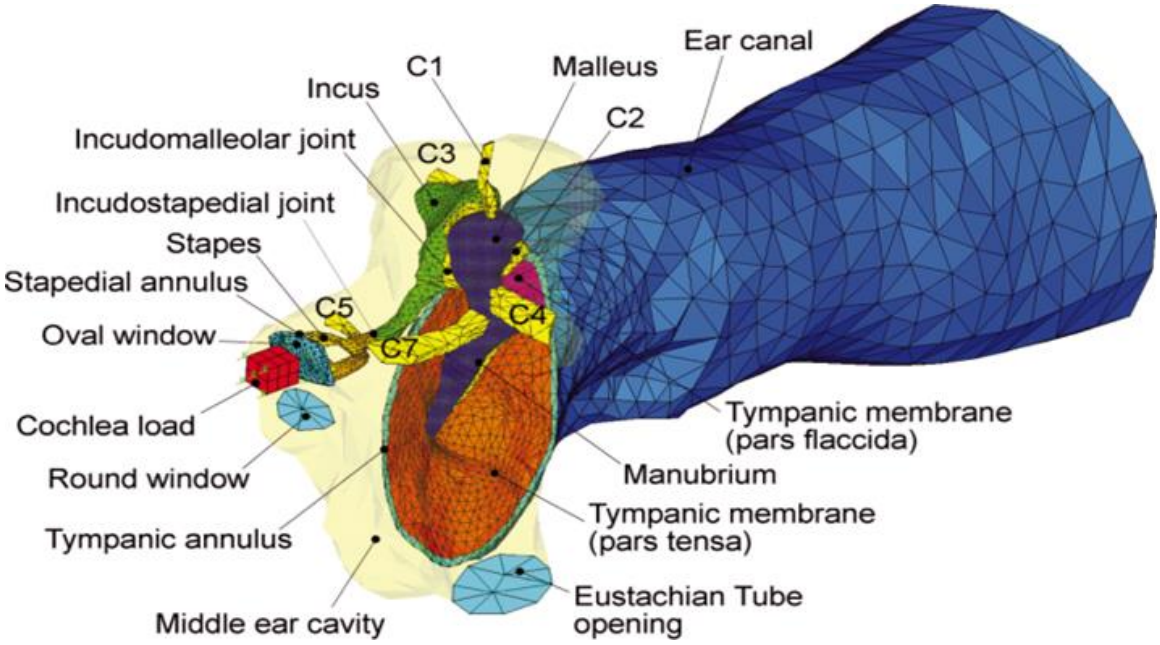

Figure 1-5. FE model of the human ear[24]

A particular topic of interest within the field of modeling the ear is predicting the harmful effects of dangerous stimuli to the ear[6,73,76] or simulating diseased states of the ear.[32,116] The ultimate goal of these models is to be able to accurately assess the sustained damage from various situations without having to experimentally characterize every possibility.[73] Models that can perform this function would greatly inform scientists and physicians on what a patient has experience from their harmful acoustic exposure or disease which would aid in better care and preventive measures.[73] A known model that has been developed for decades by Price and Kalb[78] is the auditory hazard assessment algorithm for the human ear (AHAAH) model. This model attempts to provide a simple output that predicts the possibility of hearing loss by analyzing the resulting motion of the BM from a pressure wave input.[20] A three-dimensional model by Brown et al.[6] simulated the blast wave transmission from the entrance of the ear canal to a straight, two-chamber cochlea to investigate the motion of the BM. Developed from models that were validated through acoustic simulations and experiments, Brown et al. found extreme displacement in the TM, SFP, and BM and high pressures in the ear canal near the TM and within the cochlea.[6] Other models have attempted to predict the ear's response to diseased states such as otitis media,[32,112] fixations or detachments of the ligaments,[13] and hearing loss from noise exposure.[7,73,115,116]

1.4 Blast Exposure and Blast-induced Damage to the Ear

Blast overpressures (BOPs) are rapid and intense increases in pressure that are usually caused by explosions or gunfire. A typical pressure waveform of a BOP can be seen in Figure 1-6, also known as a Friedlander waveform. Direct exposure to the extreme positive pressures of this curve can cause injury to personnel, and the rapid

decrease to the negative phase of the Friedlander curve can cause cavitation within tissue and cells in the form of micro-bubbles.[64] Traumatic injuries from blasts are grouped into four main categories: primary, secondary, tertiary, and quaternary. Blast injuries resulting from the direct interaction of body tissue with the blast's high-pressure wave are considered primary blast injuries. Secondary blast injuries are caused by debris or bomb fragments accelerated by the explosion. Tertiary blast injuries result from when the victim is knocked down or thrown into something by the blast, and quaternary blast injuries encompass all other effects from the blast such as post-traumatic disorder and burns.[11] Blast-induced injuries to the ear are often primary blast injuries.[18]

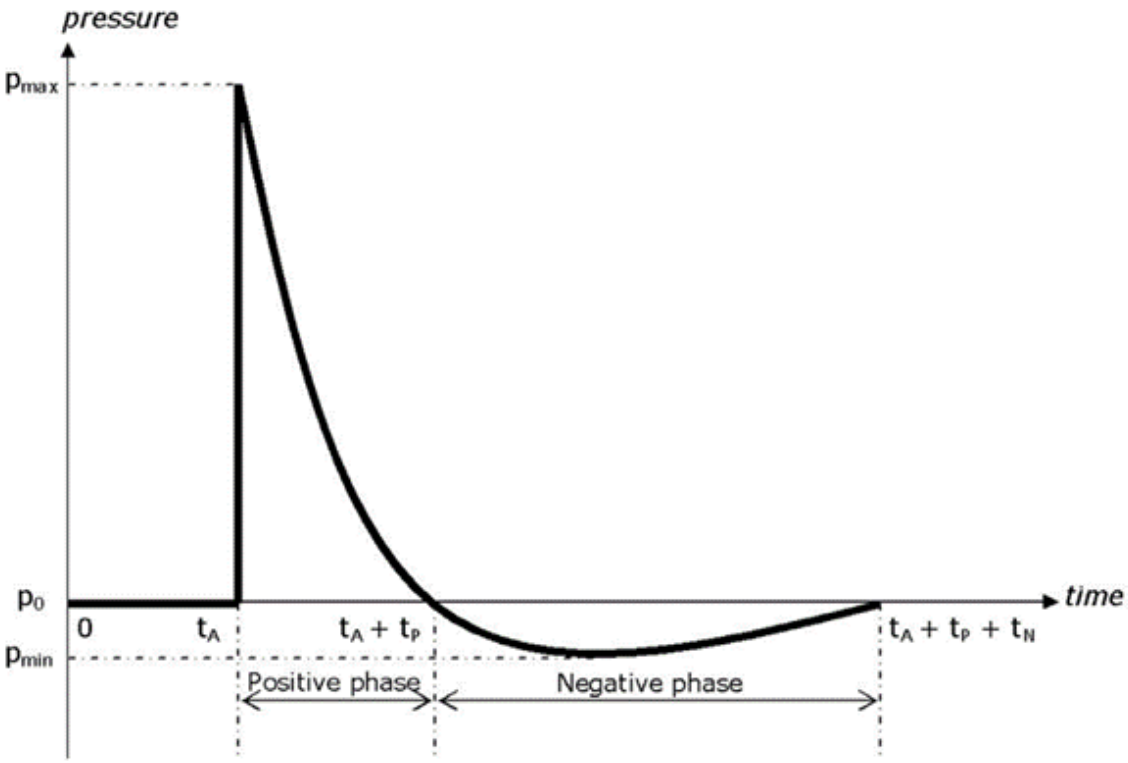

Figure 1-6. Friedlander Waveform[64]

Sensitive to pressure changes, the ear is often damaged when a person is subjected to blast exposures, which can cause hearing loss by rupturing the TM (Figure 1-7) or reducing the number of viable cochlear hair cells.[39] Dougherty et al.[18] reported a study on 3,981 military

personnel that suffered a blast-related injury and found that TM perforation occurred in 8% of the individuals. Other studies of blast-exposed patients showed the incidence of TM rupture ranged from 10 to 20%.[110] In addition to the TM rupture, the blast overpressure can also interrupt the ossicular chain, and damage the cochlear hair cells.[39]

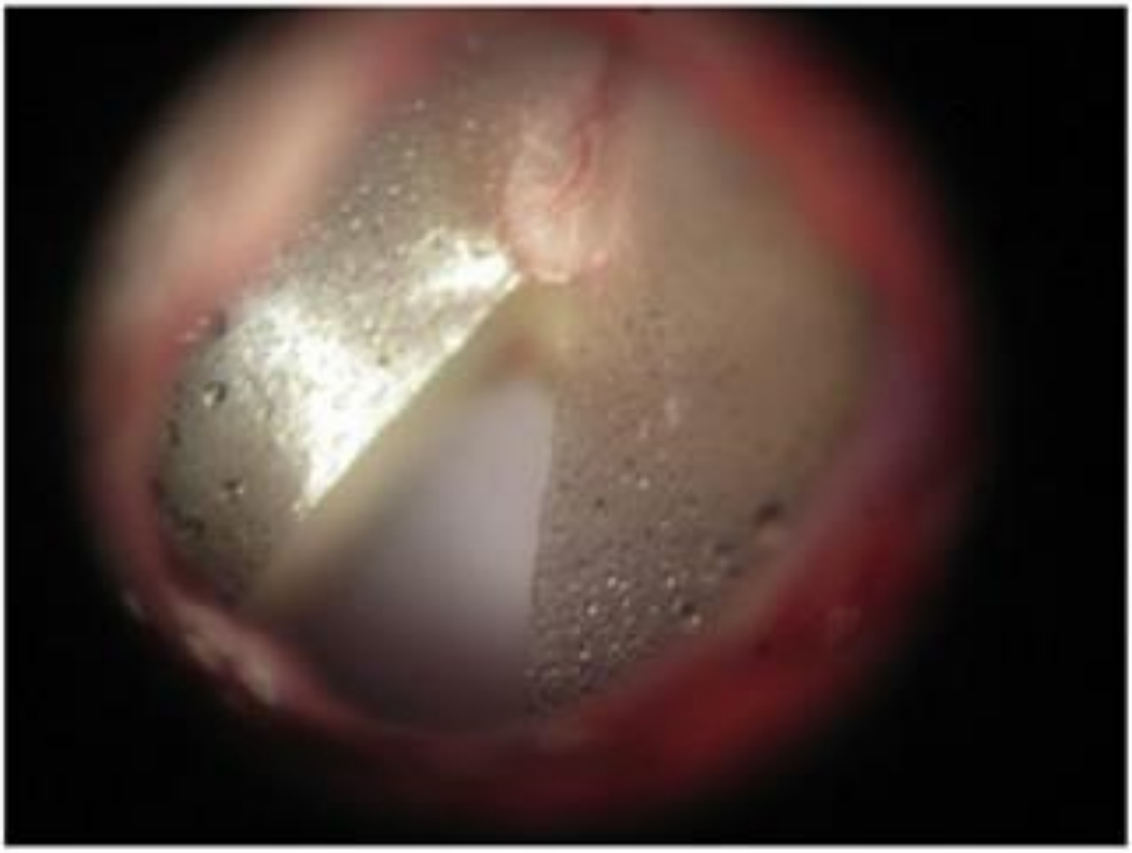

Figure 1-7. Ruptured chinchilla TM after blast exposure[27]

As for the inner ear, a blast wave can transmit through the ear canal (the auditory pathway) and cause intense pressure fluctuations and basilar membrane (BM) vibrations in the cochlea which causes damage. In addition, the cochlea can experience hair cell loss and synaptopathy within cochlea due to the overstimulation during exposure through the auditory pathway similar to what is observed from noise-induced hearing loss.[18,39,81,102] The cochlea's hair cells and ANs can also be damaged from the transmission of the blast

wave through the skull to the cochlea.[52,70] Figure 1-8 shows scanning electron microscopy (SEM) images of the OHCs stereocilia after exposure to a blast wave transmitted through the skull by a laser-induced shock wave.[70] Depending on the blast wave's energy, Niwa et al.[70] found that the stereocilia could be disturbed with the tip-links broken from shock waves through the skull, and damage to the stereocilia increased with increasing blast energy. Histological images of the cochlea also revealed the number of OHCs remained steady despite hearing function tests showed significant hearing loss in exposed animals, but the study did find a reduction in synaptic ribbons to the hair cells.[70]

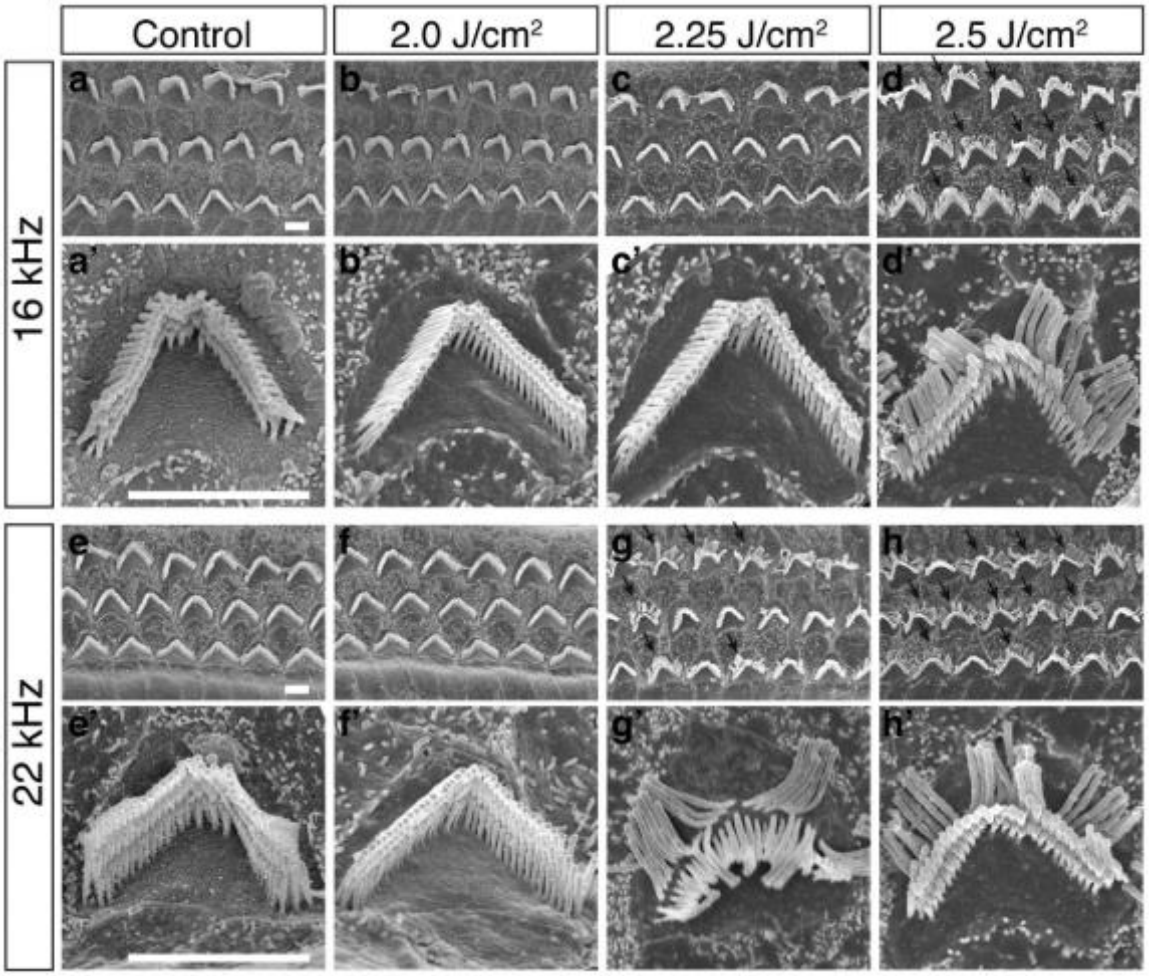

Figure 1-8. Scanning electron microscopy images of the stereocilia exposed to BOPs[70]

Similar results were found in a recent study by Hickman et al.[39] where OHC loss did not show to be significantly higher in chinchillas exposed to BOPs. The authors hypothesize that the rupture of the TM could have protected the hair cells from mechanical damage through excessive BM motion.[39] Furthermore, the animals that did not have ruptured TM did experience greater OHC loss. The synaptic ribbons in the cochlea were greatly reduced as well as the synaptic activity of the hair cells.[39] The situation where hearing loss is present in a subject but no obvious damage can be observed is referred to as synaptopathy.[39,102] This effect has been observed in noise-induced hearing loss research, but recent work has shown that blast exposure can also produce similar synaptopathy symptoms.[39,49,50,102]

Research into the blast effects on the ear is relatively new compared to noise-induced hearing loss so many of the damage mechanisms are still being investigated.[11,18] This is likely due to the intensity and complex interactions during BOP exposure which can affect the CAS as well.[81] The CAS mainly experiences trauma from BOPs through the mechanical transmission of the blast wave through the skull, also known as a blast-induced traumatic brain injury (TBI).[23,61,67,81] This trauma to the nervous system can cause cell death and inflammatory effects in auditory regions of the brain and brainstem causing the previously mentioned symptoms.[23,81] In addition, the CAS is affected by the overstimulation and synaptopathy experienced in the PAS.[92,93] The BOP's complex effects on the peripheral and central auditory systems often overlap and present similar symptoms which significantly increases the difficulty in characterizing the damage to the auditory system during blast exposure.

1.4.1 Investigation of Hearing Protection Devices for Blast Protection

Hearing protection devices (HPDs; Figure 1-9), including different types of earplugs and earmuffs, are used by military service members to mitigate hearing damage, but a certain level of injury to the auditory system is usually inevitable even with protection.[18] The effectiveness of HPDs can be significantly affected by the type, depth of insertion, involvement in bone conduction, and intensity of the blast or noise.[3,68] The traditional approach to evaluating the protective function of HPDs is a test for the real-ear attenuation in human listeners at threshold values designed for low-level noise.[3] Other studies done in humans have assessed participants' hearing function and perceived situational awareness after training excerises[101] or have supplied soldiers with the same HPD and analyzed their hearing function and surveyed their HPD compliance once they returned from deployment.[47] While studies in humans did provide useful insights into HPD effectiveness and possible improvements, many of the results were subjective responses from participants, and obtaining more extensive and standardized data would be invasive, unethical, and harmful to the participants.

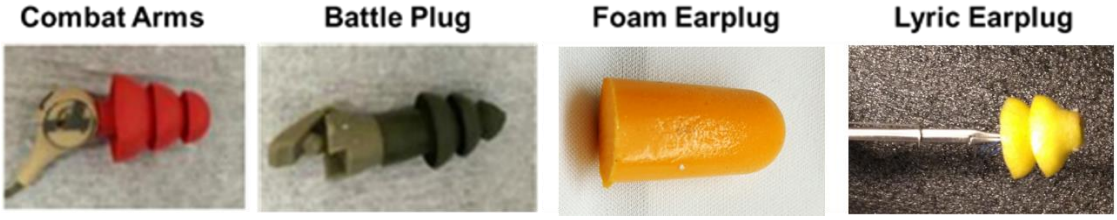

Figure 1-9. Four types of earplugs[26]

Alternative methods in recent studies used microphones to measure the attenuation of high-intensity impulse noise and blast overpressure under the cover of the HPDs inside the acoustic test fixture (ATF).[68,69] ATFs do provide a standardized model for testing HPDs during blast exposure, but the cost of the equipment can be prohibitive

for researchers who need to risk damaging the equipment during blast tests. In contrast with the traditional evaluation methods, the blast wave attenuation of four types of HPDs in human cadaveric temporal bones (TBs) was measured by Gan et al.[26] This study, and those similar to it, showed effective results for assessing the protective function of HPDs in a realistic test model;[26,105] however cadaveric TB models vary in ear canal size and only stay fresh for a limited time which adds variability and time constraints to experiments. This limits the ability to test and improve many HPD designs efficiently. With the severity of blast-induced injuries, it is vital that HPDs vastly improve soon to protect those most at risk.

1.5 Objectives

The hearing loss experienced by veterans who have suffered blast-induced auditory injuries greatly reduced their quality of life after military service.[18,102] Furthermore, hearing disabilities, such as tinnitus and hearing loss, are the top cost for treatment and compensation for the U.S. Department of Veteran Affairs.[18] Understanding how BOP exposure affects the cochlea and BM is essential for discovering the underlying mechanisms of blast-induced hearing loss and protecting against it. In addition, a cost-effective and accurate test model for evaluating HPD will enhance the development of HPDs by providing an accessible and standardizing test model to researchers and developers. However, the BOP exposure effects on the cochlea are not well understood and evaluation of HPDs for protection against BOP is expensive and inefficient. The aim of this study is to increase our understanding of the response of the cochlea during blast exposure, both computationally and experimentally, and to improve the evaluation for developing HPDs' protective function against BOPs. Specifically:

1) To develop a 3D FE model of the entire human ear for simulation of BOP wave transmission from the ear canal to a spiral cochlea,
2) To develop a 3D printed ear model, or TB, that anatomically and mechanically represents the outer and middle ear for the effective evaluation of HPDs during blast exposure, and
3) To utilize SEM to assess the blast-induced hair cell damage in an animal model of chinchilla exposed to blast and the potential therapeutic effect of liraglutide on hair cell viability.

1.6 Outline

Chapter 2 presents the development of a FE model of the human ear with a two-chambered, spiral cochlea for simulating the cochlear mechanics during blast exposure.

Chapter 3 presents the development of a 3D printed human ear model for standardized testing of hearing protection devices during blast exposure.

Chapter 4 presents the assessment of the effect of liraglutide on the blast damages sustained in the chinchilla cochlea with scanning electron microscopy.

Chapter 5 presents the summary of this study and outlook for future studies.

Table 1-1. Table of abbreviations

BOP	Blast Overpressure
PAS	Peripheral Auditory System
CAS	Central Auditory System
TM	Tympanic Membrane
BM	Basilar Membrane
RM	Reissner's Membrane
RWM	Round Window Membrane
SAL	Stapedial Annular Ligament
IMJ	Incudomalleolar Joint
ISJ	Incudostapedial Joint
SFP	Stapes Footplate
TMA	Tympanic Membrane Annulus
3D	Three-Dimensional
FE	Finite Element
TB	Temporal Bone
LDV	Laser Doppler Vibrometry
SPL	Sound Pressure Level
OHC	Outer Hair Cells
IHC	Inner Hair Cells
GLP-1	Glucagon-like peptide-1
GLP-1R	Glucagon-like peptide-1 Receptor
SEM	Scanning Electron Microscopy
HPD	Hearing Protection Device
SV	Scala Vestibuli
SM	Scala Media
ST	Scala Tympani
ABR	Auditory Brainstem Response
TBI	Traumatic Brain Injury
AHAAH	Auditory Hazard Assessment Algorithm for the Human Ear

Chapter 2 3D Finite Element Modeling of Blast Wave Transmission from the External Ear to a Spiral Cochlea

2.1 Introduction

Hearing loss and tinnitus are common disabilities among veterans and active-duty military personnel, and although conservation programs have begun to beneficially affect their hearing health, hearing loss and tinnitus persist as the top disabilities treated by Veteran Affairs.[11,18,58] Service men and women are at an increased risk for hearing loss from blast-related ear injuries due to working and being deployed to environments where BOPs are frequent.[18,62,102] BOP exposure damages the middle and inner ear, and while multiple techniques exist to observe and treat middle ear injuries, the mechanisms of inner ear blast-related injuries, such as cochlear synaptopathy and hair cell loss, are neither well understood nor observed non-invasively.

Various studies have experimentally shown that the TM and stapes experience extreme displacements and the cochlea and BM exhibit high pressures during blast and intense noise exposure.[34,35,44,45] Dual laser Doppler vibrometry (LDV) techniques were used to monitor the motion of the TM during blast exposure measuring displacements much higher than that during typical sound exposure,[31,45,108] and structural damage and altered surface motion of the TM were observed post-blast exposure.[19,25] Jiang et al.[44] showed that the TM's motion transmits to the stapes by measuring the displacement of the SFP with LDV, and results revealed high SFP movement during exposure corroborating a previous study by Greene et al.[35] where the authors measured the elevated SFP motion and cochlear pressure during intense low-frequency sound. The intracochlear pressure during BOP exposure has only recently been measured experimentally to reveal

pressures within the cochlea that would undoubtedly cause damage to the tissue within the cochlea.[34] Recent advancement in experimental studies have provided an early insight to the transmitted energy into the cochlea through measurements of the displacements in the middle ear and the intracochlear pressure at the base of the cochlea; however, the BM's motion during blast exposure has not been empirically measured due to the harsh experimental environment and the degree of precision needed to measure BM displacement.

With the difficulty of observing BM motion experimentally hindering progress for understanding cochlear mechanics during BOP exposure, researchers have adapted computational models of the ear to simulate blast transmission in the ear.[6,73,76] A recently published study[6] modeled blast transmission from the external ear canal to a straight, 2-chamber cochlea in a three-dimensional (3D) finite element (FE) model of the human ear which augmented a previous experimentally validated, blast model of the middle ear by Leckness et al.[54] Brown et al.'s[6] model predicted the large displacements of the BM and the high intracochlear pressures comparable to published measurements of cochlear pressure during blast exposure.[34] Other computational models, like the Auditory Hazard Assessment Algorithm for Humans (AHAAH) model,[76] have been developed to predict the potential harm from high pressure inputs to the inner ear and the victim's overall hearing health by simulating the input energy to the cochlea or the displacement of the BM.[73] While current advancements make progress in understanding cochlear mechanics during BOP or intense sound exposures, the models of the ear consider the BM in the widely used straight cochlear configuration and do not consider the effect the cochlea's spiral geometry has on the pressure transmission and BM displacement during BOP

exposure.[74] Straight cochlea models have been good approximations for cochlear mechanics during acoustic simulations, but differences in pressure distributions do exist between spiral and straight cochlea models. While this does not significantly alter the BM frequency tuning, significant discrepancies between the two types of models may occur when the cochlea experiences high pressures during blast exposure.[85]

In the present article, we report the development of a 3D FE model of the entire human ear to simulate the transmission of BOP wave from the ear canal through the middle ear and into a spiral cochlea to determine the effect from the cochlea's spiral structure during blast exposure. The FE model was validated with the experimental data obtained in human temporal bones (TBs) which includes the pressure near the TM in the ear canal when the experimentally measured blast pressure was applied at the ear canal entrance in the model. The displacements of the middle ear ossicles (e.g., SFP) and cochlea BM and the intracochlear pressures were derived from the model, and the BM displacements were compared to displacements simulated in a straight cochlea model. In this study, we aim to provide a more anatomically accurate computational tool for the prediction of blast wave transmission from the ear canal to the cochlea and for future applications for assisting the prevention, diagnosis, and treatment of blast-induced hearing loss.

2.2 Materials and Methods

2.2.1 FE Model of the Human Ear

The FE model of the entire human ear was created based on the model reported by Brown et al.[6] and used the spiral cochlea structure from Gan et al.[32]. The outer and middle ear was constructed from histological cross-sectional images of a human TB (left

ear, 55-year-old, male),[24] and the spiral cochlea with two and a half turns was also from histological cross-sectional images in a different male human TB (left ear, 52-year-old)[32]. The resulting middle ear and cochlea geometries were originally meshed in Hypermesh 13 (Altair Engineering, Inc., Troy, MI) and ANSYS (ANSYS Inc., Canonsburg, PA), respectively. For this model, the straight, 2-chamber cochlea from Brown et al.[6] was replaced with a 2-chamber, spiral cochlea and connected to the SFP and round window membrane (RWM). The cochlea was remeshed in Hypermesh 13 with pyramid and tetrahedral elements to improve performance in transient, high deformation analyses in the time domain.

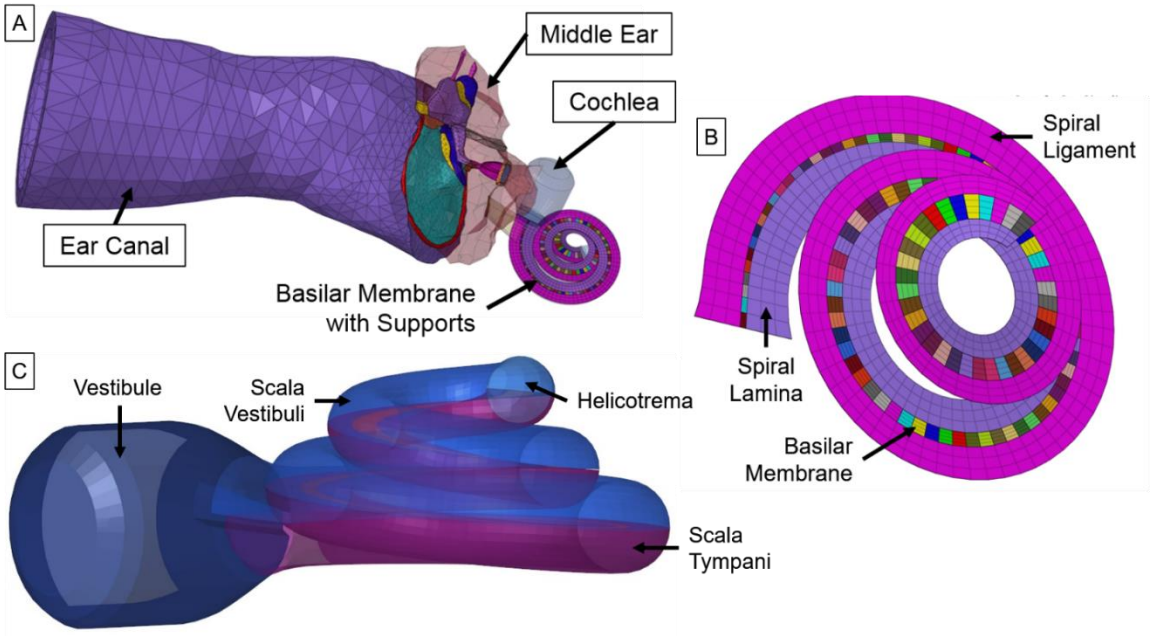

Figure 2-1 (A) FE model of the human ear with the ear canal, middle ear, and spiral cochlea. (B) The cochlea's spiral BM mesh surrounded by two supports (spiral lamina and spiral ligament). (C) Cochlea fluid volumes: Vestibule, Scala Vestibuli, Scala Tympani, and Helicotrema.

The developed ear model consisting of the meshed ear canal, middle ear, and cochlea can be seen in Figure 2-1A. The middle ear consisted of the ossicles and their suspensory ligaments and tendons, pars flaccida and pars tensa of the TM, TM annulus

(TMA), manubrium, incudomalleolar and incudostapedial joints (IMJ and ISJ respectively), stapedial annular ligament (SAL), and middle ear cavity. The spiral cochlea had two chambers, scala vestibuli (SV) and scala tympani (ST) above and below the BM, respectively, with a vestibule volume between the SV and SFP (Figure 2-1A and Figure 2-1C). The BM separated the SV and ST fluid chambers with two supporting structures (spiral lamina and spiral ligament) (Figure 2-1B). The BM was 32 mm in length and separated into 124 portions with varying material properties. The resulting meshes for the ear canal, middle ear, and cochlea contained 19,522, 48,376, and 139,542 elements, respectively.

2.2.2 Material Properties of Structural Components and Boundary Conditions

The structural components of the outer, middle, and inner ear had similar boundary conditions and material properties as mentioned in Brown et al.[6]. The standard linear viscoelastic model[22] in ANSYS was assigned to the TM, TMA, IMJ, ISJ, SAL, and RWM of all middle ear soft tissues with the Prony shear relaxation modulus:

$$G(t) = G_0 \left[\alpha_\infty^G + \alpha_1^G \, e^{-t/\tau_1}\right] \quad (1)$$

where G_0 is the shear relaxation modulus at t = 0, α_∞^G is the relative long-term modulus, α_1^G and τ_1 are the first-order relative modulus and relaxation time, respectively. The material properties reported in Table 1 of Zhang and Gan[112] were used to determine the values in Equation (1) by converting the stated Young's modulus (E) into shear modulus (G):

$$E = 2G(1 + \nu) \quad (2)$$

where ν is the Poisson's ratio of the material. The ossicles, suspensory ligaments and tendons, and manubrium were modeled as isotropic elastic materials as reported by Gan

et al.[28]. The ear canal skin was modeled as an isotropic elastic material with a Young's modulus of 0.42 MPa, density of 1050 kg/m^3, a Poisson's ratio of 0.43, and a beta damping coefficient of 4.48 x 10^{-5} s. Fixed boundary conditions were set to the outside skin of the ear canal, and the TMA, RWM, SAL, and suspensory ligaments and tendons where they met the bony wall of the ear.

Similar to Brown et al.[6], the material properties varied along the length of the BM's 124 sections with a Young's modulus that changed linearly per section along the BM's length from 50 MPa at the base to 15 MPa in the middle to 3.75 MPa at the apex with a density and Poisson's ratio of 1200 kg/m^3 and 0.3, respectively. The β damping of the BM changed linearly from 2.0 x 10^{-4} s at the base to 9.748 x 10^{-4} s at the apex. The width and thickness of the BM elements changed linearly from 126.6 and 8.46 μm, respectively, at the base to 497 and 2.54 μm, respectively, at the apex, and the BM's mesh included 496 eight-node hexahedral elements, four elements per section. The spiral lamina and apex bony supports were assumed to have a Young's modulus of 14.1 GPa, density of 1200 kg/m^3, Poisson's ratio of 0.3, and β damping of 1.0 x 10^{-4} s, and the spiral ligament was assigned similar properties except with a Young's modulus of 5 MPa and a density of 1000 kg/m^3.[28] All the BM support structures were fixed in place to give the BM a fixed boundary condition along its edges.

2.2.3 Fluid Properties and Boundary Conditions

As with the structural components, the fluid domains of the model (Figure 2-1A and Figure 2-1C) were set to similar parameters as in Brown et al.[6], and simulation of the fluid domains was modeled with ANSYS Fluent. The ear canal and middle ear cavity fluid domains were assigned as air that was a compressible ideal gas at sea level with the

ambient air pressure set to 101,325 Pa, and the perilymphatic fluid inside the cochlea was assigned an initial density of 998.2 kg/m^3 and a viscosity of 1.003 x 10^{-3} kg/m-s. The structural components of the ear were set to interact with their adjacent fluid domains through fluid-structure interfaces (FSIs): the inner surface of the ear canal, medial and lateral surfaces of the TM, SFP, cochlea, and middle ear cavity facing surfaces of the RWM, and SV and ST facing surfaces of the BM. All remaining walls were assigned as stationary, rigid walls, and all fluid domain walls were defined with a no-slip boundary condition.

2.2.4 FE Analysis

The FE analysis of the structural components was modeled with ANSYS Mechanical and the fluid dynamics was modeled with Fluent within ANSYS Workbench v19.1 which transferred the forces and displacements of the FSIs through a coupled analysis. The blast simulation ran for a blast duration of 2 ms with a time step of 1 µs for the nonlinear, transient simulation. Both ANSYS Mechanical and Fluent were set to calculate the large deformations of the FSIs that occur during blast exposure, and the deforming fluid domains implemented a remeshing and smoothing function to ensure high mesh quality during simulations.

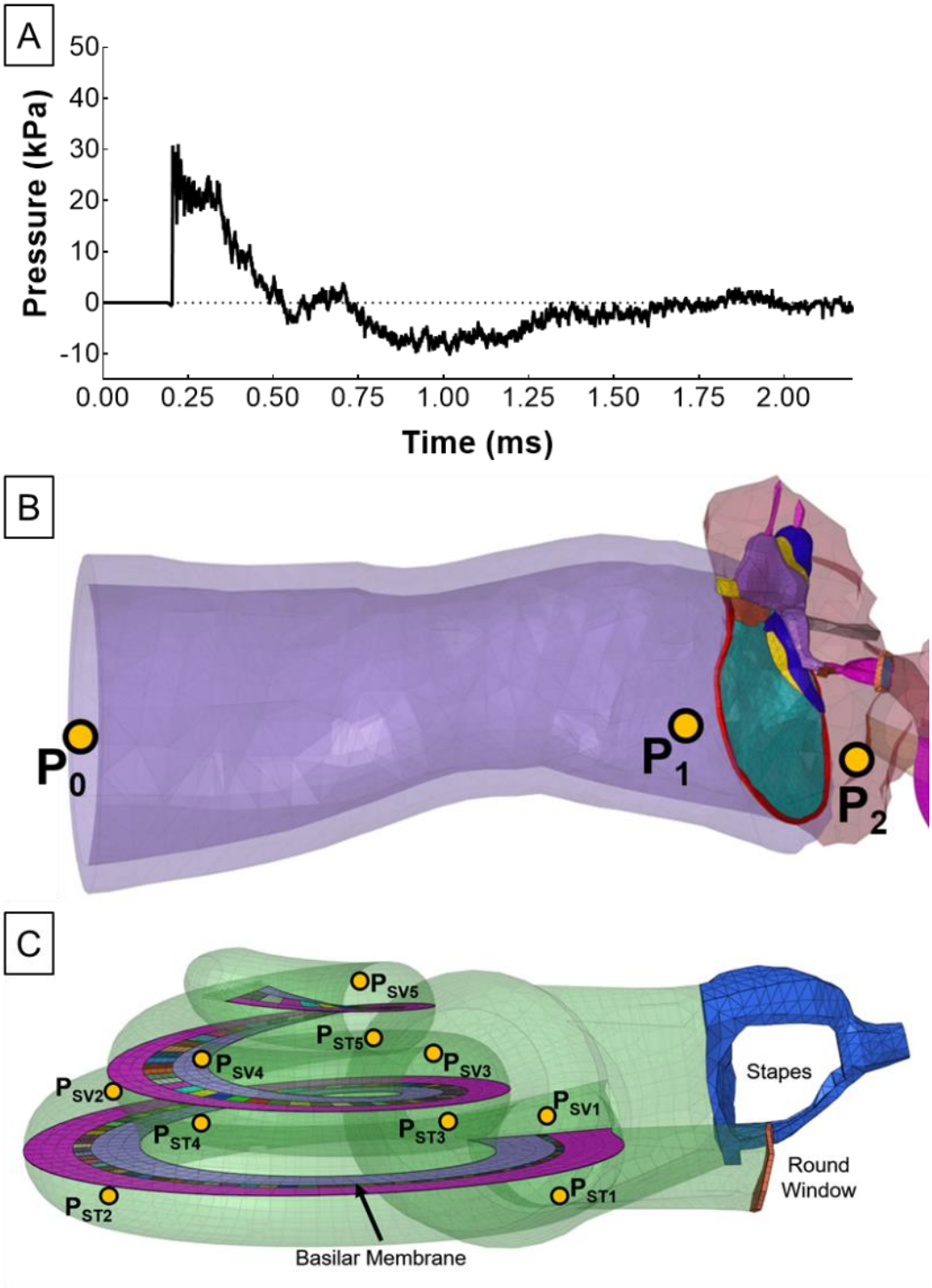

Figure 2-2. (A) Experimentally measured BOP used as input for the FE model at P0. (B) Input location for BOP at entrance of ear canal, P0, and locations in FE model monitored for pressure in the middle ear (P1 and P2). (C) Pressure monitor locations in the cochlea during simulations (P_{SV1} - P_{SV5} and P_{ST1} - P_{ST5}).

Experimental BOP waveforms, collected from cadaveric TB blast tests,[45] were used as the input BOP waveform at the entrance of the ear canal (P0), and 2 ms of the pressure waveform used is shown in Figure 2-2A, 30.7 kPa (4.45 psi) peak pressure. Figure 2-2B illustrates the location of P0 where the model's input was applied. Various locations throughout the model were monitored for pressure to track blast wave transmission in the ear (Figure 2-2B and Figure 2-2C): near the TM in the ear canal (P1), behind the TM in the middle ear cavity (P2), and five points in both the SV and ST along the BM from the base to the apex (P_{SV1} - P_{SV5} and P_{ST1} - P_{ST5}, respectively). The additional model-derived results include the displacements of the SFP and BM.

2.2.5 Experimental Blast Test with Cadaveric Temporal Bones

The methods used for collecting experimental pressure waveforms in this study were extensively described and diagramed by Jiang et al.[45] and Leckness et al.[54]. In short, fresh human cadaver TB with no observable ear damage had a pressure sensor (Model 105C002, PCB Piezotronics, Depew, NY) surgically inserted into the ear canal near the TM (P1) and was mounted inside an anechoic chamber to a "head block" placed under a blast apparatus designed for open-field blasts. The P0 pressure sensor (Model 102B16, PCB Piezotronics, Depew, NY) was mounted 1 cm lateral to the entrance of the ear canal. The BOP was generated by bursting a polycarbonate film (McMaster-Carr, Atlanta, GA) with compressed nitrogen gas. A data acquisition system using a cDAQ 7194, A/D converter 9215 (National Instruments Inc., Austin, TX), and LabVIEW Signal Express software (National Instruments Inc., Austin, TX) was used to record and synchronized measurements from the pressure sensors.

2.2.6 Model Validation with Experimental Results

The P1 pressure waveforms were used to validate the FE model when compared to the experimental results. Similar to Leckness et al.,[54] the P1 waveform's intensity and peak wave shape were used to compare the results by analyzing the peak pressure level, P1:P0 peak pressure ratio, and A-duration. The A-duration is defined as the measure of time (in ms) the positive portion of the peak pressure is sustained, and the B-duration is the time interval between the BOP peak pressure and the last value within 20 dB of the peak. A pressure waveform duration of 20 ms, sampled at 1 MHz, was used for these calculations (Figure 2-2A for the first 2 ms of pressure waveform). The percent error was used to compare the P1:P0 ratio and P1 A-duration between the experiment and model data. The model's TM and SFP displacements were compared to published data where available.

2.3 Results

Figure 2-3A and Figure 2-3B present the pressure waveforms recorded in a TB blast test and calculated from the FE model, respectively. The P0 waveform with a peak pressure of 30.7 kPa had an A-duration of 0.307 ms and a B-duration of 9.792 ms. The P1 peak pressure for the model was 64.0 kPa with a P1:P0 ratio of 2.08, and the P1 peak pressure from the experiment was 58.6 kPa with a P1:P0 ratio of 1.91 which gives a 9.2% error. The A-durations for the model and experimental P1 pressure waveforms were 0.154 and 0.175 ms (12.0% error), respectively. It should be noted that P0 was measured at 1 cm from the ear canal entrance, while the FE model applied the P0 input pressure on the inlet face of the ear canal. Our blast chamber is designed for open-field blast tests, and it is subject to the phenomenon that the air velocity and pressure generated from

blasts delay with increased distance despite sound pressure traveling at the speed of sound.[15] This resulted in a faster time of arrival of the P1 peak pressure for the model than that shown in experimental blast tests. Despite the difference, the model-predicted P1 waveform agrees well with the experimental waveform as shown by Figure 2-3C which compares the two P1 waveforms (pressure rise-times have been aligned for a better comparison). The middle ear cavity pressure at P2 was not measured during blast tests by Jiang et al.[45] from which the experimental results in this study originated. Only the model-derived P2 pressure is shown in Figure 2-3B. The model-derived P2 waveform in Figure 2-3B exhibits a typical reduction of peak pressure across an intact TM with a peak pressure of 9.3 kPa inside the middle cavity compared to a P1 peak pressure of 64.0 kPa on the lateral side of the TM. The use of a spiral cochlea did not significantly change middle ear pressures when compared to that in previous models that utilized a cochlear load mass or a two-chamber straight cochlea.[6,26,54]

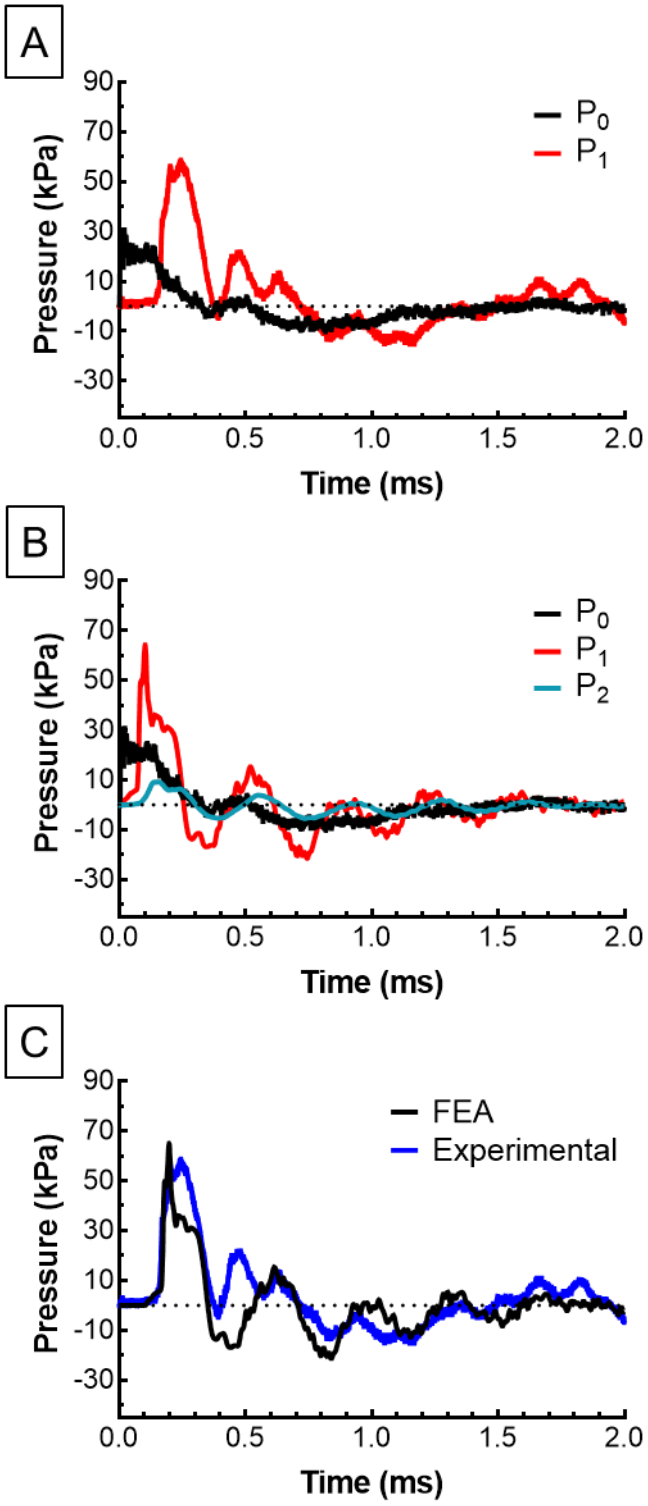

Figure 2-3. (A) Experimental measures of P0 and P1 during BOP. (B) The FE model's simulated pressures for P1 and P2 with P0 as input. (C) Comparison between FE model and experimental pressures of P1.

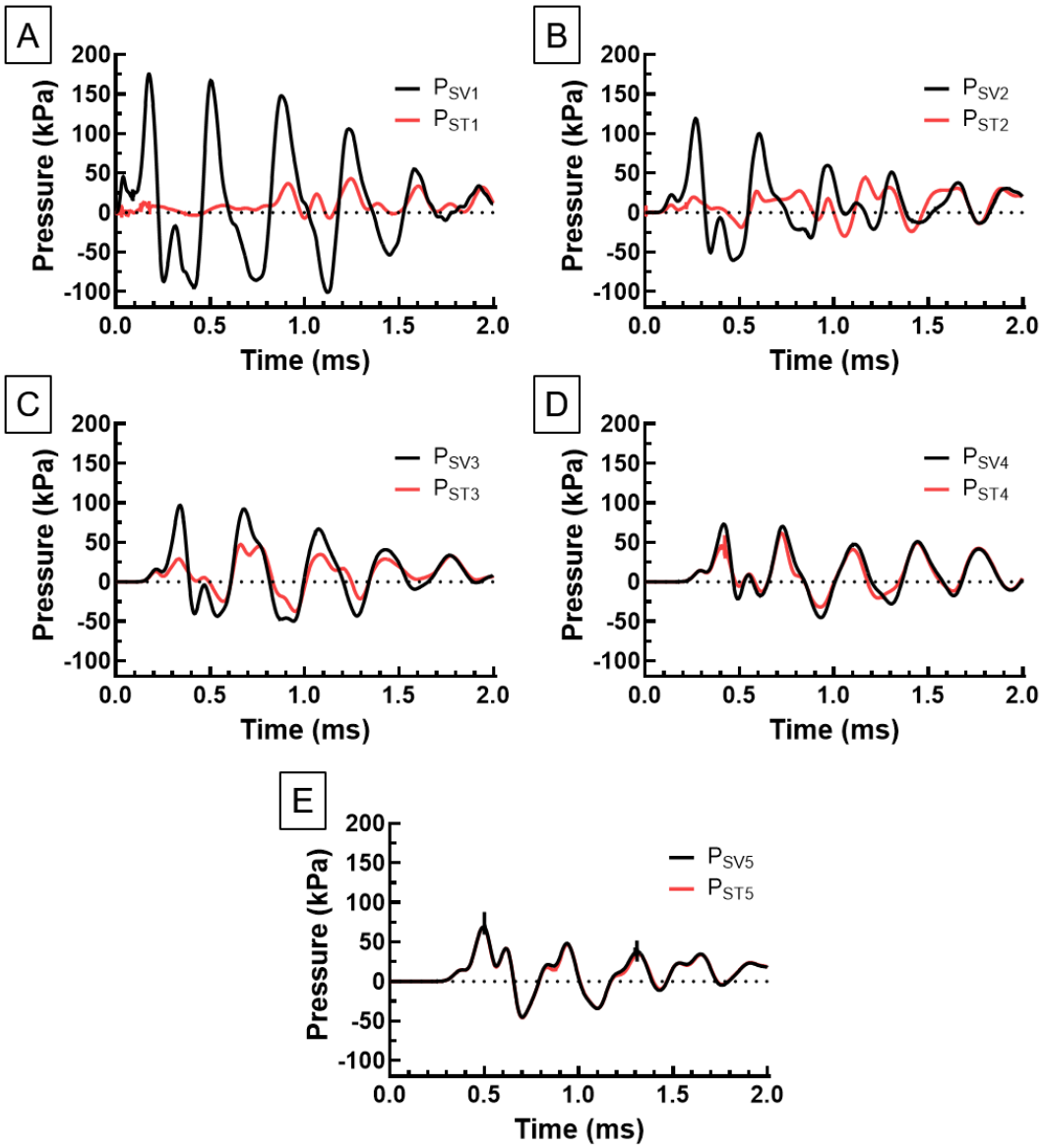

Figure 2-4. Pressures along the cochlea from base to apex during blast exposure. Pressures monitored in the scala vestibuli (P_{SV}) and scala tympani (P_{ST}) at 2.5, 13, 18.0, 23.25, and 28.25 mm from the base of the cochlea (A, B, C, D, and E, respectively).

Figure 2-4 shows the cochlear pressures at various locations in the SV (P_{SV1}-P_{SV5}) and ST (P_{ST1}-P_{ST5}) from the base to the apex (shown in Figure 2-2C): 2.5 (A), 13 (B), 18 (C), 23.25 (D), and 28.25 (E) mm from the base of the BM. Maximum peak pressures in the SV (black lines) were 175.2, 119.1, 96.8, 72.9, and 85.4 kPa at P_{SV1}, P_{SV2}, P_{SV3}, P_{SV4}, and P_{SV5}, respectively, and the maximum pressure within the ST (red lines) were 42.7,

44.2, 47.1, 61.4, and 68.2 kPa at P_{ST1}, P_{ST2}, P_{ST3}, P_{ST4}, and P_{ST5}, respectively. As illustrated by Figure 2-4, the maximum pressure within the SV of the cochlea decreases from the base to the apex with the inverse true for the ST. A trend in the model was observed where the pressure waveforms decreased in magnitude difference the closer to the apex which was also observed in a previous straight cochlea model[6] with the greatest pressure difference between the SV and ST being 174.0 kPa near the base (2.5 mm; Figure 2-4A) and decreasing to 17.8 kPa near the apex (28.25 mm; Figure 2-4E). The greatest positive and negative pressures of 175.2 kPa at 0.175 ms and -100.9 kPa at 1.122 ms, respectively, were observed in the SV at 2.5 mm from the base (P_{SV1}; Figure 2-4A).

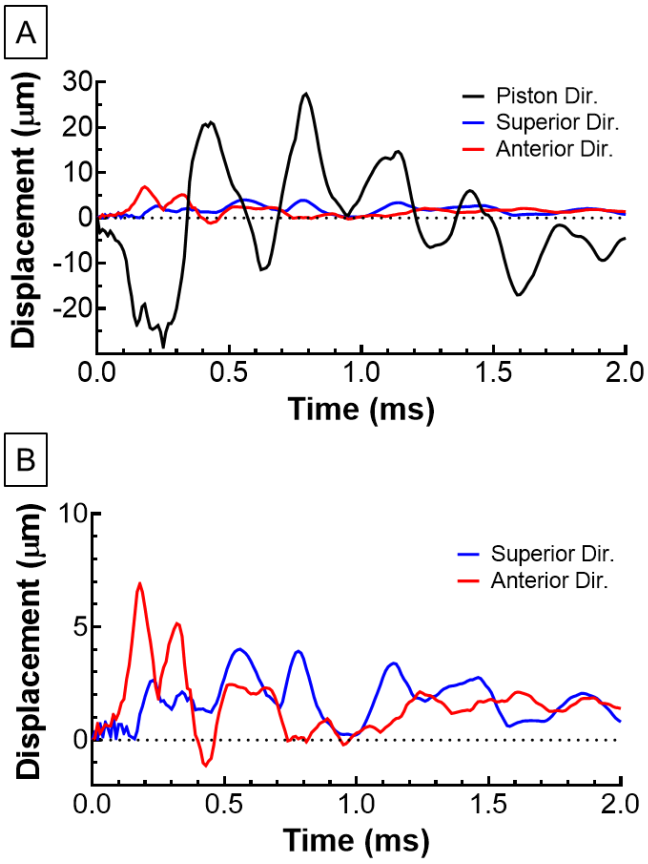

Figure 2-5. (A) Model-derived stapes displacement in the piston, superior/inferior, and anterior/posterior directions from BOP exposure. (B) Model-derived stapes displacement in the superior/inferior, and anterior/posterior directions, emphasizing the difference in magnitude between the stapes' piston and rocking movements.

The motion of the SFP can be seen in Figure 2-5 where the displacement of the SFP plane is plotted in three directions (piston, anterior, and superior) over a 2 ms time duration. The piston direction is the direction normal to the SFP plane where the negative direction would be into the cochlea. The anterior and superior directional movements are the rocking motions of the SFP plane in the anterior-posterior and superior-inferior directions, respectively. The greatest displacement magnitude was 28.5 μm into the cochlea (negative) at 0.25 ms with the largest positive displacement of 27.4 μm at the second maximum peak at 0.79 ms (Figure 2-5A). The first two peak-to-peak displacements (49.5 and 38.8 μm for the first and second, respectively) seem to have the greatest impact on the cochlear pressure since the cochlear pressure in the base quickly diminishes after 1 ms (Figure 2-4A). Figure 2-5B plots the superior and anterior directional movements of the SFP at a smaller range due to the magnitude of their displacements being much smaller than the piston direction displacements. The maximum displacements for the superior and anterior directions were 4.0 μm at 0.56 ms and 6.9 μm at 0.18 ms, respectively, which were more than four times less than the maximum magnitude in the piston direction. Even though these displacements were small when compared to the piston direction, all of the displacements were much larger than the SFP displacements during low-frequency sound stimuli at 90 dB sound pressure level (SPL) (<0.1 μm).[31]

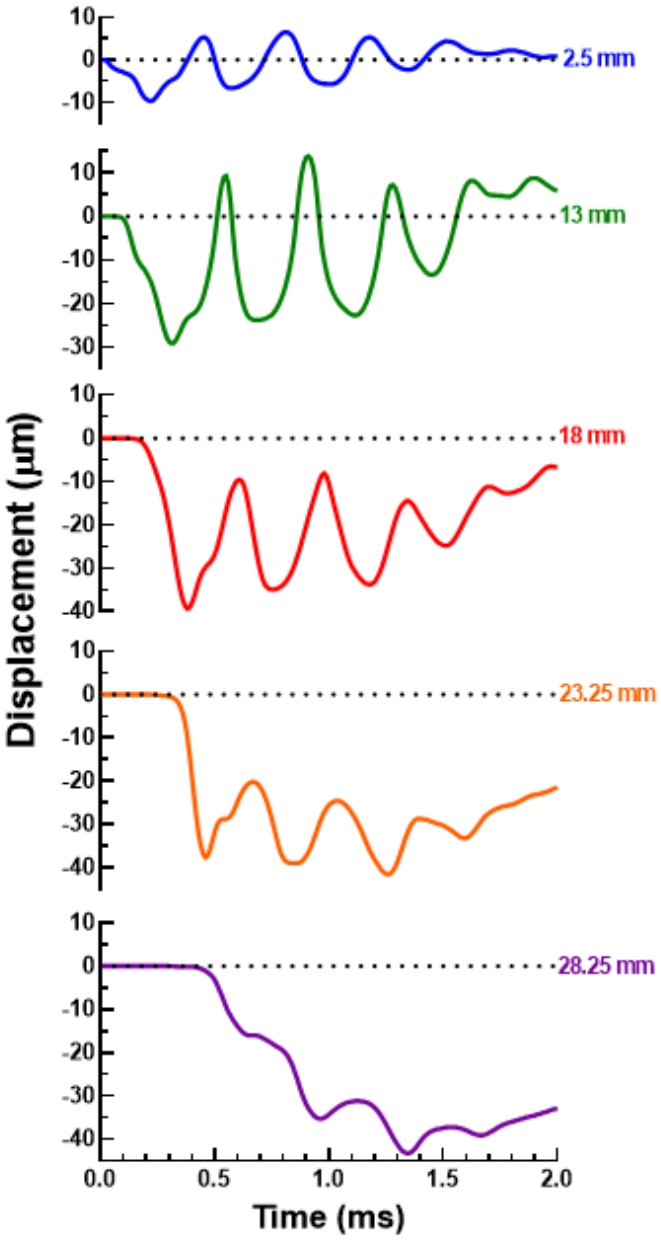

Figure 2-6. Model-derived displacements of the BM at 2.5, 13, 18, 23.25, and 28.25 mm from the base of the cochlea.

Figure 2-6 shows the displacement of the model's BM over 2 ms at 2.5, 13, 18, 23.25, and 28.25 mm from the base of the cochlea, and the maximum displacements at these points were -9.7, -29.1, -39.4, -41.6, and -43.2 µm, respectively, with a negative value indicating displacement downward towards the ST normal to the plane of the BM.

The maximum upward displacements were 6.5, 15.9, 14.4, 2.6, and 0.0 µm, respectively, over the 2 ms time duration. The results show the BM motion near the base was closely tied to the cochlear pressure generated by the SFP (Figure 2-4A), and the motion of the BM was more centered around the origin than the motion of the BM further away from the base. While the cyclic wave response can be seen in the BM away from the base, a negative broad peak formed in the BM and grew with increasing distance from the base of the BM. This reflected a passive, low frequency traveling wave often discussed with BM inner ear mechanics,[83,97] and interestingly, such a prominent traveling wave effect was not observed in a previous blast model.[6]

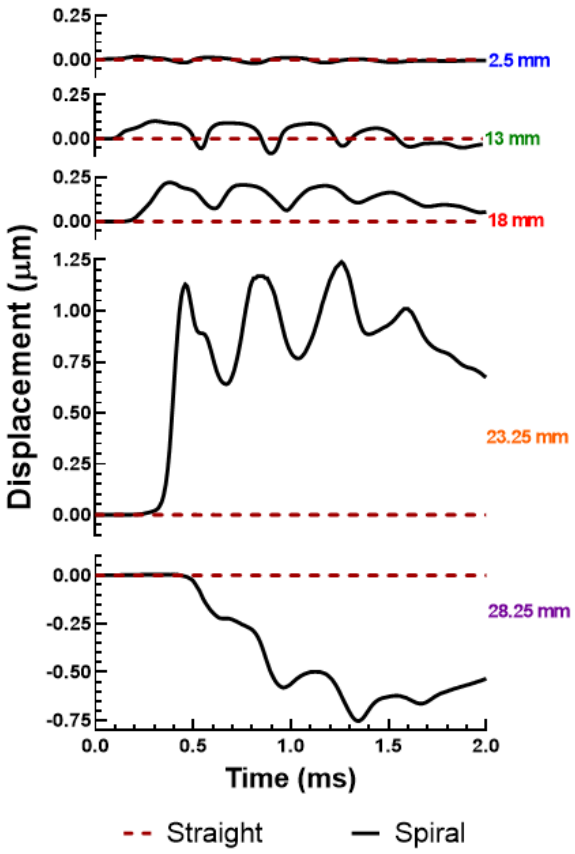

Figure 2-7. Comparison of the transverse displacements of the BM at 2.5, 13, 18, 23.25, and 28.25 mm from the base of the spiral cochlea and the straight, 2-chamber by Brown et al.[6]

To illustrate the effect a spiral cochlea has on the BM response, Figure 2-7 plots the transverse displacement of the BM from the spiral cochlea model and compares it to that from the straight cochlea model reported by Brown et al.[6]. The BM transverse motion is the direction perpendicular to the length of the BM element with the positive motion being toward the center of the cochlea's spiral. The maximum displacements for each position along the length of the BM (2.5, 13, 18, 23.25, and 28.25 mm) were -0.02, 0.10, 0.22, 1.24, and -0.75 μm, respectively. The trend of the transverse motion in the BM mirrored the BM's motion shown in Figure 2-6 except for at 28.25 mm where most of the motion was away from the center of the cochlea; however, the transverse displacement of the BM was about two magnitudes less than the normal displacement of the BM. While the transverse displacement was far less than the normal displacement, it was much greater than the transverse displacement simulated by the straight two-chamber cochlea model reported by Brown et al.[6] which the max displacement was 0.59 nm and the typical displacement was less than 300 pm. In addition, the transverse motion of the basilar membrane was greater than normal directions displacements measured during acoustic simulation (<10 nm at 120 dB).[71]

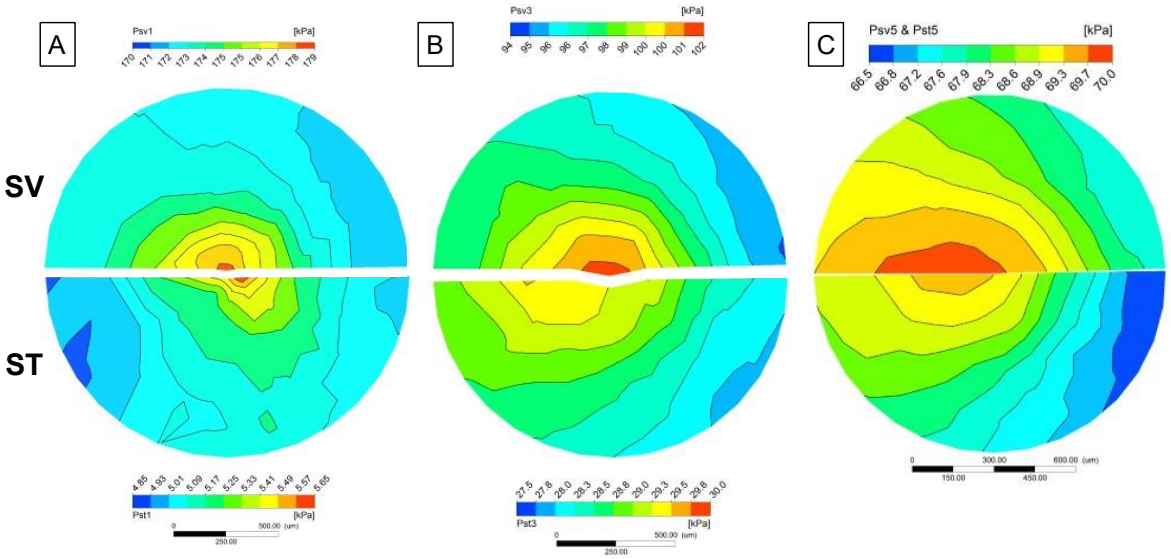

Figure 2-8. Pressure contour plots of SV and ST of the spiral (A-C) two-chamber cochlea models. Plots illustrate the pressure distribution at planes perpendicular to the perilymph flow in the cochlea at 2.5 (A), 18 (B), and 28.25 mm (C) from the base of the BM. Pressure distributions are from the first pressure peak at the respective locations. Note that the SV and ST plots of A and B have separate legends for the pressure distribution due to the large difference in pressure range between the two chambers.

The pressure distribution within the SV and ST of the spiral cochlea (pressure contour plot) is shown in Figure 2-8 (A-C) at three different positions along the BM at the base (2.5 mm), middle (18 mm), and apex (28.25 mm) turns. The time point for each pressure contour is the time at which the first maximum peak pressure occurred at the respective position. It is important to note the pressure contours for the basal (Figure 2-8A) and middle (Figure 2-8B) turns have separate pressure scales due to the large difference in pressure ranges between the SV and ST chambers. The right side of the contour plots are toward the center of the spiral cochlea. As seen in Figure 2-8, the increase in pressure distribution asymmetry is apparent from the base to the apex of the cochlea. The base of the cochlea shows minimal symmetry across the width of the cochlea with a pressure variation of less than 3 kPa between the left (outer) and right (inner) sides of the SV (Figure 2-8A). When the first pressure peak occurs at the apex

(Figure 2-8C), the pressure distribution was completely asymmetric across the width of the spiral cochlea with the higher pressure skewing to the outer curve of the cochlea. The increase in asymmetry across the BM in Figure 2-8C correlates to the increased transverse displacement of the BM beyond the base of the cochlea (Figure 2-7). The pressure difference between the outer (left) and inner (right) curve of the cochlea was less than 3, 4, and 2.1 kPa for the basal, middle, and apex turns of the SV, respectively, and 0.24, 1.2, and 2.4 kPa for the basal, middle, and apex turns of the ST, respectively.

2.4 Discussion

2.4.1 Spiral Cochlea Effect and Model Comparison

Blast models of the human body aim to predict and assess the damage sustained during blast exposure as a final goal, and models of the auditory system attempt to predict the long-term hearing loss caused by BOPs.[6,20,73,77] The AHAAH model was such a model that has been incrementally improved since the early 1990s to an easy-to-understand program that analyzed a sample pressure waveform and attempted to predict the possible long-term hearing loss with a simple output.[20] Mathematical models like the AHAAH model are created from data obtained from animal experiments then are converted to a human model through patient data.[76–78] These models do continue to improve as more data becomes available; however, these models are intrinsically unable to model the complex fluid dynamics within the cochlea during blast exposure. Studies have shown that, even under normal sound stimuli, the spiral shape of the cochlea has an effect on the fluid dynamics and pressure distribution within the cochlea when compared to a straight cochlear model[59,85,113] and would undoubtedly have an effect during BOP exposure. Advancing blast models of the peripheral auditory system to include the spiral

shape of the cochlea is a necessary step to accurately represent the cochlear response during blast.

The blast model by Brown et al.[6] is the most relevant study for comparing the cochlear response between straight and spiral cochlea models. By utilizing the same experimental BOP as input for P0, it was found that there were no significant changes in the pressures of the middle ear and displacement of the TM. The spiral cochlea did change the resulting displacement of the SFP when compare to the straight cochlea. The overall trend of the SFP piston motion and initial displacement into the cochlea were very similar (-28.5 and -27.5 μm for the spiral and straight cochlea, respectively); however, the following maximum peaks after the initial minimum were less than half the magnitude of the maximum SFP displacement reported by Brown et al.[6]. Furthermore, the initial anterior directional movement was greater for the spiral cochlea model, but overall displacement magnitudes were similar. When compared to Jiang et al.'s SFP measurements during blast exposure,[44] the frequency trend of the SFP motion was similar between the model and experimental results in that the stapes sharply displaced between the positive and negative peaks; however, the magnitude displaced was greater for the experimentally measured SFP despite the same BOP waveform (TB sample 18-1L in Jiang et al.[44]) being used for P0 in the model.

As previously mentioned, the BM of the spiral cochlea exhibited a broad negative peak that grew as the pressure transmitted from the base to the apex. This was not observed to this degree in the BM reported by Brown et al.[6]. The BM displacement of the straight cochlea model was smaller in magnitude and the cyclic motion centered around the origin throughout most of the cochlea. In addition, the BM fluctuations that originated

at the base persisted and grew in magnitude until near the apex where most of the waves combined.[6] The greater BM displacement seen in the spiral cochlea model may be due to the greater intracochlear pressure when compared to the straight cochlea (49.9 and 175.2 kPa for the straight and spiral cochleae, respectively). This was likely due to the smaller cross-sectional area and volume of the spiral cochlea which would increase the resulting pressure from the same amount of input energy from the stapes. Moreover, the pressure distribution differed across the cross-section of the spiral cochlea (Figure 2-8) where straight cochlea models have shown to have a symmetrical pressure distribution across the cochlea.[85] Similar results were observed by Ren et al.[85] where straight and spiral cochlear models were directly compared in an acoustic simulation, and the pressure distribution skewed towards the outer curve of the spiral cochlea while the straight cochlea model exhibited a symmetric pressure distribution. Ren et al.[85] did not find any significant changes in neither the normal nor transverse displacements of the BM; however, the intracochlear pressure were far less than the current study and the boundary constraints of the BM elements did not allow for transvers motion. In the current study, the asymmetric pressure distribution and pressure difference between the SV and ST caused the BM to deform in the transverse direction where the symmetry of the straight cochlea did not allow for much transverse motion (Figure 2-7).

2.4.2 Limitations and Future Work

The lack of experimental intracochlear pressure measurements during blast is a limitation for further validating cochlear blast models, as very few studies have measured cochlear pressure during blast exposure.[34] Greene et al.[34] measured the intracochlear pressure in cadaveric heads in blast conditions, and while this was an important

advancement for the field, intracochlear pressure measurements exhibited large variances within the results showing the need for further research. Previous ear blast models simulated pressures in the cochlea that were within the range of the reported experimental results, but the present spiral cochlea model exceeded that range.[6,34] As mentioned previously, this was likely due to the smaller volume and cross-sectional area of the spiral cochlear chambers when compared to the straight cochlea model by Brown et al.[6]. Future work will compensate for the smaller fluid volume to improve the accuracy of the simulated intracochlear pressure.

Currently, a few studies compare the results between straight and spiral cochlea models to determine the significant effects between the model geometries,[85,86] but a spiral cochlea model has not been used to model blast exposure. Understanding how the spiral shape of the cochlea affects BM motion and BOP pressure transmission throughout the cochlea will help with future developments of a more comprehensive ear blast model. Future work includes developing a three-chambered, spiral cochlea capable of simulation blast pressures from the ear canal entrance to the cochlea. A model with this capability would give insight into how the Reissner's membrane and three chambers affect pressure transmission through the cochlea. In addition, it is unclear if the Reissner's membrane protects the organ of Corti from the initial high pressure increase of the BOP or if it passively transmits pressure to the scala media.

2.4.3 Preliminary Work on Three-Chamber, Spiral Cochlea

Preliminary work has begun to develop the FE ear model with a three-chambered, spiral cochlea for simulation of blast wave transmission from the entrance of the ear canal to the cochlea (Figure 2-9). The developed model was built on the previous work in

Chapter 2 to enhance the cochlear portion of the model. This model is meant to improve the spiral, two-chamber cochlea to a spiral, three-chamber cochlea that includes: the SV, scala media (SM), ST, BM, and Reissner's membrane (RM). This will allow us to analyze how the cochlea's anatomy affects the blast transmission within the cochlea and to investigate the more advanced fluid mechanics from the addition of the SM and RM.

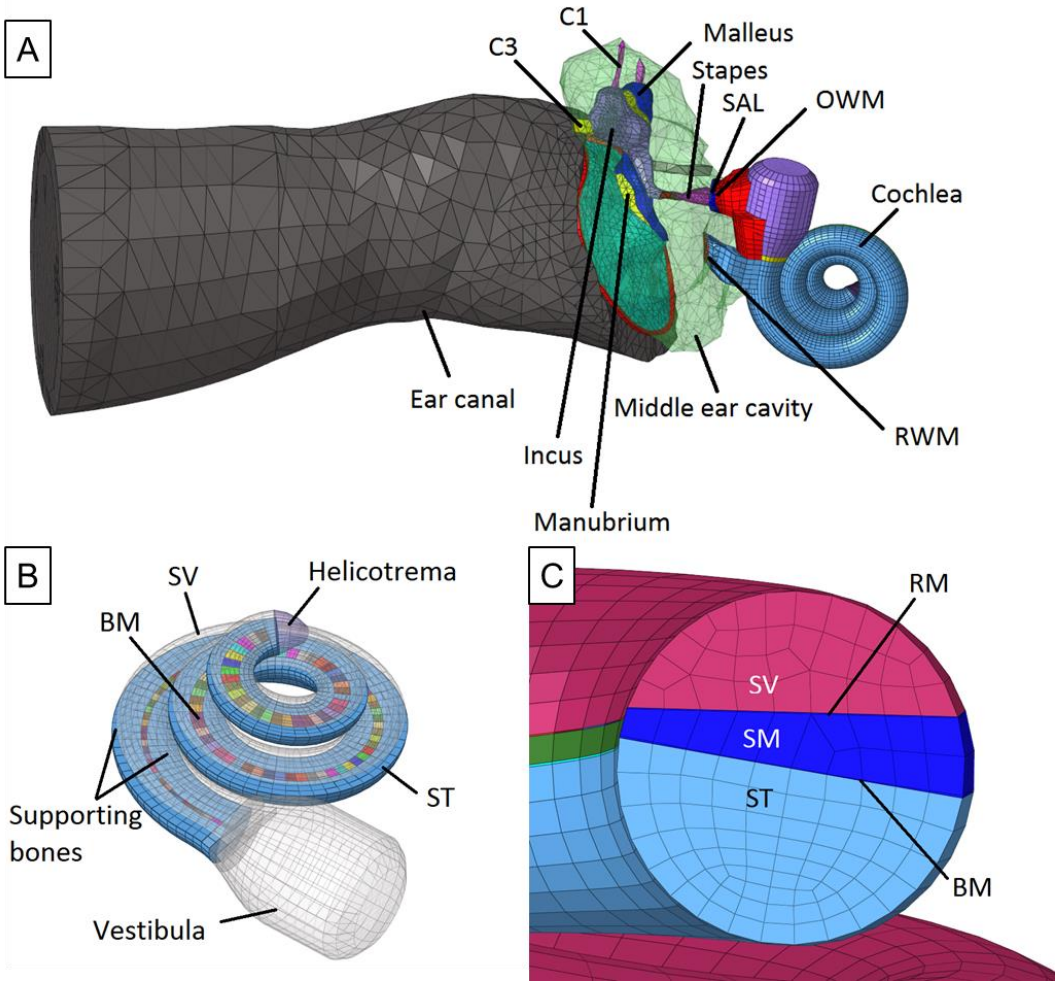

Figure 2-9. (A) 3D FE model of the human ear with spiral cochlea (posterior view). C1 and C3 are the middle ear suspensory ligaments. (B) FE model of the spiral cochlea with BM (SV, SM, and RM are transparent here). (C) Cross-section of the cochlea model displaying the three chambers and two membranes.

Preliminary simulations have been conducted using the same P0 (Figure 2-2) for the model in Chapter 2; however, the response of the RM has been damped while

stability and RM material properties are being improved. The pressure of P1 and P2 for the three-chamber model did not differ significantly from that of the two-chamber cochlea model as the outer and middle ear was identical in both models. Figure 2-10 plots the pressure at the base of the three-chamber cochlea in the SV, SM, and ST. Interestingly, the pressure in the SV and SM were almost the same values throughout the simulation while the ST pressure was much lower, similar to the two-chamber, spiral cochlea model. This was likely due to the large surface area of the RM and its tight coupling to the fluid in the SV and SM where the SM and ST boundary has a much smaller surface area with the BM. Also, the maximum pressure at the base of the three-chamber cochlea was less than half that of the two-chamber with max pressures of 66.9 and 175.2 kPa, respectively.

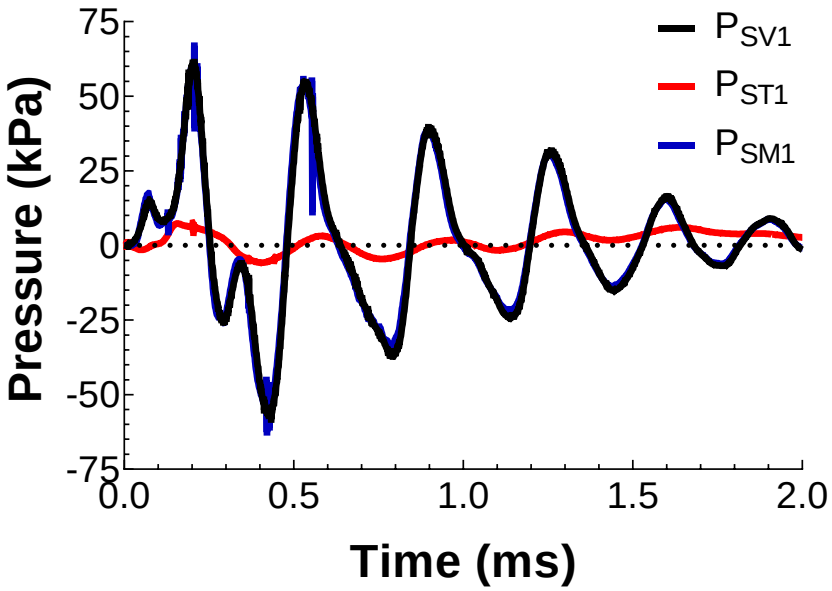

Figure 2-10. Pressure in the cochlea near the base of the BM in the SV (P_{SV1}, black), SM (P_{SM1}, blue), and ST (P_{ST1}, red).

Figure 2-11 shows the displacement of the stapes footplate in the piston direction (movement of the stapes in and out of the cochlea) and the superior and anterior

directions (rocking motion of the stapes). The trend of the stapes footplate motion was very similar to the two-chamber cochlea model with the same trend in the piston direction motion. The maximum displacement magnitudes were higher in the three-chamber model, however. Also, the rocking motion of the SFP decreased with this model. The maximum displacement magnitude for the spiral cochlea was 38.9 μm (negative) where that in the two-chamber cochlea model was 28.5 μm (negative).

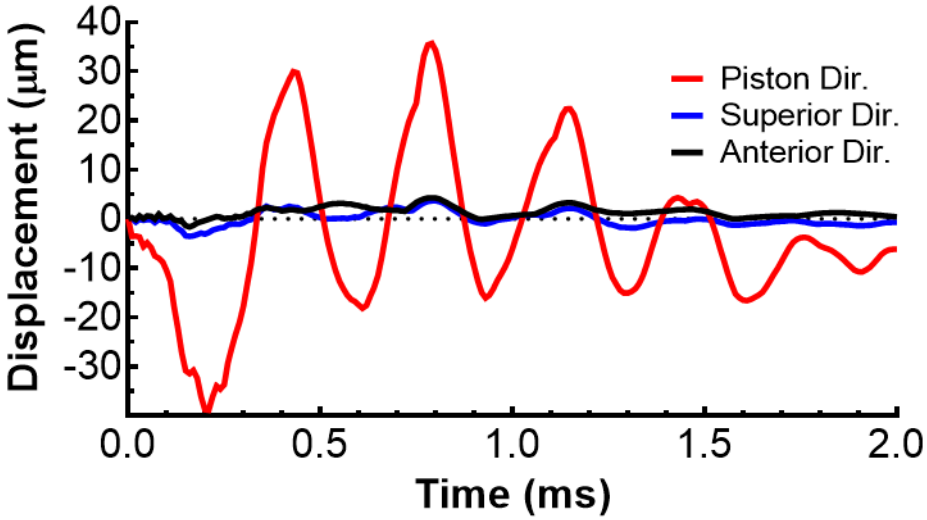

Figure 2-11. (A) Model-derived stapes displacement in the piston, superior/inferior, and anterior/posterior directions from BOP exposure.

Figure 2-12 shows the displacement of the BM at various points along the BM (2.5 to 28.25 mm from the base of the BM). The displacement of BM is in the normal direction of the surface of the BM. The BM displacement of the three-chamber model was more centered around the origin and the effect of the broad, negative low-frequency peak was less prevalent in this model compared to the two-chamber model. Furthermore, the maximum magnitudes were at least 10 μm less for the three-chamber model at distances greater than 13 mm from the base. The maximum displacement of the BM was

28.7 µm (negative) at 23.24 mm from the base. The RM appeared to stabilize the motion of the BM by controlling the variation in pressure in the SV and SM.

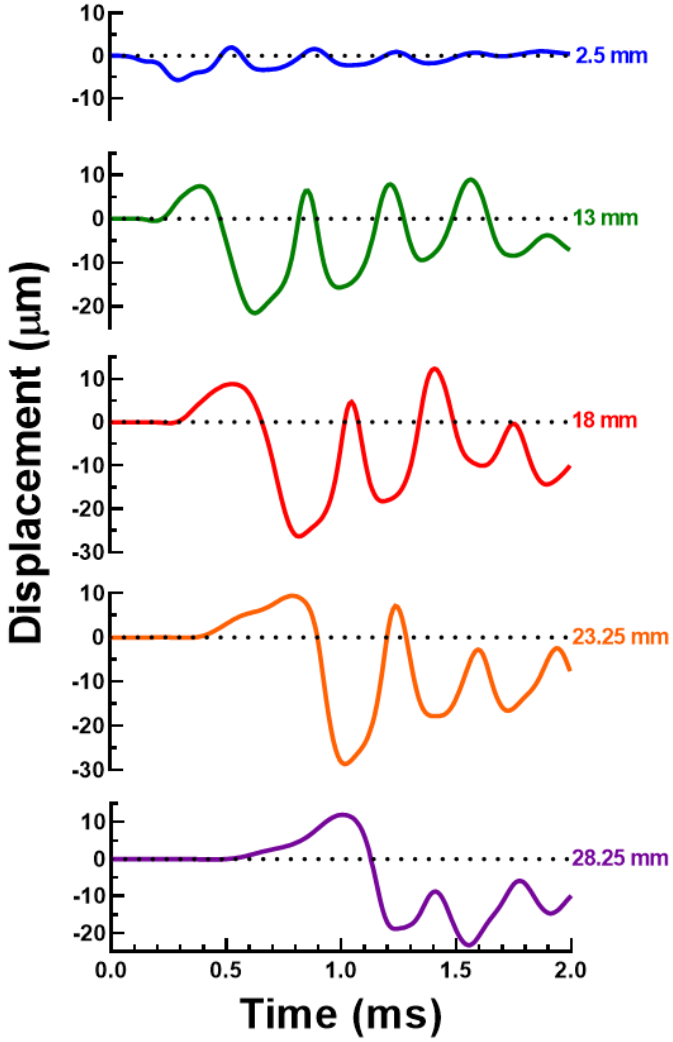

Figure 2-12. Model-derived displacements from the three-chamber cochlea of the BM at 2.5, 13, 18, 23.25, and 28.25 mm from the base of the cochlea.

The displacement of the RM can be seen in Figure 2-13. The motion of the RM was far less than that of the BM after the basal region of the cochlea. At the base of the cochlea (2.5 mm from the base; Figure 2-13), the RM experiences an increasingly negative displacement. Interestingly, this was not seen closer to the apex. This could be due to the strict damping parameters of the RM and the decrease in SV pressure when

compared to the two-chambered model. Future work in this model will include further optimizing the material properties of the RM to achieve a representative response from the membrane and to further analyzed the pressure distribution throughout the cochlea.

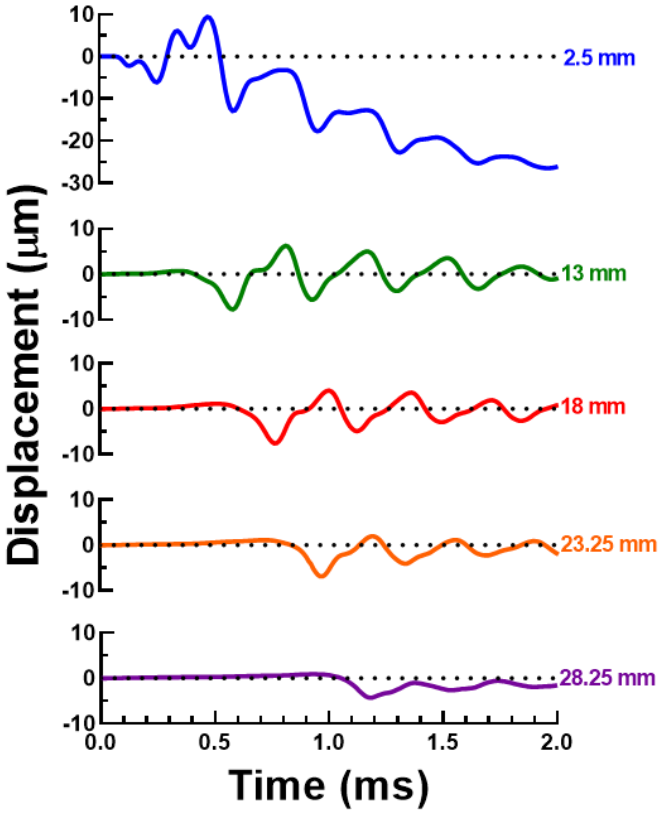

Figure 2-13. Model-derived displacements from the three-chamber cochlea of the RM at 2.5, 13, 18, 23.25, and 28.25 mm from the base of the cochlea.

2.5 Conclusions

A human ear FE model with a two-chamber spiral cochlea was developed and simulated BOP transmission throughout the outer, middle, and inner ear. The BOP input with a peak pressure of 30.7 kPa resulted in large displacements of the stapes which caused high intracochlear pressures and significant BM displacements. The abnormally high SFP displacement had a maximum magnitude of 28.5 μm resulting in intracochlear

pressures as high as 175.2 kPa and BM displacements up to 43.2 μm which both would indicate permanent damage to the cochlea after BOP exposure. The spiral shape of the cochlea caused an asymmetric pressure distribution across the width of the cochlea or the SV and ST chambers and allowed for significant transverse motion of the BM. Preliminary work into the development of a three-chambered, spiral cochlea has begun as well with promising results. The spiral cochlea model developed in this study provides a necessary advancement from the commonly utilized straight cochlea model to increase understanding of the cochlear mechanics during blast exposure, and in doing so, progresses towards a model able to predict the potential hearing loss sustained during BOP exposure.

Chapter 3 A 3D Printed Human Ear Model for Standardized Testing of Hearing Protection Devices to Blast Exposure

3.1 Introduction

Noisy work environments and increased risk of BOP exposure have caused hearing loss to be a prominent disability among veterans.[16,18] Blast-related ear injuries, such as TM rupture and cochlear damage, can result in hearing impairments.[11,23,84] Hearing protection devices (HPDs) are necessary for preventing hearing loss while deployed in hazardous environments, and even though various HPDs are widely available, some troops feel HPDs reduce situational awareness.[18,101] Advanced HPDs have been developed to increase perceived situational awareness and improve uptake of HPDs; however, recent studies indicate the need for further HPD improvement with reliable and efficient testing methodologies.[47,68,101]

Previous studies utilized different computational and experimental methods to investigate the efficacy of HPDs when exposed to noise impulses or BOP.[26,68,101] Utilizing HPDs did attenuate intense impulse noises during human experiments, but early indications of hearing loss were still found emphasizing that assessment of numerous HPD designs in humans would be unethical and cause the subjects long-term harm [47,101]. Human cadaveric temporal bones (TBs) were used to investigate the protective function of different earplugs; however, cadaveric TB models are impractical for thoroughly testing HPD designs during development as they rely on donor availability and TB ear canals' size differences add variability to the results.[26,105] Acoustic test fixtures (ATFs) have been utilized to test insertion loss of HPDs during exposure to impulse noises relevant to a military environment, e.g. gunfire.[68,69] While Murphy et al.[68] did obtain

consistent results when testing HPDs in ATFs, the sound pressure levels (SPLs) used were below that observed in blast exposures where pressure levels could damage expensive ATFs. Computational models offer a cost-effective and time-efficient method of testing HPDs in high-pressure environments, and Gan et al.[26] were able to simulate BOP exposure to their ear model with and without HPDs. While the model provided insight into the ear's response to BOP that could not be measured experimentally, the FE model's results did exhibit some discrepancies when compared to the experimental results demonstrating that physical models for testing HPDs are essential until computational models improve.

Due to the technology's versatility and low cost, 3D printing technology provides an intriguing tool for customized solutions for otolaryngology applications.[40,53,114] 3D printed auricular prostheses and ossicular chain prostheses were used to improve the cosmetic outcome and mechanical function, respectively, of defected or damaged ears in patients, and work has been done to create TM grafts that could aid in restoring the TM to its original structure after tympanoplasty.[40,48,51,114] 3D printed models have the possibility to mimic the ear's function such as in models that simulate mastoid surgery,[66,90] however, 3D printing has not been utilized to create models for the development of HPDs. A model that takes advantage of this technology's benefits could vastly improve the testing and evaluation of HPDs.

In the present article, we report the development of a 3D printed ear model or TB that anatomically and mechanically represented the outer and middle ear for the effective evaluation of HPDs during blast exposure. This 3D printed TB utilized flexible and rigid materials to print the ear canal, TM, middle ear ossicles with suspensory ligaments, and

middle ear cavity, and was created using Gan et al.'s[24] FE model of the human ear. Experiments exposed the 3D printed TB to BOPs with and without HPDs, and results were compared with that from similar experiments using cadaveric human TBs for validation. These experiments monitored pressure at the ear canal entrance and near the TM, with and without earplugs, during BOP exposure. The TM displacement was measured during acoustic simulation and compared to published results for further validation. This novel 3D printed TB was developed with the aim to provide a standardized testing model for the efficient, cost-effective, and repeatable evaluation of HPDs' performance under blast conditions in hopes to hasten the improvement of HPDs.

3.2 Material and Methods

3.2.1 3D Printed TB Design and Fabrication

The 3D printed TB was designed from an FE model originally developed by Gan et al.[24] using histological cross-sectional images of a 55-year-old human male TB (left ear). The FE and 3D printed TB model consisted of the structural components of the human outer and middle ear including the ear canal, TM, ossicular chain, middle ear suspensory ligaments/muscle tendons, and middle ear cavity (Figure 3-1a). The FE model was imported into SolidWorks (3DS, Waltham, MA) to optimize the human ear model for 3D printing, and as seen in Figure 3-1b, a sectional view of the CAD model of 3D printed TB shows how the human ear model was encased in the outer TB structure. An assembled CAD model of the 3D printed TB is shown in Figure 3-1c-e. The outer ear portion contained most of the ear canal and was designed to attach to the "head block" used in blast exposure tests as described by Gan et al.[26] (Figure 3-1c), and the middle ear portion contained the TM, ossicular chain with joints and suspensory ligaments, as well

as ports for measuring air pressure near the TM (P1) and in the middle ear cavity (P2) and allowing access to the stapes footplate (Figure 3-1d). The 3D printed TB was printed as two main sections: outer and middle ear (Figure 3-1e) The cavity seals (Figure 3-1d and Figure 3-1e) were initially printed separately from the middle ear portion to facilitate removal of support material within the middle ear cavity then fastened to the middle ear portion to enclose the middle ear cavity. The access port to the stapes footplate was sealed to create an enclosed air cavity for a cochlear load. Future studies will use water pressure to simulate the cochlear load.

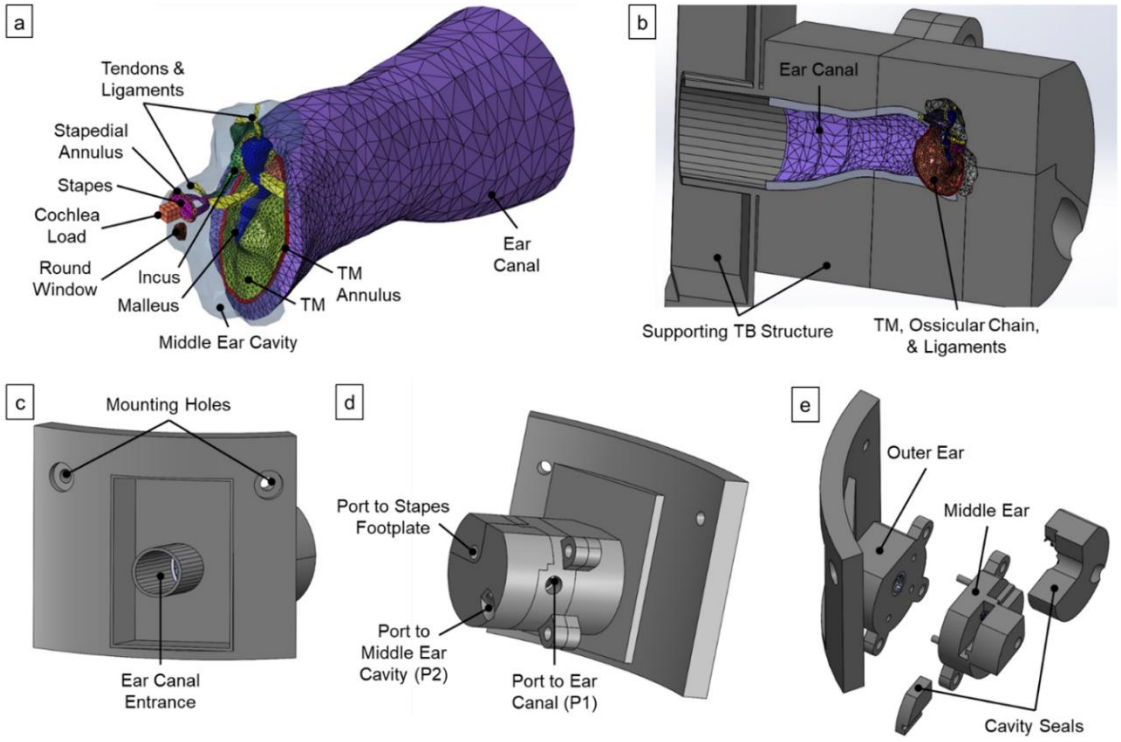

Figure 3-1. (a) FE model of the human ear with the ear canal, middle ear, and cochlear load. (b) Sectional view of the assembled CAD model showing the enclosed ear canal and middle ear tissues. (c) Lateral view of the CAD model of the 3D printed TB highlighting the ear canal entrance. The model's shape was designed to mount into the head block for blast exposure tests. (d) Medial view of the CAD model of the 3D printed TB. The pressure ports to the ear canal near the TM (P1) and middle ear cavity (P2) are shown where pressure sensors are threaded for measurements. A port for access to the stapes footplate for future studies is also shown. (e) Exploded view of the 3D printed TB's CAD model showing the parts to be printed separately: the outer ear, middle ear, and cavity seals.

The model was printed using an Objet350 Connex3 3D printer (Stratasys, Eden Prairie, MN), which has the capability to print materials with varying mechanical properties by mixing multiple proprietary, acrylic-based, UV-cured polymers. Mixing rigid and flexible materials (VeroWhitePlus and TangoBlackPlus, respectively) during printing allowed the 3D printed TB parts to be printed with different flexibility or rigidity per part. Flexible polymer mixtures were used to print the ear's soft tissues (TM, ligaments, tendons, and canal skin) and rigid material mixtures were used to print the ear's hard tissues (ossicles, manubrium, and TB structures). Table 3-1 lists the material properties for the 3D printed TB parts. Materials were chosen by their closeness to their respective part's published mechanical properties. Limited information was available for the 3D printer materials' composition and mechanical properties due to Stratasys' materials being proprietary.[99,100]

Table 3-1. Material properties of the 3D printed materials used for each part in the 3D printed TB.

Structure	**3D Printer Material Properties[a]**		
	Tensile Strength (MPa)	**Elongation at Break (%)**	**Young's Mod. (MPa)**
Tympanic Membrane	1.3 - 1.8	125%	
Skin	3.5 - 5.0	75%	
Manubrium	40 - 60	25%	1700 - 2300
Ossicles & TB	50 - 65	10 - 25%	2000 - 3000
Stapedial Annular Ligament	0.8 - 1.5	170 - 220%	
Other Ligaments	1.3 - 1.8	125%	
Tympanic Annulus	1.3 - 1.8	125%	
Posterior Stapedial Tendon	3.5 - 5.0	75%	
Tensor Tympani Tendon	1.9 - 3.0	105%	
Incudostapedial Joint	2.5 - 4.0	80%	
Incudomalleolar Joint	8.5-10.0	50%	

Abbreviations: Elong. = Elongation; Mod. = Modulus; TB = Temporal Bone
[a] Materials used in the Objet350 are proprietary and material properties are reported as published by Stratasys Ltd. [99,100]

3.2.2 3D Printed TB and Human Cadaveric TB Blast Exposure Tests

Blast exposure tests in 3D printed TB and human cadaver TB were performed similarly to HPD characterizations performed by Gan et al.[26]. The TBs were packed in dry ice and shipped from Science Care, Inc., a certified human tissue supplier for military health research. The study protocol was approved by the Office of Research Protections, US Army Medical Research and Material Command. The 3D printed TB or human cadaveric TBs were exposed to BOPs in an anechoic chamber while fixed to the "head block" under a blast apparatus designed for open-field blasts (Figure 3-2a and Figure 3-2b). Exploding a polycarbonate film (McMaster-Carr, Atlanta, GA) with nitrogen gas at the blast aperture (Figure 3-2a) produced BOPs in the range of 6 – 8 psi. Figure 3-2c illustrates where pressures were monitored: P0, at the entrance of the ear canal, and P1, in the ear canal near the TM. P0 pressure sensor (Model 102B16, PCB Piezotronics, Depew, NY) was mounted 1 cm lateral to the entrance of the ear canal (Figure 3-2a), and the P1 pressure sensor (Model 105C002, PCB Piezotronics, Depew, NY) was either surgically implanted (human TB) or screwed (3D printed TB) into an opening near the TM.

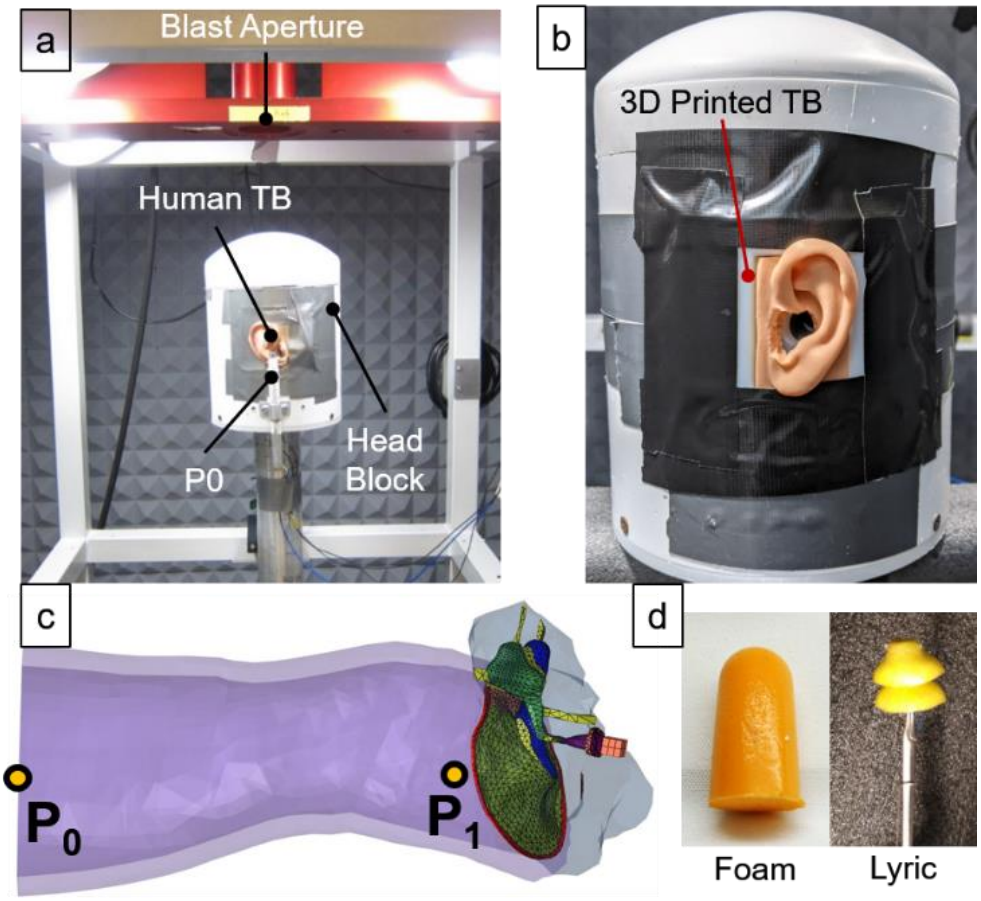

Figure 3-2. (a) Image of the blast test setup within an anechoic chamber where the "head block" sits below the blast aperture. A human cadaveric TB is mounted to the head block and the pressure sensor P0 is mounted outside of the ear canal entrance. (b) Image of the 3D printed TB mounted to the head block. (c) The FE model highlighting where the pressures were monitored during blast exposure: at the entrance of the ear canal, P0, and in the ear canal near the TM, P1. (d) Images of the foam earplug (left) and Lyric earplug with a stick holder (right) used in blast exposure tests.

The pressure in the middle ear cavity (P2) was not monitored in this study for the human TB nor the 3D printed TB as it was in Gan et al.[26]. Pressure sensor readings were recorded and synchronized with a cDAQ 7194, A/D converter 9215 data acquisition system (National Instruments Inc., Austin, TX) using LabVIEW Signal Express software (National Instruments Inc., Austin, TX).

Blast tests were performed with and without earplugs inserted into the ear canal of the TBs. Either a 3M foam earplug (3M Co., St. Paul, MN) or Lyric hearing aid (Phonak,

LLC, Warrenville, IL) was used as HPDs during BOP exposure (Figure 3-2d left and Figure 3-2d right, respectively). The Lyric hearing aid (or earplug) is a deep insertion, passive hearing aid that is installed 4 mm away from the TM and has the potential to offer protection against BOPs.[9,26] This was installed without the battery in both the human and 3D printed TBs.

3.2.3 3D Printed TB Validation and HPDs Evaluation

To validate the functional capability of the 3D printed TB for sound transmission through the ear, the movement of the TM was measured using laser Doppler vibrometry (LDV) under acoustic stimulation, and the data were compared with published human TM's displacement in the literature.[30] The LDV measurements performed in this study were similar to those performed by Gan et al.[31]; however, only the TM velocity was recorded. Sound was delivered in the ear canal near the TM from a speaker (Model MF1, TDT, Alachua, FL) through a 1 mm ID tube which was controlled by a dynamic signal analyzer (HP 35670A, Palo Alto, CA) and a power amplifier (B&K 2718, Norcross, GA). The system's output sound pressure level was monitored with a probe-tipped microphone (Etymotic Research ER-7C, Elk Grove Village, IL) 2 mm away from the TM which allowed the system to generate and maintain a pure tone of 90 dB SPL from 200 – 10,000 Hz. The TM movement was measured by the LDV (Polytec CLV 2534, Irvine, CA) with the laser focusing on a piece of reflective tape attached to the TM's umbo and recorded by the dynamic signal analyzer.

Comparison between P1 pressure waveforms from the human and 3D printed TBs were used as validation for the model as an effective HPD test standard. Measures used to compare P1's intensity and waveform were the peak pressure level, P1:P0 peak pressure

ratio, and A-duration (the measure of time the positive portion of the peak pressure is sustained). In addition, BOP attenuation by the earplugs was examined and compared between the 3D printed and human TBs. The percent error among recorded data was used to evaluate the accuracy of the 3D printed TB model to the human TB. The human TB blast test data used for comparisons were previously published in Gan et al.[26] where blast tests were performed on 13 TBs with foam earplugs (age 74.5 ± 7.6) and six TBs with Lyric earplugs (age 79.7 ± 5.2).

3.3 Results

A finished print of the 3D printed TB's unassembled middle ear can be seen in Figure 3-3a-d where rigid materials were printed in either white or yellow (hard tissues) and flexible materials were printed in shades of gray or black (soft tissues). The lateral surface of the TM can be seen through the ear canal in Figure 3-3a while Figure 3-3b shows the medial-inferior side of the TM within the middle ear cavity. The ossicular chain was freely suspended after the removal of the support material. The top and back seals (Figure 3-3c) were affixed to the middle ear portion to form the middle ear cavity. For clarity, the TM, ossicular chain and their attached ligaments and tendons were 3D printed separately and are shown in Figure 3-3d. The ossicular chain was printed at a 1:1 scale from the human ear or FE model and retained its shape throughout the 3D printed TB's fabrication. Figure 3-3e and Figure 3-3f show the fully assembled 3D printed TB. The model was designed to mount in our current head block with pre-printed mounting holes and allow space to adhere a silicone pinna (Figure 3-3e). Figure 3-3e demonstrates how the Lyric earplug would be fitted into the ear canal. A medial view of the 3D printed TB can be seen in Figure 3-3f where ports to the ear canal (P1), middle ear cavity (P2),

and stapes footplate are highlighted. The ports for P1 and P2 were printed to the recommended specifications of the pressure sensors used in blast exposure tests to ensure a secure fit (Figure 3-3f). The port to the stapes footplate was designed to allow the application of a cochlear pressure to the stapes footplate in future applications, and as with the P2 port, it was not used in the present study.

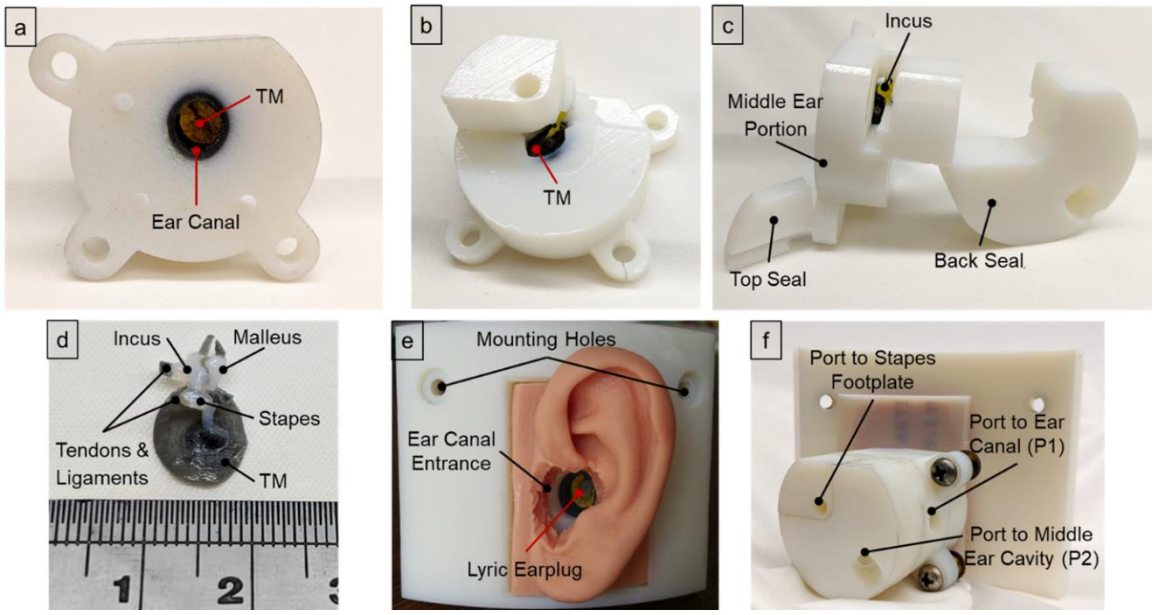

Figure 3-3. Images of a finished print of the 3D printed TB's unassembled middle ear portion. (a) Lateral view of the middle ear portion showing the ear canal and TM within. (b) Medial view of the middle ear portion of the 3D printed TB showing the opening used for cleaning. (c) Posterior view of the 3D printed TB's middle portion with the seals. (d) A 3D print of the ossicles, TM, and ligaments, and tendons from within the middle ear cavity of the 3D printed TB. The ossicles were imaged without the surrounding material and with a scale to highlight the detail and size of the middle ear tissues. (e) Lateral view of the assembled 3D printed TB with a Lyric earplug inserted into the ear canal. A silicone mold of the pinna was adhered to the 3D printed TB to simulate the outer ear. (f) Medial view of the assembled 3D printed TB showing the ports to measure the pressures at the TM and in the middle ear cavity and to access the stapes footplate.

Figure 3-4 displays the peak-to-peak displacement of the 3D printed TB's TM and compares it to data published by Gan and Wang.[30] The published data was recorded using LDV measurements in seven human cadaveric TBs with no observable TM damage, and their results and average are shown in Figure 3-4. While the displacement of the 3D

printed TM follows a similar trend as the human TM, the peak-to-peak displacement of the 3D printed TM was substantially lower than the human's at frequencies lower than 3 kHz. The greatest discrepancy between the human TB average and 3D printed TM occurred at 275 Hz with a difference of 0.058 μm (72.5% error, 0.080 and 0.022 μm for Gan and Wang[30] average and 3D printed TM, respectively), and the closest values occurred at 5,248 Hz with a difference of 0.003 μm (41.1% error, 0.007 and 0.004 μm for Gan and Wang[30] average and 3D printed TM, respectively). It is important to note that the 3D printed TB was initially designed to test HPDs' effectiveness in protecting the ear during BOP exposure and was not designed for acoustic SPL experiments, but future iterations of the model will aim to include acoustic tests.

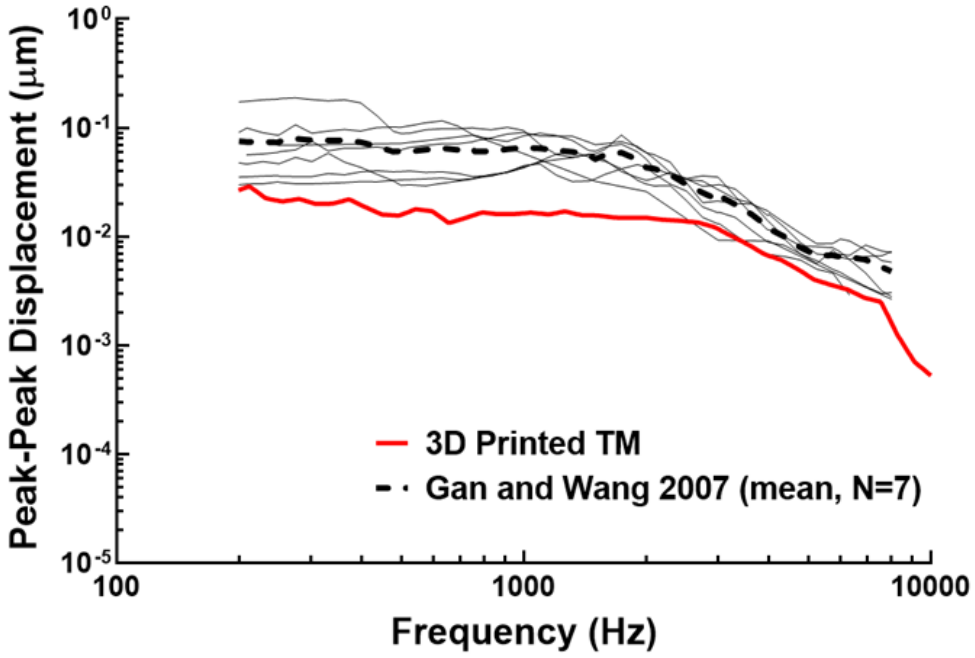

Figure 3-4. Plot of the peak-to-peak displacement of the TM over the frequency range of 200 – 10,000 Hz for the 3D printed TB's TM (red line) and seven human TB samples (solid black lines) from Gan and Wang [30]. The average of the seven samples is plotted in the black dotted line.

The pressures measured during BOP exposure without an HPD for the 3D printed TB and human TB are shown in Figure 3-5a. Specifically, the plot compares the pressures recorded at P0 (entrance of the ear canal) and P1 (in the ear canal near TM) for the printed TB and a human. The peak P0 pressure values were 5.89 psi (186 dB) and 5.92 psi (186 dB) for the human TB and 3D printed TB, respectively, and the A-duration of the P0 waveforms for the human TB and 3D printed TB were 0.32 ms and 0.28 ms, respectively. The P0 waveforms for both test TBs in Figure 3-5a exhibited very similar magnitudes and shapes. The resulting P1 pressure waveforms had peak values of 10.38 psi (191 dB) and 9.79 psi (191 dB) (5.7% error) which occurred at 0.79 ms and 0.69 ms (12.7% error) for the human TB and 3D printed TB, respectively. The A-duration of the P1 waveforms were 0.05 ms and 0.08 ms for the human TB and 3D printed TB, respectively, with a small difference of 0.03 ms. While the P1 peak pressures and A-durations were similar, the time-of-arrival for the P1 peak was sooner for the 3D printed TB than with the human TB (Figure 3-5a). This was likely due to the 3D printed TB having a shorter ear canal than the compared human TB sample and the delay of air velocity and pressure from BOP with increased distance.[15] In addition, the time-of-arrival difference shown in Figure 3-5a was within the variance reported in previous publications testing HPDs during BOP exposure.[26] The P1:P0 ratio was 1.76 for the human TB sample and 1.65 for the 3D printed TB with a relatively low percent error of 6.19%, and according to an HPD characterization study by Gan et al.[26], the P1:P0 ratio of the 3D printed TB was well within the standard deviation reported (typically a mean and standard deviation of 1.7 ± 0.4).

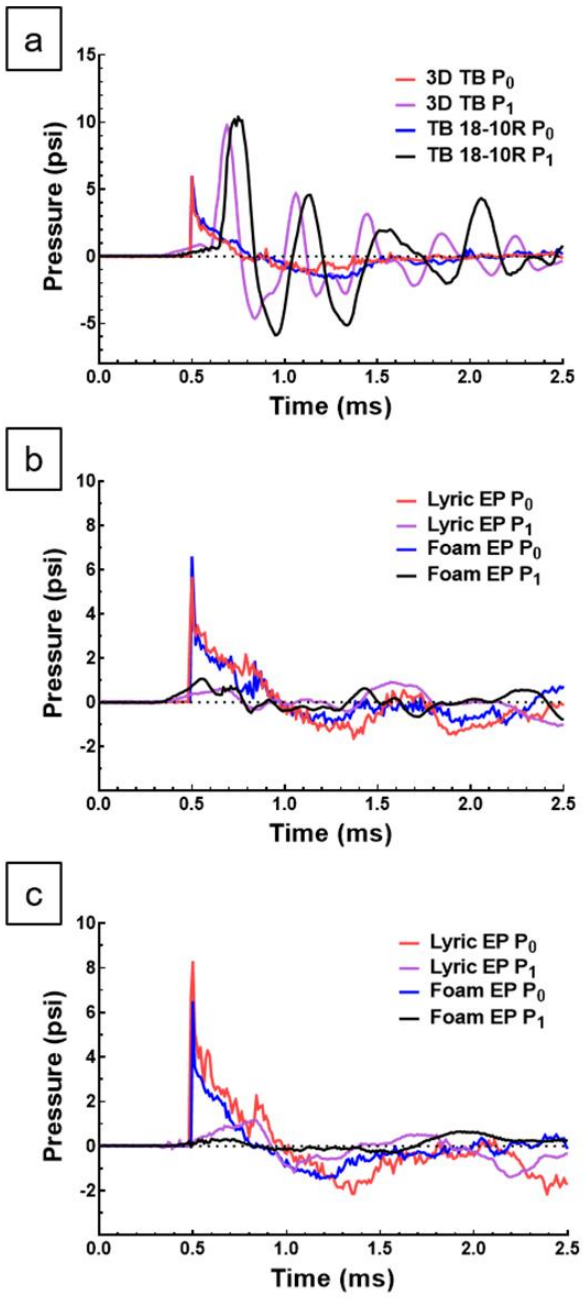

Figure 3-5. (a) Plot of the P0 (ear canal entrance) and P1 (in the ear canal near the TM) pressures measured in blast tests of the 3D printed TB (red line for P0 and purple line for P1) and a human cadaveric TB (blue line for P0 and black line for P1) without hearing protection. (b) and (c) are plots of the P0 and P1 pressures measured in blast tests of the 3D printed TB (b) and human cadaveric TBs (c) protected with a foam earplug (blue line for P0 and black line for P1) or Lyric earplug (red line for P0 and purple line for P1).

Figure 3-5b and Figure 3-5c report the measured pressures during BOP exposure for the human and 3D printed TBs with earplugs equipped. The P0 and P1 pressures

recorded while the 3D printed TB had either the foam or Lyric earplug inserted into the ear canal can be seen in Figure 3-5b, and Figure 3-5c plots the similar data for that in a human TB sample. For the 3D printed TB, the peak pressures were 6.54 psi (187 dB) and 1.06 psi (171 dB) for the foam earplug (blue and black lines) and 5.62 psi (186 dB) and 0.92 psi (170 dB) for the Lyric earplug (red and green lines) at P0 and P1, respectively. The P1 peak times occurred at 0.55 ms and 1.57 ms for the foam and Lyric earplugs, respectively. As for the human TB, the peak pressures were 6.43 psi and 0.65 psi for the foam earplug and 8.24 psi (189 dB) and 1.18 psi (172 dB) for the Lyric earplug at P0 and P1, respectively (Figure 3-5c). The P1 peak times occurred at 1.93 ms with the foam earplug and 0.83 ms with the Lyric earplug. Qualitative observation of the results initially revealed that HPDs in the 3D printed TB attenuated blast pressures similar to that in human TBs; however, P1 peak pressure and time differences between the 3D printed and human TBs were 20% greater for all values. Earplug fit and ear canal variation may account for much of the difference between the human and 3D printed TBs. An ear canal designed to better fit standard sized earplugs can be considered for future model iterations.

Despite discrepancies in the measurements at P1, the 3D printed TB's ability to evaluate HPDs' protective function was within the desired operating range. For the foam earplug, the drop in pressure from the entrance of the ear canal to the TM (P0 – P1, in decibels) was 19.9 dB in the human TB and 15.8 dB in the 3D printed TB (20.7% error), and while that was a difference of 4.1 dB, the decibel loss for tests performed in the 3D printed TB was within the standard deviation for tests performed in human cadaveric TBs with the same earplugs as reported by Gan et al.[26] (mean and SD of 12.3 ± 6.4 dB for

foam earplugs). The P0 – P1 for the Lyric earplug in the human TB was 16.9 dB and 15.7 dB in the 3D printed TB with the same earplug (7.0% error). The difference in pressure level drop across the Lyric earplug between the two TBs was also within the standard deviation reported by Gan et al.[26] (mean and SD of 16.3 ± 1.7 dB the Lyric earplug), and it is important to note that the Lyric earplug was fitted in both the human and 3D printed TB by an experienced audiologist from Phonak to ensure a correct fit which may account for the decreased variance among samples. Table 3-2 summarizes pressure measurements previously mentioned (in decibels) for Figure 3-5.

Table 3-2. Summary of the pressure intensities measured during blast exposure tests.

TB Model	P0 (dB) w/out EP	P1 (dB) w/out EP	P1:P0 ratio w/out EP	P0 w/EP (dB)		P1 w/EP (dB)		P0 - P1 w/EP (dB)	
				Foam	Lyric	Foam	Lyric	Foam	Lyric
3D Printed	186.2	190.6	1.65	187.1	185.7	171.3	170.0	15.8	15.7
Human	186.2	191.1	1.76	186.9	189.1	167.0	172.2	19.9	16.9

Abbreviations: EP = Earplug, Foam = Foam Earplug, Lyric = Lyric Earplug, TB = Temporal Bone

3.4 Discussion

3.4.1 Application of 3D Printed TB for Evaluation of HPDs

The use of a standardized blast test model for assessing the protective function of HPD designs should greatly assist in HPD development by offering an efficient, accurate, and cost-effective model. Improved HPDs would undoubtedly reduce the occurrence of hearing loss among veterans.[18] Previous publications have reported studies that thoroughly test various HPDs at the sound pressure level of military firearms[68,69] (about 130 – 170 dB), but few studies investigated the effectiveness of HPD in blast pressures above 180 dB.[9,26,105] Gan et al.'s[26] study published the most comparable results to the tests performed with the 3D printed TB with blast exposures performed at levels above

185 dB. The P1 pressures measured in the 3D printed TB were similar to that observed by Gan et al.[26], and as previously mentioned, many of the metrics measured with the 3D printed TB followed the same trend and were well within the standard deviations reported by Gan et al.[26]. In addition, the P1 reduction (P1 with an earplug subtracted from P1 without an earplug) of the foam and Lyric earplugs in the 3D printed TB were 19.3 dB and 20.5 dB, respectively, which were within the reported standard deviations (17.3 ± 6.8 dB and 20.9 ± 5.3 dB for the foam and Lyric earplugs, respectively[26]). Brungart et al.[9] did report an impulse peak insertion loss (i.e. P0 – P1) of 30 – 34 dB at blast pressures from 150 – 190 dB using a Lyric extended wear hearing aid. The greater than 10 dB difference in attenuation may be due to the use of an ATF, and the authors mentioned that the Lyric hearing aid needed to be placed against the ATF's microphone (i.e., eardrum) due to the short length of its ear canal. Since the 3D print TB's ear canal was anatomically correct, the Lyric hearing aid was inserted at the correct length. The 3D printed TB, with HPD attenuation function measurements similar to literature,[9,26,105] demonstrated that this developed model may function as an accurate standardized model for efficiently evaluating HPDs' performance.

ATFs have been used as a model for evaluating high-pressure transmission in the ear, and high-pressure ATFs do exist that withstand pressures as high as 193 dB,[68,105] however, the test fixture alone would cost above $1,000. Such a high equipment cost would be prohibitive for many researchers who desire to test HPD designs in a blast environment not to mention risking damage to the expensive ATF during tests. Our 3D printed TB provides an effective blast test model for evaluating HPDs where if a researcher has access to a similar 3D printing system, a researcher may obtain our model

for less than $100 of printing material. A low-cost, accurate test fixture like the 3D printed TB presented here would make blast exposure tests available to more HPD developers increasing their beneficial impact on the prevention of blast-related ear injuries.

3.4.2 Limitations and Future Work

The middle ear tissues attached to the ossicular chain are viscoelastic in which their response to stimuli is heavily dependent on time or strain rate. This is a limitation of the current 3D printed TB model as the materials used to print the TB exhibited an elastic behavior. The difference in LDV displacement measurements between the 3D printed TM and published human TM should be due to the lack of viscoelastic behavior of the 3D printed TM and middle ear. While this was not the primary goal of this study, a 3D printed TB that can model the mechanical response of the ear from blast and acoustic stimuli would be greatly beneficial to the development of HPDs. Refinement of the acoustic response of the 3D printed TB's middle ear is planned for future iterations of our model, which include mass-balancing middle ear tissues and exploring alternative materials for the model.

Moreover, discrepancies between the LDV data from the 3D printed TB and human TB (Figure 3-4) indicated that the transfer function of the middle ear in 3D printed TB needs to improve.[31] To address the mass-damping balance of the 3D printed TB's middle ear, the addition of a cochlear load (along with material improvement) will further improve the acoustic response of our 3D printed TB. As shown in Figure 3-1d and Figure 3-5b, the design of the 3D printed TB considered this as a way to provide the fluid pressure feedback from the cochlea during ossicular movement. Once the middle ear

transfer function of the 3D printed TB is improved, LDV measurements of the TM and ossicular chain are planned to further validate our model, and with the versatility of 3D printing, measuring the velocity of the incus and stapes footplate can be facilitated by incorporating windows for the vibrometer to simply measure the ossicles.

3.5 Conclusion

In summary, a 3D printed TB was created for the purpose of providing standardized testing of HPDs to blast exposure. Two HPDs (a standard foam earplug and Lyric hearing aid) were included for testing the protective function with the 3D printed TB during blast. The attenuated peak pressure near the TM was as low as 0.92 psi (170 dB) with a blast peak pressure of 5.62 psi (186 dB) at the entrance of the ear canal with an HPD in use, and without an HPD, the pressure near the TM was 9.79 psi (191 dB) with a similar blast peak at the entrance of the ear canal. Results show that the pressure measurements in the 3D printed TB were well within the mean and standard deviation of the published data from tests performed in human cadaveric TBs demonstrating that our 3D printed TB is a valid model for testing HPD designs. The 3D printed TB developed in this study provides an accurate and cost-effective evaluation tool for HPDs' protective function against BOP exposure. The printed ear model has the potential to perform as a human temporal bone model for research in ear biomechanics for acoustic transmission and the development of middle ear implants.

Chapter 4 Assessing the Effect of Liraglutide on the Blast Damages Sustained in the Chinchilla Cochlea with Scanning Electron Microscopy

4.1 Introduction

The inner ear, or cochlea, has long been the subject of research for investigating sensorineural hearing loss (SNHL) occurring after noise exposure damages the inner ear.[50,57,80] Furthermore, noise exposure has been shown to damage the synaptic connections and neuron synapses within the cochlea, also known as synaptopathy, while leaving their respective hair cells intact.[49,57] Despite the correlation between noise and inner ear damage becoming more clear, research into how blast affects the inner ear is still relatively new.[11,18,39,70,102] Previous studies in BOP exposure to the ear suggested that blasts can damage the cochlea hair cells,[39,70] the spiral ganglion and their synaptic connections,[39] and even cause damage to the central auditory system.[23,61,82] Since the extreme pressures from blasts can affect both the peripheral and central auditory systems (PAS and CAS, respectively) and cause overlapping symptoms, more work is needed to assess the specific damage mechanisms occurring within the cochlea.

Therapeutics to mitigate long-term hearing loss after blast exposure are needed and sought after since many deployed service members of the military are at high risk for blast exposure and hearing loss is commonly developed in those who are exposed.[18] A long-lasting glucagon-like peptide-1 receptor (GLP-1R) agonist, liraglutide, binds to the GLP-1 receptor of neurons which results in an increase in protein kinase A and B which in turn activates transcription factor cAMP-responsive element-binding protein (CREB)

and promotes cell proliferation. Furthermore, the activation of the GLP-1R pathway protects the cell by downregulating the blast-induced oxidative stress that can lead to apoptosis. Liraglutide was shown in studies to exhibit these potential protective effects in neuronal tissue by ameliorating neurodegeneration induced by Parkinson's and mild traumatic brain injury (TBI).[103] Clinical research on military personnel has shown a strong correlation between TBI and sensorineural hearing loss, and the auditory cortex neuron and spiral ganglion loss from blast-induced damaged shared similar mechanisms with memory loss induced by TBI.[72,104] This strongly suggests that liraglutide can also protect the neurons of the auditory system after blast exposure as well. While there is potential for protecting the neuronal tissue of the auditory system, the effect of liraglutide has on the cochlea after blast exposure is unknown, and since the health of the spiral ganglion and hair cells are closely related,[39,57] the blast-induced cochlear damage needs to be assessed to fully understand liraglutide's effect on the inner ear post-blast exposure.

Scanning electron microscopy (SEM) has been used as a tool for analyzing hair cells and their stereocilia.[42,43,70,75,106] The high resolution and excellent topographical detail provided by SEM allowed researchers to easily visualize subtle physical damages to the stereocilia of OHC caused by blast or noise exposure and even observe the tip links between the stereocilia.[33,43,70] Through SEM studies, it was observed that the stereocilia could recover their shape and tip links as soon as four days after noise exposure to levels that cause temporary hearing loss (110 dB for 30 minutes), as well as the progressive decay of stereocilia and the loss of hair cells exposed to noise at permanent hearing loss levels (120 dB for 150 minutes).[33] The blast-induced disruption of the stereocilia was also observed using SEM.[70] Since the scarring of the organ of Corti after hair cell loss and the

damage to the stereocilia can effectively be observed with SEM, SEM is a valuable tool for observing the blast-induced effects on the organ of Corti and if liraglutide significantly protects against hair cell loss in the cochlea.

The reported study aimed to utilize SEM to assess the blast-induced hair cell damage in chinchillas exposed to blast and the potential therapeutic effect of liraglutide on hair cell viability. Chinchillas were exposed to six consecutive blasts at levels ranging from 21-35 kPa (3-5 psi or 180-185 dB SPL). Auditory brainstem response (ABR) was measured on Day 1 (before and after blast) and on Days 4, 7, and 14 to characterize the progression of the hearing damage. A seven-day-long liraglutide treatment was started two days before blast exposures, and the results measured from hearing function tests and SEM analysis were performed to investigate the therapeutic function of the liraglutide for protecting the cochlea and its outer hair cells (OHCs).

4.2 Materials and Methods

4.2.1 Animal Protocol for Drug Administration and Blast Exposure

Young, chinchillas (Chinchilla laniger) with mixed-gender provided by Ryerson Chinchilla Ranch (Plymouth, OH) were included in this study. The study protocol was approved by the Institutional Animal Care and Use Committee of the University of Oklahoma following the guidelines of the National Institutes of Health and the US Department of Agriculture. All animals went through health exams to ensure they are healthy at the beginning of the experiment.

Nineteen chinchillas were randomly separated into three groups: blank control, pre-blast drug treatment, and blast control (N = 5, 8, and 6, respectively). Figure 4-1 shows the time course and experimental procedures for the pre-treatment drug group.

Key procedures such as blast exposure, hearing function tests, and euthanasia are emphasized by arrows. Animals in the pre-blast treatment group were subcutaneously injected daily with liraglutide (Victoza, Novo Nordisk Inc. Plainsboro, NJ) two days before the blast exposure and every day thereafter for seven consecutive days. The blast control chinchillas underwent blast exposure procedure only without the liraglutide treatment. The dose of liraglutide was 246.7μg/kg/day, which was equivalent to the human dose (20μg/kg/day) normalized to body surface area across species and considered respective to the dosage used for published mice and rats studies.[37,56] The hearing function tests were performed before and after the blast on Day 1 and Days 4, 7, and 14. Upon the completion of the Day 14 hearing function test, some of the chinchillas from the blast control and pre-blast treatment groups were euthanized to harvest the cochleae for SEM imaging, and the remaining chinchillas were euthanized after the Day 28 hearing function test where the cochleae were harvested for SEM imaging.

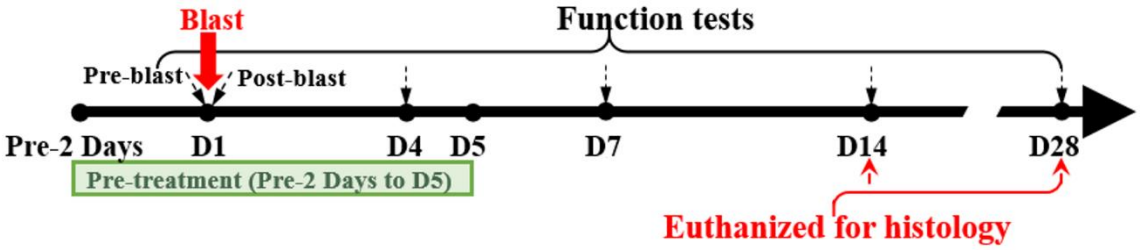

Figure 4-1. Schematic diagram of the time course and experimental procedure for the pre-blast treatment group.

For the blast procedure, the animals were anesthetized with an intramuscular injection of 35 mg/kg Ketamine (Henry Schein Animal Health, Dublin, OH) and 3 mg/kg Xylazine (Akorn Inc., Lake Forest, IL) to ensure the chinchilla was sedated during blast exposures. The experimental blast setup used for this study was previously reported by Smith et al.[95] In short, the chinchilla was placed in a specifically designed L-shape animal

holder and fixed with straps to position the top of its head facing the center of the blast source (Figure 4-2). The nose of the chinchilla pointed forward and the pinna remained unfolded to ensure the ear canal was naturally open during the blast exposures. A pressure sensor (Model 102B16, Piezotronics, Depew, NY) was fixed to the animal holder with the measuring surface next to the chinchilla's ear to monitor the blast pressure at the entrance of the ear canal.

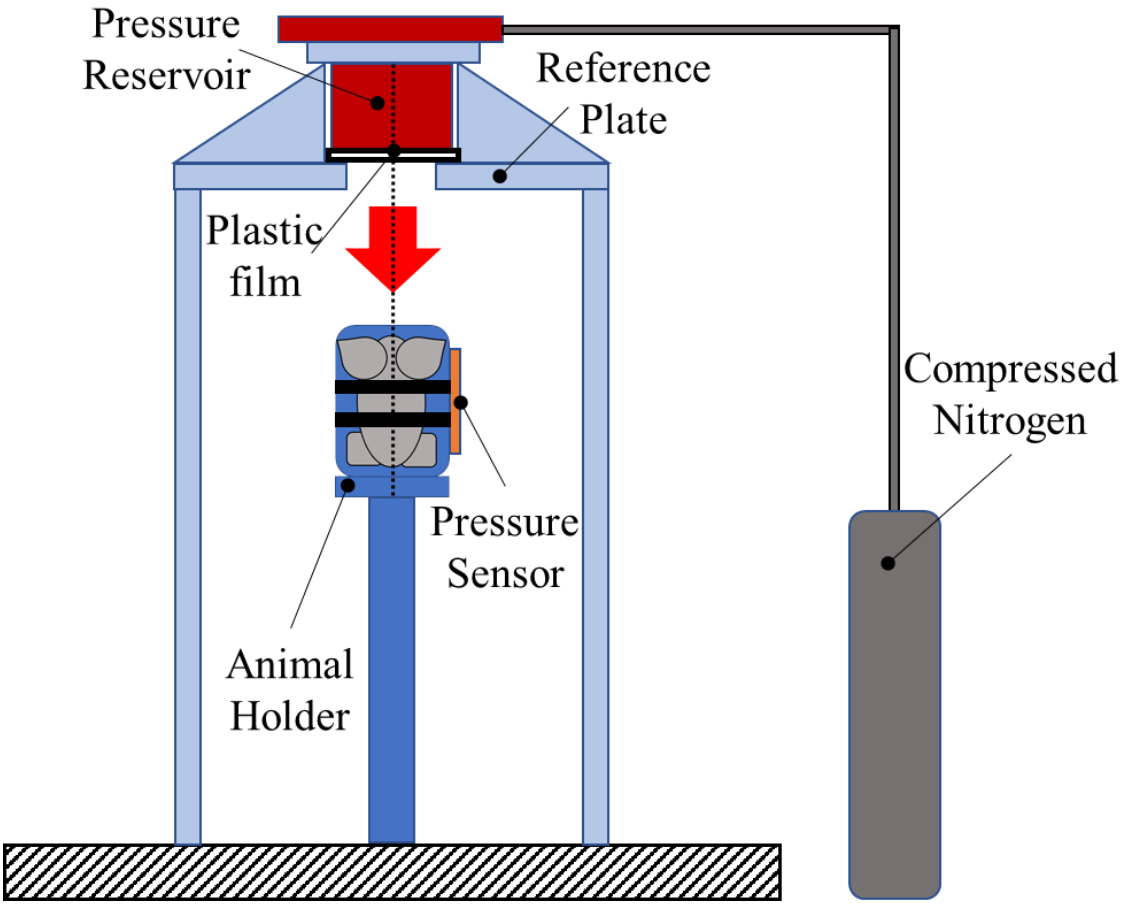

Figure 4-2. Schematic of the animal experimental setup with blast apparatus. The top of the chinchilla's head was facing the blast source and the nose of the chinchilla pointed to the front. Figure from Jiang et al.[46]

A well-controlled compressed nitrogen-driven blast apparatus, located inside an anechoic chamber (Figure 4-2), was used to generate BOPs at peak pressure levels of 21-35 kPa (3-5 psi) using polycarbonate films of thickness 0.25 mm (McMaster-Carr,

Atlanta, GA). The chinchilla was exposed to six consecutive blasts at 5-minute intervals. The pressure signals from the sensor were processed by a cDAQ 7194 and A/D converter 9215 (National Instruments Inc., Austin, TX) at a sampling rate of 100k/s (10 ms dwell time) using a LabVIEW software package (National Instruments Inc., Austin, TX) for data acquisition and analysis.

4.2.2 Hearing Function Measurements

The testing for the hearing function was performed on Day 1 pre- and post-blast and Days 4, 7, and 14. For hearing tests performed on Days 4-14, the chinchillas were sedated by isoflurane (Covetrus, Dublin, OH) at a concentration of 1%-3% in the oxygen at a flow rate of 1L/minute. Isoflurane sedation was not used on days with blast exposure due to the inability of the sedation equipment to withstand blast exposure. Before each hearing function measurement, the condition of the ear canal and TM were examined with a 3.9 mm digital otoscope (ScopeAround), and wide-band tympanometry (Titan, Interacoustics, Denmark) measurements were recorded as well to determine TM and ossicular function. Thereafter, ABR measurements were performed on anesthetized animals at the previously specified time intervals.

Following a protocol previously reported by Smith et al.[95], ABR measurements were recorded bilaterally using a TDT system III (Tucker-Davis Technologies, Alachua, FL). While anesthetized, stainless steel needle electrodes were placed subcutaneously at the vertex of the skull and ventrolateral surfaces of the ear, and a ground electrode was placed in the rear leg. Tone burst stimuli of 0.5-ms rise-fall time and 4-ms duration with alternating polarity at frequencies of 1, 2, 4, 6, and 8 kHz were used.[27] The stimuli signals were designed by the SigGenRP and BioSigRP software, created by an RP2.1 signal

processor, attenuated by a PA5 programmable attenuator, amplified by two stages of SA1 stereo power amplifier and power amplifier TYPE 2718 (BRUEL & KJAER, Nærum, Denmark), generated by an MF1 multi-field magnetic speaker, and delivered into the chinchilla ear canal through a 10 cm tube. The sound pressure level in the ear canal was calibrated and monitored by a probe microphone (ER-7C, Etymotic Research, Elk Grove Village, IL). The electrode recordings were pre-amplified and collected by an RA16 Medusa base station at a rate of 25 kHz.

ABR thresholds were determined by visually examining the prominent ABR peaks to determine the lowest sound level at which reproducible waveforms were observed. If an ABR response was not detected at the maximum acoustic stimulation, the threshold was arbitrarily set to be 100 dB. Alternatively, the threshold was arbitrarily set to be 20 dB if the ABR signal continued to appear at 20 dB. The ABR threshold shifts on Days 1, 4, 7, and 14 were calculated by subtracting the threshold measured pre-blast from the threshold measured at the post-blast time points.

4.2.3 SEM Preparation and Imaging

After the hearing function measurements on Days 14 or 28, the chinchilla was anesthetized with ketamine/xylazine, and transcardial perfusion was performed with phosphate buffer saline (PBS) followed by 4% paraformaldehyde. Once the animal was euthanized, the cochlea was immediately harvested, and the round and oval window membranes were removed. The cochlea sample was then fixated in 2% paraformaldehyde (Sigma-Aldrich) and 2.5% glutaraldehyde (Ted Pella, Inc) with 0.1M PBS solution containing 5% sucrose overnight at 4 °C. The samples were then decalcified with 0.5M ethylenediaminetetraacetic acid (Sigma-Aldrich) in PBS for seven days and micro-

dissected for a post-fixation with 1% OsO_4 (Ted Pella, Inc) at 4 °C for 30 min. Samples were then dehydrated in ethanol, critical point dried with CO_2, sputter-coated with gold/palladium, and examined with an electron microscope at the University of Oklahoma Samuel Roberts Noble Microscopy Laboratory (either with the JSM-840 [JEOL Ltd., Tokyo, Japan], TM3000 [Hitachi Ltd, Tokyo, Japan], or NEON [ZEISS, Jena, Germany]). Cochlea samples were imaged at the characteristic frequency regions of the organ of Corti at: 0.5, 1, 4, 6, and 8 kHz (roughly 13, 10.5, 5.5, 4, and 3 mm from the base of the BM, respectively). Note that SEM imaging was not performed for every animal within the groups of this study (n = 5, 4, 4, 3, and 3 for control, Day 14 and 28 pre-blast treatment, and Day 14 and 28 blast control, respectively) due to animal tissues being preserved for other histological studies.

4.2.4 Statistical and Imaging Analyses

The ABR threshold was expressed as the mean ± SEM (standard error) and was plotted in GraphPad Prism (GraphPad Software Inc., Version 9.0). A two-way repeated-measures ANOVA test ($\alpha = 0.05$) was used to check whether the effects of the treatment (pre-blast treatment and blast control) and post-blast recovery time were significant ($p < 0.05$).

OHC counts were performed on the SEM images of the organ of Corti at the 0.5, 1, 4, 6, and 8 kHz frequency positions. OHC bin sizes of 15x3 (maximum of about 45 OHCs) were used for the cell count areas. Note it was possible to have more than 45 OHCs within the counting area due to extra OHCs being present. One-way ANOVA test ($\alpha = 0.05$) was used to test for significance ($p < 0.05$) among the groups per frequency position.

4.3 Results

Figure 4-3 shows representative SEM images from each group at the 0.5, 4, and 8 kHz regions. Missing OHCs in Figure 4-3 can be recognized from the area where the Deiters' cells redistribute to seal the reticular lamina after an OHC dies (black arrows).[55] Notice that the control cochlea samples exhibit a baseline amount of hair cell loss that occurs occasionally along the length of the organ of Corti. SEM imaging did not show a significant increase in hair cell loss when compared to the control SEM imaging analysis. Furthermore, disturbed stereocilia could be observed in some of the images (Figure 4-3J-M for example), but the source of that disruption can be assumed to be from sample preparation since stereocilia have shown to recover from temporary damage within four days or advanced degeneration of the OHC and stereocilia would have set in within this study's observation time.[33]

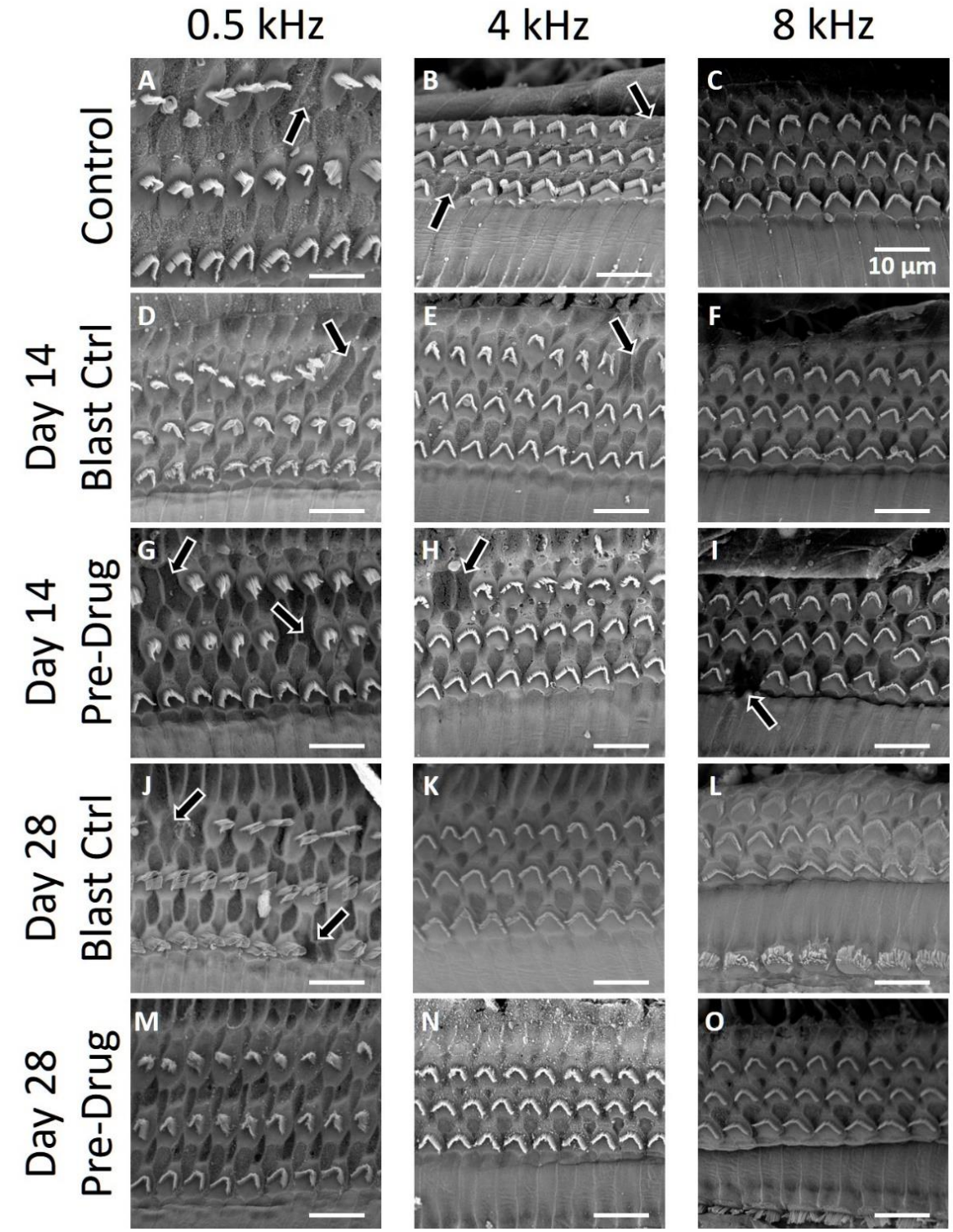

Figure 4-3. (A-O) SEM images of the OHCs of the three animal groups: control (A-C), Day 14 (D-F) and Day 28 (J-L) blast control, and Day 14 (G-I) and Day 28 (M-O) pre-blast treatment. Images from each group are from the 0.5, 4, and 8 kHz frequency region of the BM. Arrows point out missing OHCs and the scale bar represents 10 µm.

Figure 4-4 shows the mean and error bars (standard error) of the OHC counts from the SEM images. Cell counts were performed at BM frequency positions of 0.5, 1, 4, 6, and 8 kHz for each of the animal groups: blank control (n=5), Day 14 (n=4) and Day 28 (n=4) pre-blast treatment, and Day 14 (n=3) and Day 28 (n=3) blast control. Each groups' means were above 40 for every frequency position except for Day 14 pre-blast treatment at 6 kHz. This led to the result that the blast exposure treatment (six consecutive blasts at pressure levels of 21-35 kPa) did not cause a significant loss in OHCs at the imaged frequencies 14 or 28 days after blast exposure, neither could liraglutide's protective effect be observed at those frequencies and time points. Even though the mean for Day 14 pre-blast treatment at 6 kHz was 32.75, the OHC count for this group varied widely causing a standard error of 7.21 (SD of ±14.42) which resulted in no significant difference for this groups mean amongst the other groups. The organ of Corti for some of the Day 14 pre-blast treatment at 6 kHz sample exhibited heavy scarring and missing OHC while other samples within this group did not show any loss of OHCs. As shown by Figure 4-4, many areas of the observed cochleae in the test groups did not show more OHC loss than what was observed in control samples.

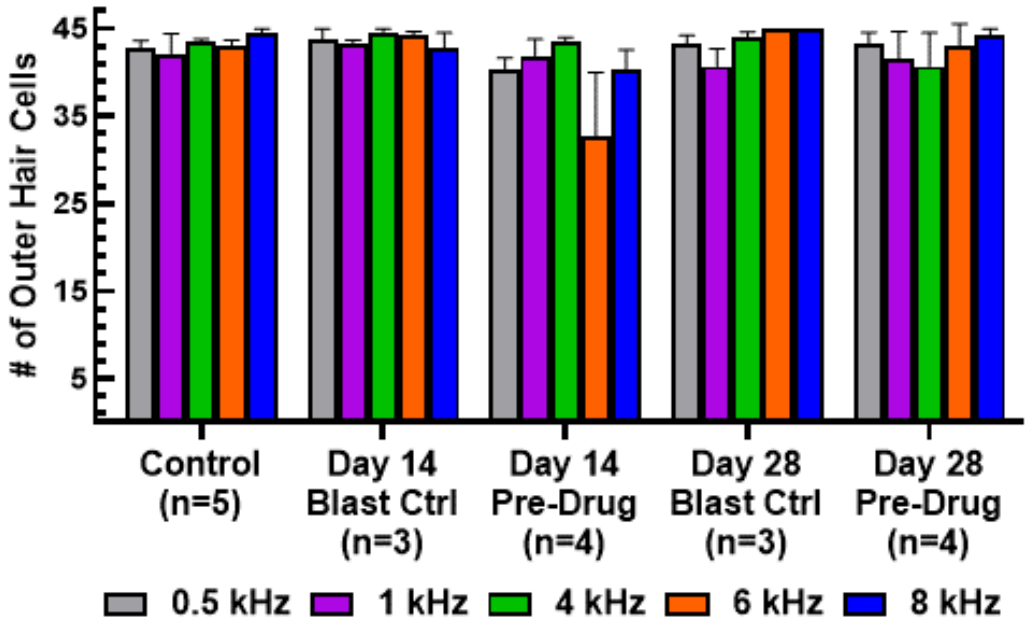

Figure 4-4. Mean and standard error bars of outer hair cell count from SEM images of the three animal groups: control (n=5), Day 14 (n=4) and Day 28 (n=4) pre-blast treatment, and Day 14 (n=3) and Day 28 (n=3) blast control. Cell counts for each group are compared at BM frequency positions of 0.5, 1, 4, 6, and 8 kHz.

Figure 4-5 shows the mean and standard error of the ABR threshold shifts for animals in the pre-blast treatment and blast control groups on Days 1 (post-blast), 4, 7, and 14 (n=14 ears in each group). The mean threshold shifts post-blast ranged between 35 dB to 50 dB for both groups with shifts tending to be lower at 1 kHz and greater at 4 to 8 kHz. The ABR threshold shifts decreased over time from Day 1 to Day 14 and at a decreasing rate with the greatest reduction occurring between Days 1 and 4. As shown in Figure 4-5A, the mean threshold shifts for Day 14 of the drug treatment group ranged from 5 dB at 1 kHz to approximately 25 dB at 6 kHz. The blast-control group results shown in Figure 4-5B showed greater threshold shifts on Day 14 than the liraglutide-treated group with the mean threshold shift value increasing from 15 dB at 1 kHz to 30 dB at 8 kHz. The ABR threshold shift indicated the blast-induced acute damage on Day 1

was approximately at the same level for both groups of chinchillas, and the high-frequency (4-8 kHz) was more severely damaged than the low-frequency hearing (1-2 kHz). The liraglutide treatment facilitated the recovery of the ABR threshold after blasts. The two-way ANOVA analysis at each frequency point indicated the recovery time significantly ($P<0.05$) changed the mean of the ABR threshold shift at all frequencies. The liraglutide treatment introduced a significant change of the ABR threshold shifts at 1, 2, 5, and 8 kHz but not on 4 kHz ($P = 0.69$).

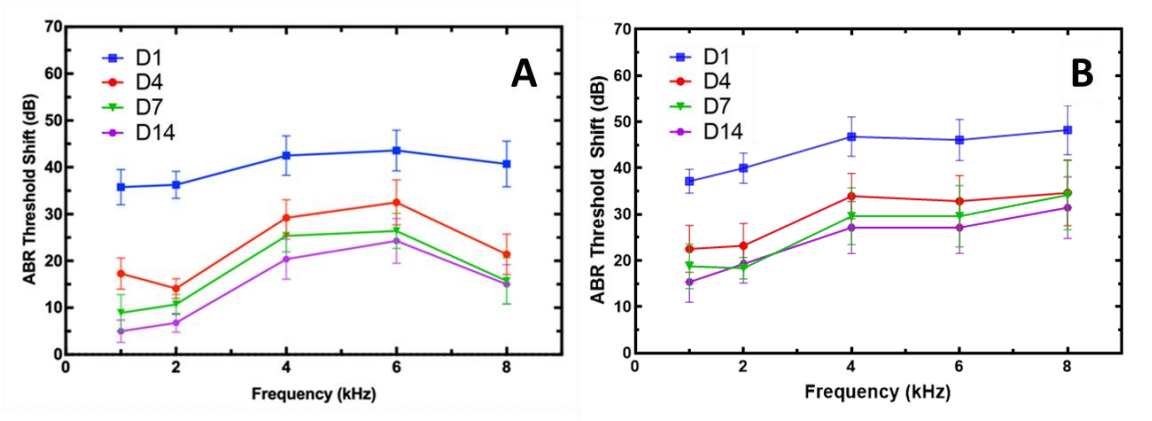

Figure 4-5. ABR threshold shifts (mean ± SEM, n = 14 ears in each group) measured on Days 1, 4, 7, and 14 from (A) pre-blast treatment and (B) blast control groups. Figure from Jiang et al.[46]

For reference, Figure 4-6 shows the ABR threshold hearing function tests on drug and sham control animals. These plots only present the direct threshold readings and not the shift in ABR threshold relating to pre-blast exposure levels. This was due to the shift for each control being too small to meaningfully present. The ABR threshold results show that the liraglutide drug treatment and anesthetization procedures did not alter the ABR threshold of the animals.

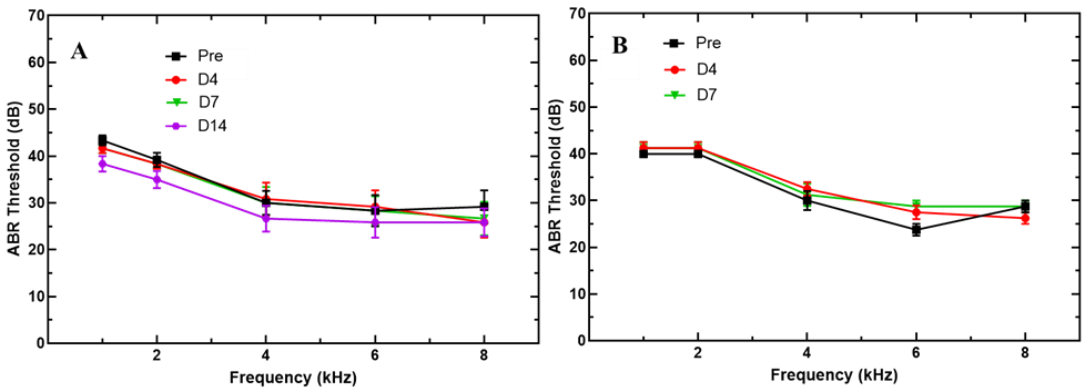

Figure 4-6. The ABR threshold was measured from (A) drug control (mean ± SEM, n = 6 ears) and (B) sham control (mean ± SEM, n = 4 ears) groups. In the drug control group, the measurement was conducted on Days 1(Pre), 4, 7, and 14. In the sham control group, the measurement was only conducted on Days 1(Pre), 4, and 7. Figure from Jiang et al.[46]

4.4 Discussion

4.4.1 Effect of Liraglutide on OHC and Hearing Loss

With blast-induced auditory injury research becoming more relevant, studies investigating the blast damage to the cochlea have increased;[11,39,70,82] however, it is becoming more apparent that blast-induced hearing loss and TBI correlate and affect each other as the field matures.[60,82] While investigating a therapeutic drug for mitigating blast-induced CAS damage, it is necessary to determine the therapy's effect on the cochlea due to the dependent relationship between blast damage and the peripheral and central auditory systems.[60] In this study, the OHC loss along the BM after exposure to six consecutive blasts was investigated along with the liraglutide's effect on that OHC loss. The cochleae were examined at 14 and 28 days after exposure to BOPs ranging from 21-35 kPa (3-5 psi). ABR threshold shifts were also reported to analyze the resulting hearing function and compare them to the SEM images. Interestingly, the widespread permanent threshold shifts observed in Figure 4-5 did not reflect in the SEM imaging analysis (Figure 4-4). The missing OHC counts from the blast groups were not more than what

was seen in the control group. All animal groups had the occasional missing OHCs, but a pattern did not exist that would result in a significant difference among the groups. This result is not surprising, however, as researchers have characterized the loss of hearing where synapses and spiral ganglion are damaged or degenerated but the hair cell remains as synaptopathy.[39,49,57] Liberman et al.[49] reported the degeneration of hair cell's efferent and afferent neurons after noise-induced hearing loss, but their respective hair cells could remain up to two weeks after exposure. Furthermore, damaged areas showed lower synaptic activity at the hair cell showing that the hair cell could recover from temporary hearing loss while the neuron does not.[33,49] A follow-up study showed that similar results were found where chinchillas developed synaptopathy after being exposed to blasts at a level that caused temporary hearing loss.[39] Blast-induced cochlear damage has been shown to affect both the neurons of the cochlea and the hair cells, but at lower BOP levels, such as in this study, the cochlear damage my not obviously damage the hair cells of the cochlea.[39,70]

All the chinchillas of this study experienced TM rupture during the six blast exposures. While the damage to the TM and middle ear was apparent, the rupture of the TM had a protective effect on the inner ear. The pressure the TM experienced during blast exposure was partially relieved when a rupture occurred. Thus, the displacement magnitude of SFP would be reduced, and the TM rupture subsequently lowered the input energy into the cochlea. This could further explain why OHC remained viable even at the base of the cochlea. A similar effect was observed by Hickman et al.[39] The authors observed that hair cell survival was higher for chinchillas when their eardrum ruptured during blast exposure compared to those who did not experience eardrum rupture.[39]

While this gives incite to the high survival rate of OHCs in this study, it does not explain the widespread hearing loss for chinchillas in blast groups. This study is further evidence that blast-induced hearing loss is greatly intertwined with damage to the CAS and auditory nerve, and with the greater recovery in hearing function in drug-treated animals compared to that in untreated animals, liraglutide showed to be a potential therapeutic drug for blast exposure victims.

Variability and sample size was a limitation for this study. Even though some cochleae did have organ of Corti regions that had significant losses in OHCs, this hair cell loss was not consistent even within a group at the same frequency position. Figure 4-7 shows an example of inconsistent OHC loss within an animal test group. The images are of the 4 kHz region of the BM from two samples of Day 28 pre-blast treatment drug group. The image in Figure 4-7A had very few missing OHC while Figure 4-7B exhibited a much higher loss in OHC. With this variance within some sample groups, it would be difficult to accurately determine the effects of blast exposure when compared to controls. The variation among group samples imposes a limitation on this study and demonstrates the need for larger sample sizes per group to overcome that variance in future efforts. Furthermore, SEM analysis of cochleae at different recovery times (i.e., post-blast, 4 and 7 days after blast) would give insight to the progression of OHC loss after blast exposure.

5.1.1 Limitations and Future Work

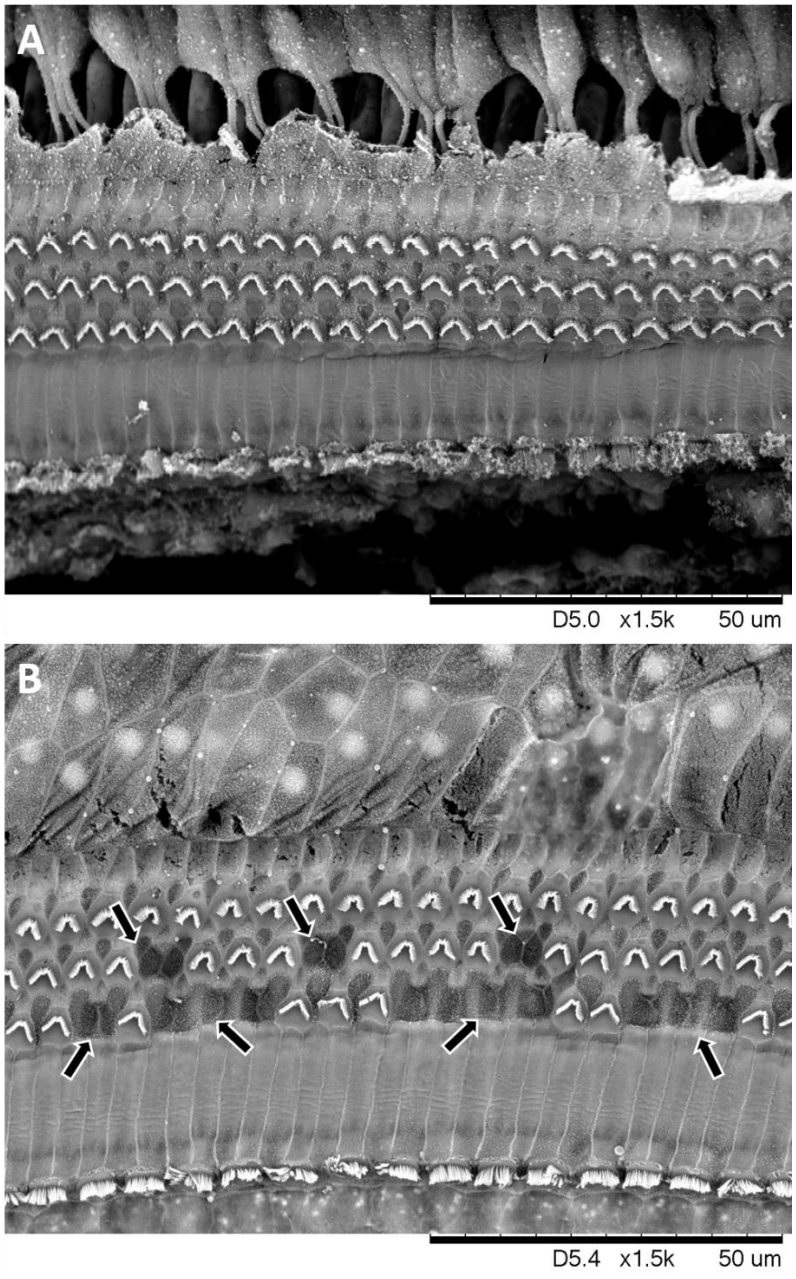

Figure 4-7. SEM images of the 4 kHz frequency position of the organ of Corti for two samples in the Day 28 pre-blast drug treatment group. The left image (A) is an example of an organ of Corti sample with little to no OHC loss, and the right image (B) shows a sample exhibiting significant OHC loss. One increment of the black scale bar is 5 µm. The black arrows point out missing OHCs.

Another improvement for this study would be to include distortion product otoacoustic emission (DPOAE) measurements to observe the active cochlear function.

This noninvasive measurement is essential for determining how blast affects the cochlear tuning ability during sound stimuli (i.e. the function of the OHCs).[87] With the results of this study suggesting that the blast-induced hearing loss was not caused by extensive OHC loss, Histological studies on spiral ganglion neurons, hair cell vesicle activity, ribbon synapses, middle genicular body, and auditory cortex could provide extensive evidence for the ties between auditory injury and TBI and discover how liraglutide improved hearing recovery after blast. Our future studies will seek to include these tests along with obtaining DPOAE measurements permitting good TM conditions.

Conclusions

This study aimed to investigate the viability of OHCs of chinchillas that were exposed to six consecutive blast exposures ranging from 21-35 kPa (3-5 psi) and if liraglutide had a significant effect on OHC survival after blast exposure. Results showed that OHC loss was not significantly greater than controls for blast-exposed chinchillas with or without the drug treatment despite some blast-exposed cochleae showing some OHC loss. Conversely, the ABR results showed blast-exposed chinchillas suffered hearing function loss throughout the frequency range of 1-8 kHz. Furthermore, the chinchillas treated with liraglutide did significantly recover more hearing function than chinchillas without the drug treatment. With the results showing increased ABR thresholds but little loss in OHCs, BOPs at the tested pressure levels appear to damage the CAS and neurons of the PAS, and liraglutide has shown to have the potential to protect the auditory system's neuronal tissue while having no adverse effect on OHC survivability. This study increases our understanding of the link between TBI and hearing loss while also supporting the use of liraglutide as a therapeutic for blast victims.

Chapter 5 Summary and Future Work

With the damage mechanisms in the cochlea that occur during blast largely unknown, it is important to further understand how BOPs affect the cochlea. In this study, the cochlea's response to blast exposure was modeled by a FE model of the ear with a two-chambered, spiraled cochlea to give insight into how the high pressures and large displacements within the cochlea could cause hearing loss. Furthermore, the cochleae of chinchillas were imaged using SEM to observe that possible blast-induced damage to the hair cells of the cochlea and to determine the possible protective effect of liraglutide in the cochlea.

Given that the ear is quite vulnerable to BOPs, better hearing protection is desired from our service men and women to prevent permanent hearing loss. This study also developed a 3D printed TB for standardized testing of HPDs for cost-effective, accurate, and efficient improvement of HPDs. The 3D printed test module was used to evaluate HPDs during blast exposure and showed the potential for being used for acoustic stimuli tests as well.

Chapter 2 of this dissertation reports the development of a FE model of the ear with a two-chambered, spiral cochlea to simulate the response of the ear when exposed to BOP. A BOP input with a peak pressure of 30.7 kPa resulted in large displacements of the stapes which subsequently caused high intracochlear pressures and significant BM displacements which would indicate permanent damage to the cochlea after BOP exposure. The spiral shape of the cochlea caused an asymmetric pressure distribution across the width of the cochlea or the SV and ST chambers and allowed for significant transverse motion of the BM. The spiral cochlea model reported in this chapter provides a

necessary advancement for progress towards a model able to predict the potential hearing loss sustained during BOP exposure.

In the next chapter, Chapter 3, a 3D printed TB was created for the purpose of providing standardized testing of HPDs to blast exposure and was used to test two different HPD designs under blast conditions. Results show that the pressure measurements in the 3D printed TB were well within the mean and standard deviation of published data from similar tests performed in human cadaveric TBs demonstrating that our 3D printed TB is a valid model for testing HPD designs. The 3D printed TB developed in this chapter provides an accurate and cost-effective evaluation tool for HPDs' protective function against BOP exposure with the potential to perform as a human temporal bone model for research in ear biomechanics for acoustic transmission and the development of middle ear implants.

Chapter 4 investigated the viability of OHCs of chinchillas that were exposed to six consecutive blast exposures ranging from 21-35 kPa (3-5 psi) and the effect of liraglutide on OHC survival after blast exposure. Results showed that OHC loss did not differ among animal groups; however, the ABR results showed hearing function loss in BOP exposed groups, and drug-treated chinchillas did regain more hearing function after blast. This study increases our understanding of the link between TBI and hearing loss while also supporting the use of liraglutide as a therapeutic for blast victims.

The work reported in this dissertation increases our understanding of cochlear mechanics and sustained damage from blast exposure, and as such, creates opportunities for future research that will progress towards the goals of understanding the damage mechanisms of blast in the inner ear, creating a model that can accurately predict the

damage to the ear from a given stimulus, and improving HPDs' effectiveness for protection against BOP exposure. Future research directions include:

- To develop a blast FE model of the ear that can accurately simulate the cochlear mechanics in response to blast utilizing an anatomically correct, three-chambered, spiral cochlea,
- To improve the acoustic response of the middle ear materials in the 3D printed TB allowing the model to be used as an accurate and cheap model for acoustic and blast testing situations,
- To increase the range of BOP levels tested, sample number, and frequency regions imaged with SEM to decrease variance in the results and better understand the extent that BOP affects the stereocilia of hair cells, and
- To perform histological and immunofluorescent studies on the cochlea's synaptic ribbons and hair cell vesicle activity and the CAS to clarify the damage mechanisms of blast and determine the therapeutic effect of liraglutide on the auditory system.

References

1. Batteau, D. W. The role of the pinna in human localization. *Proc. R. Soc. London. Ser. B. Biol. Sci.* 168:158–180, 1967.
2. Von Bekesy, G. Experiments in Hearing. Oxford, England: Mcgraw Hill, 1960, 745 pp.
3. Berger, E. H., R. W. Kieper, and D. Gauger. Hearing protection: Surpassing the limits to attenuation imposed by the bone-conduction pathways. *J. Acoust. Soc. Am.* 114:1955–1967, 2003.
4. de Boer, E., and A. L. Nuttall. The mechanical waveform of the basilar membrane. I. Frequency modulations ("glides") in impulse responses and cross-correlation functions. *J. Acoust. Soc. Am.* 101:3583–3592, 1997.
5. Borg, E., and J. Zakrisson. Stapedius reflex and speech features. *J. Acoust. Soc. Am.* 54:525–527, 1973.
6. Brown, M. A., X. D. Ji, and R. Z. Gan. 3D Finite Element Modeling of Blast Wave Transmission from the External Ear to Cochlea. *Ann. Biomed. Eng.* 49:757–768, 2021.
7. Bruce, I. C., Y. Erfani, and M. S. A. Zilany. A phenomenological model of the synapse between the inner hair cell and auditory nerve: Implications of limited neurotransmitter release sites. *Hear. Res.* 360:40–54, 2018.
8. Bruce, I. C., M. B. Sachs, and E. D. Young. An auditory-periphery model of the effects of acoustic trauma on auditory nerve responses. *J. Acoust. Soc. Am.* 113:369–388, 2003.
9. Brungart, D. S., N. J. Spencer, N. Pryor, N. Abouzahra, E. A. McKenna, and N. Iyer. Attenuation characteristics of an extended-wear hearing aid: Impulse and continuous noise. *J. Acoust. Soc. Am.* 148:1404–1414, 2020.
10. Cheng, T., R. Z. Gan, J. T. Cheng, and R. Z. Gan. Mechanical Properties of Stapedial Tendon in Human Middle Ear. *J. Biomech. Eng.* 129:913–18, 2007.
11. Cho, S.-I., S. S. Gao, A. Xia, R. Wang, F. T. Salles, P. D. Raphael, H. Abaya, J. Wachtel, J. Baek, D. Jacobs, M. N. Rasband, and J. S. Oghalai. Mechanisms of Hearing Loss after Blast Injury to the Ear. *PLoS One* 8:e67618, 2013.
12. Cooper, N. P., and J. J. Guinan. Efferent-mediated control of basilar membrane motion. *J. Physiol.* 576:49–54, 2006.
13. Dai, C., T. Cheng, M. W. Wood, and R. Z. Gan. Fixation and detachment of superior and anterior malleolar ligaments in human middle ear: Experiment and modeling. *Hear. Res.* 230:24–33, 2007.
14. Dau, T., O. Wegner, V. Mellert, and B. Kollmeier. Auditory brainstem responses with optimized chirp signals compensating basilar-membrane dispersion. *J. Acoust. Soc. Am.* 107:1530–1540, 2000.
15. Dewey, J. M. The air velocity in blast waves from t.n.t. explosions. *Proc. R. Soc. London. Ser. A. Math. Phys. Sci.* 279:366–385, 1964.
16. Díaz Santana, M. V., S. Eber, S. Barth, Y. Cypel, E. Dursa, and A. Schneiderman. Health-Related Quality of Life Among U.S. Veterans of Operation Enduring Freedom and Operation Iraqi Freedom—Results From a Population-Based Study. *Mil. Med.* 182:e1885–e1891, 2017.
17. Dolmazon, J., L. Bastet, and V. Shupljakov. A functional model of peripheral

auditory system in speech processing. , 1977.
18. Dougherty, A. L., A. J. MacGregor, P. P. Han, E. Viirre, K. J. Heltemes, and M. R. Galarneau. Blast-related ear injuries among U.S. military personnel. *J. Rehabil. Res. Dev.* 50:893–904, 2013.
19. Engles, W. G., X. Wang, and R. Z. Gan. Dynamic Properties of Human Tympanic Membrane After Exposure to Blast Waves. *Ann. Biomed. Eng.* 45:2383–2394, 2017.
20. Fedele, P. D., M. S. Binseel, J. T. Kalb, and G. R. Price. Using the Auditory Hazard Assessment Algorithm for Humans (AHAAH) With Hearing Protection Software, Release MIL-STD-1474E. 2013.at <http://www.arl.army.mil/arlreports/2013/ARL-TR-6748.pdf>
21. Fettiplace, R. Hair cell transduction, tuning, and synaptic transmission in the mammalian cochlea. *Compr. Physiol.* 7:, 2017.
22. Fung, Y. Biomechanics. New York, NY: Springer New York, 1993, 568 pp.doi:10.1007/978-1-4757-2257-4
23. Gallun, F. J., M. S. Lewis, R. L. Folmer, A. C. Diedesch, L. R. Kubli, D. J. McDermott, T. C. Walden, S. A. Fausti, H. L. Lew, and M. R. Leek. Implications of blast exposure for central auditory function: A review. *J. Rehabil. Res. Dev.* 49:1059, 2012.
24. Gan, R. Z., B. Feng, and Q. Sun. Three-dimensional finite element modeling of human ear for sound transmission. *Ann. Biomed. Eng.* 32:847–59, 2004.
25. Gan, R. Z., and S. Jiang. Surface Motion Changes of Tympanic Membrane Damaged by Blast Waves. *J. Biomech. Eng.* 141:, 2019.
26. Gan, R. Z., K. Leckness, K. Smith, and X. D. Ji. Characterization of Protection Mechanisms to Blast Overpressure for Personal Hearing Protection Devices – Biomechanical Measurement and Computational Modeling. *Mil. Med.* 184:251–260, 2019.
27. Gan, R. Z., D. Nakmali, X. D. Ji, K. Leckness, and Z. Yokell. Mechanical damage of tympanic membrane in relation to impulse pressure waveform – A study in chinchillas. *Hear. Res.* 340:25–34, 2016.
28. Gan, R. Z., B. P. Reeves, and X. Wang. Modeling of Sound Transmission from Ear Canal to Cochlea. *Ann. Biomed. Eng.* 35:2180–2195, 2007.
29. Gan, R. Z., Q. Sun, B. Feng, and M. W. Wood. Acoustic–structural coupled finite element analysis for sound transmission in human ear—Pressure distributions. *Med. Eng. Phys.* 28:395–404, 2006.
30. Gan, R. Z., and X. Wang. Multifield coupled finite element analysis for sound transmission in otitis media with effusion. *J. Acoust. Soc. Am.* 122:3527–3538, 2007.
31. Gan, R. Z., M. W. Wood, and K. J. Dormer. Human Middle Ear Transfer Function Measured by Double Laser Interferometry System. *Otol. Neurotol.* 25:423–435, 2004.
32. Gan, R., X. Zhang, and X. Guan. Modeling Analysis of Biomechanical Changes of Middle Ear Cochlea in Otitis Media. , 2011.doi:10.1063/1.3658144
33. Gao, W., D. Ding, X. Zheng, F. Ruan, and Y. Liu. A comparison of changes in the stereocilia between temporary and permanent hearing losses in acoustic trauma. *Hear. Res.* 62:27–41, 1992.

34. Greene, N. T., M. A. Alhussaini, J. R. Easter, T. F. Argo, T. Walilko, and D. J. Tollin. Intracochlear pressure measurements during acoustic shock wave exposure. *Hear. Res.* 365:149–164, 2018.
35. Greene, N. T., H. A. Jenkins, D. J. Tollin, and J. R. Easter. Stapes displacement and intracochlear pressure in response to very high level, low frequency sounds. *Hear. Res.* 348:16–30, 2017.
36. Guinan, J. J. Cochlear efferent innervation and function. *Curr. Opin. Otolaryngol. Head Neck Surg.* 18:447–453, 2010.
37. Hakon, J., K. Ruscher, B. Romner, and G. Tomasevic. Preservation of the Blood Brain Barrier and Cortical Neuronal Tissue by Liraglutide, a Long Acting Glucagon-Like-1 Analogue, after Experimental Traumatic Brain Injury. *PLoS One* 10:e0120074, 2015.
38. Heinz, M. G., X. Zhang, I. C. Bruce, and L. H. Carney. Auditory nerve model for predicting performance limits of normal and impaired listeners. *Cit. Acoust. Res. Lett. Online* 2:91, 2001.
39. Hickman, T. T., C. Smalt, J. Bobrow, T. Quatieri, and M. C. Liberman. Blast-induced cochlear synaptopathy in chinchillas. *Sci. Rep.* 8:10740, 2018.
40. Hirsch, J. D., R. L. Vincent, and D. J. Eisenman. Surgical reconstruction of the ossicular chain with custom 3D printed ossicular prosthesis. *3D Print. Med.* 3:7, 2017.
41. Ibrahim, R. A., and I. C. Bruce. Effects of Peripheral Tuning on the Auditory Nerve's Representation of Speech Envelope and Temporal Fine Structure Cues. In: The Neurophysiological Bases of Auditory Perception. New York, NY: Springer New York, 2010, pp. 429–438.doi:10.1007/978-1-4419-5686-6_40
42. Iha, L. C. N., and O. L. M. Cruz. Use of scanning electron microscopy in the cochlea of guinea pigs. *Braz. J. Otorhinolaryngol.* , 2019.doi:10.1016/j.bjorl.2018.11.008
43. Jia, S., S. Yang, W. Guo, and D. Z. Z. He. Fate of Mammalian Cochlear Hair Cells and Stereocilia after Loss of the Stereocilia. *J. Neurosci.* 29:15277–15285, 2009.
44. Jiang, S., C. Dai, and R. Z. Gan. Dual-laser measurement of human stapes footplate motion under blast exposure. *Hear. Res.* 403:108177, 2021.
45. Jiang, S., K. Smith, and R. Z. Gan. Dual-laser measurement and finite element modeling of human tympanic membrane motion under blast exposure. *Hear. Res.* 378:43–52, 2019.
46. Jiang, S., P. Welch, S. Sanders, and R. Z. Gan. Mitigation of Blast-Induced Hearing Damage using Liraglutide in Animal Model of Chinchilla. *J. Assoc. Res. Otolaryngol.* , 2021. *IN REVIEW*
47. Job, A., P. Hamery, S. De Mezzo, J.-C. Fialaire, A. Roux, M. Untereiner, F. Cardinale, H. Michel, C. Klein, and B. Belcourt. Rifle impulse noise affects middle-ear compliance in soldiers wearing protective earplugs. *Int. J. Audiol.* 55:30–37, 2016.
48. Kozin, E. D., N. L. Black, J. T. Cheng, M. J. Cotler, M. J. McKenna, D. J. Lee, J. A. Lewis, J. J. Rosowski, and A. K. Remenschneider. Design, fabrication, and in vitro testing of novel three-dimensionally printed tympanic membrane grafts. *Hear. Res.* 340:191–203, 2016.
49. Kujawa, S. G., and M. C. Liberman. Adding Insult to Injury: Cochlear Nerve

Degeneration after “Temporary” Noise-Induced Hearing Loss. *J. Neurosci.* 29:14077–14085, 2009.
50. Kujawa, S. G., and M. C. Liberman. Synaptopathy in the noise-exposed and aging cochlea: Primary neural degeneration in acquired sensorineural hearing loss. *Hear. Res.* 330:191–199, 2015.
51. Kuo, C.-Y., E. Wilson, A. Fuson, N. Gandhi, R. Monfaredi, A. Jenkins, M. Romero, M. Santoro, J. P. Fisher, K. Cleary, and B. Reilly. Repair of Tympanic Membrane Perforations with Customized Bioprinted Ear Grafts Using Chinchilla Models. *Tissue Eng. Part A* 24:527–535, 2018.
52. Kurioka, T., T. Matsunobu, K. Niwa, A. Tamura, S. Kawauchi, Y. Satoh, S. Sato, and A. Shiotani. Characteristics of laser-induced shock wave injury to the inner ear of rats. *J. Biomed. Opt.* 19:125001, 2014.
53. Kuru, I., H. Maier, M. Müller, T. Lenarz, and T. C. Lueth. A 3D-printed functioning anatomical human middle ear model. *Hear. Res.* 340:204–213, 2016.
54. Leckness, K., D. Nakmali, and R. Z. Gan. Computational Modeling of Blast Wave Transmission Through Human Ear. *Mil. Med.* 183:262–268, 2018.
55. Leonova, E. V., and Y. Raphael. Organization of cell junctions and cytoskeleton in the reticular lamina in normal and ototoxically damaged organ of Corti. *Hear. Res.* 113:14–28, 1997.
56. Li, Y., M. Bader, I. Tamargo, V. Rubovitch, D. Tweedie, C. G. Pick, and N. H. Greig. Liraglutide is neurotrophic and neuroprotective in neuronal cultures and mitigates mild traumatic brain injury in mice. *J. Neurochem.* 135:1203–1217, 2015.
57. Liberman, M. C., and S. G. Kujawa. Cochlear synaptopathy in acquired sensorineural hearing loss: Manifestations and mechanisms. *Hear. Res.* 349:138–147, 2017.
58. Lloyd Soderlund, L., E. A. McKenna, K. Tastad, and M. Paul. Prevalence of permanent threshold shifts in the United States Air Force hearing conservation program by career field, 2005–2011. *J. Occup. Environ. Hyg.* 13:383–392, 2016.
59. Manoussaki, D., R. S. Chadwick, D. R. Ketten, J. Arruda, E. K. Dimitriadis, and J. T. O’Malley. The influence of cochlear shape on low-frequency hearing. *Proc. Natl. Acad. Sci.* 105:6162–6166, 2008.
60. Mao, J. C., E. Pace, P. Pierozynski, Z. Kou, Y. Shen, P. VandeVord, E. M. Haacke, X. Zhang, and J. Zhang. Blast-Induced Tinnitus and Hearing Loss in Rats: Behavioral and Imaging Assays. *J. Neurotrauma* 29:430–444, 2012.
61. Masri, S., L. S. Zhang, H. Luo, E. Pace, J. Zhang, and S. Bao. Blast Exposure Disrupts the Tonotopic Frequency Map in the Primary Auditory Cortex. *Neuroscience* 379:428–434, 2018.
62. Mathews, Z. R., and A. Koyfman. Blast Injuries. *J. Emerg. Med.* 49:573–587, 2015.
63. Meddis, R., E. A. Lopez-Poveda, R. R. Fay, and A. N. Popper. Computational Models of the Auditory System. Boston, MA: Springer US, 2010, 545 pp.
64. Mediavilla Varas, J., M. Philippens, A. C. Meijer, A. C. van den Berg, P. C. Sibma, J. L. M. J. van Bree, and D. V. W. M. de Vries. Physics of IED blast shock tube simulations for mTBI research. *Front. Neurol.* 2:1–14, 2011.
65. Meyer-Bäse, U., A. Meyer-Bäse, and H. Scheich. An interspike interval method

for computing phase locking from neural firing. *Biol. Cybern.* 82:283–290, 2000.
66. Monfared, A., G. Mitteramskogler, S. Gruber, J. K. Salisbury, J. Stampfl, and N. H. Blevins. High-Fidelity, Inexpensive Surgical Middle Ear Simulator. *Otol. Neurotol.* 33:1573–1577, 2012.
67. Moore, D. F., A. Jérusalem, M. Nyein, L. Noels, M. S. Jaffee, and R. A. Radovitzky. Computational biology — Modeling of primary blast effects on the central nervous system. *Neuroimage* 47:T10–T20, 2009.
68. Murphy, W. J., G. A. Flamme, D. K. Meinke, J. Sondergaard, D. S. Finan, J. E. Lankford, A. Khan, J. Vernon, and M. Stewart. Measurement of impulse peak insertion loss for four hearing protection devices in field conditions. *Int. J. Audiol.* 51:S31–S42, 2012.
69. Nakashima, A., S. Sarray, and N. Fink. Insertion loss of hearing protection devices for military impulse noise. *Can. Acoust. - Acoust. Can.* 45:148–149, 2017.
70. Niwa, K., K. Mizutari, T. Matsui, T. Kurioka, T. Matsunobu, S. Kawauchi, Y. Satoh, S. Sato, A. Shiotani, and Y. Kobayashi. Pathophysiology of the inner ear after blast injury caused by laser-induced shock wave. *Sci. Rep.* 6:31754, 2016.
71. Nuttall, A. L., D. F. Dolan, and G. Avinash. Laser Doppler velocimetry of basilar membrane vibration. *Hear. Res.* 51:203–213, 1991.
72. Oleksiak, M., B. M. Smith, J. R. St. Andre, C. M. Caughlan, and M. Steiner. Audiological issues and hearing loss among veterans with mild traumatic brain injury. *J. Rehabil. Res. Dev.* 49:995, 2012.
73. De Paolis, A., M. Bikson, J. T. Nelson, J. A. de Ru, M. Packer, and L. Cardoso. Analytical and numerical modeling of the hearing system: Advances towards the assessment of hearing damage. *Hear. Res.* 349:111–128, 2017.
74. De Paolis, A., H. Watanabe, J. T. Nelson, M. Bikson, M. Packer, and L. Cardoso. Human cochlear hydrodynamics: A high-resolution μCT-based finite element study. *J. Biomech.* 50:209–216, 2017.
75. Pickles, J. O., M. P. Osborne, and S. D. Comis. Vulnerability of tip links between stereocilia to acoustic trauma in the guinea pig. *Hear. Res.* 25:173–183, 1987.
76. Price, G. R. Validation of the auditory hazard assessment algorithm for the human with impulse noise data. *J. Acoust. Soc. Am.* 122:2786, 2007.
77. Price, G. R. Predicting mechanical damage to the organ of Corti. *Hear. Res.* 226:5–13, 2007.
78. Price, G. R., and J. T. Kalb. Insights into hazard from intense impulses from a mathematical model of the ear. *J. Acoust. Soc. Am.* 90:219–227, 1991.
79. Puel, J. Chemical synaptic transmission in the cochlea. *Prog. Neurobiol.* 47:449–476, 1995.
80. Rabinowitz, P. M. Noise-induced hearing loss. *Am. Fam. Physician* 61:2749–56, 2759–60, 2000.
81. Race, N., J. Lai, R. Shi, and E. L. Bartlett. Differences in postinjury auditory system pathophysiology after mild blast and nonblast acute acoustic trauma. *J. Neurophysiol.* 118:782–799, 2017.
82. Race, N., J. Lai, R. Shi, and E. L. Bartlett. Differences in postinjury auditory system pathophysiology after mild blast and nonblast acute acoustic trauma. *J. Neurophysiol.* 118:782–799, 2017.
83. Reichenbach, T., and A. J. Hudspeth. The physics of hearing: fluid mechanics and

the active process of the inner ear. *Reports Prog. Phys.* 77:076601, 2014.
84. Remenschneider, A. K., S. Lookabaugh, A. Aliphas, J. R. Brodsky, A. K. Devaiah, W. Dagher, K. M. Grundfast, S. E. Heman-Ackah, S. Rubin, J. Sillman, A. C. Tsai, M. Vecchiotti, S. G. Kujawa, D. J. Lee, and A. M. Quesnel. Otologic Outcomes After Blast Injury. *Otol. Neurotol.* 35:1825–1834, 2014.
85. Ren, L.-J., C. Hua, G.-H. Ding, L. Yang, P.-D. Dai, and T.-Y. Zhang. Three-dimensional finite element hydrodynamical modeling of straight and spiral cochlea. , 2018.
86. Ren, L.-J., Y. Yu, Y.-Q. Fang, C. Hua, P.-D. Dai, and T.-Y. Zhang. Finite element simulation of cochlear traveling wave under air and bone conduction hearing. *Biomech. Model. Mechanobiol.* , 2021.doi:10.1007/s10237-021-01443-7
87. Rhode, W. S. Distortion product otoacoustic emissions and basilar membrane vibration in the 6–9 kHz region of sensitive chinchilla cochleae. *J. Acoust. Soc. Am.* 122:2725, 2007.
88. Robles, L., and M. a Ruggero. Mechanics of the Mammalian Cochlea. *Physiol. Rev.* 81:1305–1352, 2001.
89. Rønne, F. M., T. Dau, J. Harte, and C. Elberling. Modeling auditory evoked brainstem responses to transient stimuli. *J. Acoust. Soc. Am.* 131:3903–3913, 2012.
90. Rose, A. S., C. E. Webster, O. L. A. Harrysson, E. J. Formeister, R. B. Rawal, and C. E. Iseli. Pre-operative simulation of pediatric mastoid surgery with 3D-printed temporal bone models. *Int. J. Pediatr. Otorhinolaryngol.* 79:740–744, 2015.
91. Rosowski, J. J., I. Dobrev, M. Khaleghi, W. Lu, J. T. Cheng, E. Harrington, and C. Furlong. Measurements of three-dimensional shape and sound-induced motion of the chinchilla tympanic membrane. *Hear. Res.* 301:44–52, 2013.
92. Salvi, R. J., J. Wang, and D. Ding. Auditory plasticity and hyperactivity following cochlear damage. *Hear. Res.* 147:261–274, 2000.
93. Schrode, K. M., M. A. Muniak, Y.-H. Kim, and A. M. Lauer. Central Compensation in Auditory Brainstem after Damaging Noise Exposure. *eneuro* 5:ENEURO.0250-18.2018, 2018.
94. Shimada, T., and D. J. Lim. The Fiber Arrangement of the Human Tympanic Membrane. *Ann. Otol. Rhinol. Laryngol.* 80:210–217, 1971.
95. Smith, K. D., T. Chen, and R. Z. Gan. Hearing Damage Induced by Blast Overpressure at Mild TBI Level in a Chinchilla Model. *Mil. Med.* 185:248–255, 2020.
96. Soeta, Y., and Y. Ando. Signal Processing Model of Human Auditory System. In: Neurally Based Measurement and Evaluation of Environmental Noise. 2015, pp. 5–50.doi:10.1007/978-4-431-55432-5_2
97. Sohmer, H. Reflections on the role of a traveling wave along the basilar membrane in view of clinical and experimental findings. *Eur. Arch. Oto-Rhino-Laryngology* 272:531–535, 2015.
98. Stenfeldt, K., C. Johansson, and S. Hellström. The Collagen Structure of the Tympanic Membrane. *Arch. Otolaryngol. Neck Surg.* 132:293, 2006.
99. Stratasys Ltd. Digital Materials Data Sheet. , 2013.at <https://www.stratasys.com/-/media/files/material-spec-sheets/mss_pj_digitalmaterialsdatasheet_0617a.pdf>
100. Stratasys Ltd. Vero Material Data Sheet. , 2018.at <https://www.stratasys.com/-/media/files/material-spec-sheets/vero-material-data-sheet.pdf>

101. Talcott, K. A., J. G. Casali, J. P. Keady, and M. C. Killion. Azimuthal auditory localization of gunshots in a realistic field environment: Effects of open-ear versus hearing protection-enhancement devices (HPEDs), military vehicle noise, and hearing impairment. *Int. J. Audiol.* 51:S20–S30, 2012.
102. Tepe, V., C. Smalt, J. Nelson, T. Quatieri, and K. Pitts. Hidden Hearing Injury: The Emerging Science and Military Relevance of Cochlear Synaptopathy. *Mil. Med.* 182:e1785–e1795, 2017.
103. Tweedie, D., L. Rachmany, V. Rubovitch, Y. Li, H. W. Holloway, E. Lehrmann, Y. Zhang, K. G. Becker, E. Perez, B. J. Hoffer, C. G. Pick, and N. H. Greig. Blast traumatic brain injury-induced cognitive deficits are attenuated by preinjury or postinjury treatment with the glucagon-like peptide-1 receptor agonist, exendin-4. *Alzheimer's Dement.* 12:34–48, 2016.
104. Vadalà, R., E. Giugni, F. R. Pezzella, U. Sabatini, and S. Bastianello. Progressive sensorineural hearing loss, ataxia and anosmia as manifestation of superficial siderosis in post traumatic brain injury. *Neurol. Sci.* 34:1259–1262, 2013.
105. Walilko, T. J., R. D. Lowe, T. F. Argo, G. D. Meegan, N. T. Greene, and D. J. Tollin. Experimental Evaluation of Blast Loadings on the Ear and Head with and Without Hearing Protection Devices. In: Conference Proceedings of the Society for Experimental Mechanics Series. 2017, pp. 101–109.
106. Wang, H., S. Yin, Z. Yu, Y. Huang, and J. Wang. Dynamic changes in hair cell stereocilia and cochlear transduction after noise exposure. *Biochem. Biophys. Res. Commun.* 409:616–621, 2011.
107. Wang, X., and R. Z. Gan. 3D finite element model of the chinchilla ear for characterizing middle ear functions. *Biomech. Model. Mechanobiol.* 15:1263–1277, 2016.
108. Whittemore, K. R., S. N. Merchant, B. B. Poon, and J. J. Rosowski. A normative study of tympanic membrane motion in humans using a laser Doppler vibrometer (LDV). *Hear. Res.* 187:85–104, 2004.
109. Wiener, F. M., and D. A. Ross. The Pressure Distribution in the Auditory Canal in a Progressive Sound Field. *J. Acoust. Soc. Am.* 18:401–408, 1946.
110. Xydakis, M. S., V. S. Bebarta, C. D. Harrison, J. C. Conner, G. a Grant, and A. S. Robbins. Tympanic-membrane perforation as a marker of concussive brain injury in Iraq. *N. Engl. J. Med.* 357:830–1, 2007.
111. Zhang, X., and R. Z. Gan. Dynamic properties of human tympanic membrane based on frequency-temperature superposition. *Ann. Biomed. Eng.* 41:205–14, 2013.
112. Zhang, X., and R. Z. Gan. Finite element modeling of energy absorbance in normal and disordered human ears. *Hear. Res.* 301:146–155, 2013.
113. Zhang, Y., C. K. Kim, K.-J.-B. Lee, and Y. Park. Resultant Pressure Distribution Pattern along the Basilar Membrane in the Spiral Shaped Cochlea. *J. Biol. Phys.* 33:195–211, 2007.
114. Zhong, N., and X. Zhao. 3D printing for clinical application in otorhinolaryngology. *Eur. Arch. Oto-Rhino-Laryngology* 274:4079–4089, 2017.
115. Zilany, M. S. A., and I. C. Bruce. Modeling auditory-nerve responses for high sound pressure levels in the normal and impaired auditory periphery. *J. Acoust. Soc. Am.* 120:1446–1466, 2006.

116. Zilany, M. S. A., and I. C. Bruce. Representation of the vowel /ε/ in normal and impaired auditory nerve fibers: Model predictions of responses in cats. *J. Acoust. Soc. Am.* 122:402–417, 2007.